Development of Constitutive Relation for Multiscale Modeling of Carbon Fiber Reinforced Polymer Composites under Uncertainty

By

Rudraprasad Bhattacharyya

Dissertation

Submitted to the Faculty of the

Graduate School of Vanderbilt University

in partial fulfillment of the requirements

for the degree of

DOCTOR OF PHILOSOPHY

in

Civil Engineering

January 31, 2021

Nashville, Tennessee

Approved:
Douglas E. Adams, PhD.
Prodyot K. Basu, DSc.
Sankaran Mahadevan, PhD.
Ravindra Duddu, PhD.
G. Kane Jennings, PhD.

This dissertation is dedicated to the service of the mankind.

ॐ सर्वे भवन्तु सुखिनः सर्वे सन्तु निरामयाः ।
सर्वे भद्राणि पश्यन्तु मा कश्चिद्दुःखभाग्भवेत् ।

"May all be happy and free from illness.
May all see what is auspicious and may all be free from suffering"

ACKNOWLEDGMENT

I would like to express my sincere gratitude to my PhD advisor Professor Douglas Adams for his continuous support towards my PhD research. His guidance has helped me in all my research endeavor and professional growth. I would like to thank Professor Prodyot K Basu for being a mentor, a confidant, and huge source of knowledge. I want to thank Professor George Hornberger, the chair of the 'Student progress committee'for evaluating my performance towards doctoral program. My thanks to Professor Sankaran Mahadevan for serving as my dissertation committee member and mentoring on the uncertainty quantification aspects in my research. Professor G Ken Jennings, thank you for being supportive towards my endeavor to complete the doctoral degree. I want to acknowledge Professor Ravindra Duddu for meticulously checking all mathematical derivations and providing valuable feedback.

My sincere thanks to Professor Caglar Oskay for his intellectual support and allowing me to access the computing resources at 'Multiscale Computation Mechanics Laboratory'. I acknowledge partial financial support provided by the Aerospace Systems Directorate of the Air Force Research Laboratory (Contract No: GS04T09DBC0017 through Engility Corporation and FA8650-12-D-3212/0016 through UDRI) and Dr. Stephen B. Clay for providing thoughtful comments during weekly meetings. I want to thank my wonderful colleagues at MCML and LASIR for their support. My special thanks to Dr. Thushara Gunda, Dr. Xiang Zhang, Dr. Paul A. Sparks, Dr. Paromita Nath and Dr. Saideep Nannapaneni for their help. I also want convey my thanks to the wonderful CEE department staffs.

My thanks to Professor Curtis Byers and Professor Sanjiv Gokhale for immense professional support towards developing my knowledge in structural engineering practice and to obtain the PE Civil Structural license. I gratefully acknowledge the excellent resources available at Vanderbilt University campus (*e.g.* VU library, VUMC, graduate school travel grant). Finally, I want to acknowledge the funding I received from the Peter G Hoadley fellowship and Russell G Hamilton Graduate Leadership Development Institute travel grant.

To this end, I would like to acknowledge my maternal uncle, who stimulated and supported my desire to become a civil engineer. And last but not least, I would like to thank my family - my parents for their immense support, my sister Madhumanti for providing sheer inspiration in pursuing PhD and my wife Soumita for her love.

TABLE OF CONTENTS

LIST OF TABLES

LIST OF FIGURES

CHAPTER 1

INTRODUCTION

1.1 Research Motivation

All quasi-brittle materials experience degradation in mechanical properties due to damage accumulation at the microscopic level caused by debonding of atoms as well as nucleation, or growth and bridging of microcracks and/or microvoids, prior to the development of macroscale cracks. A continuum damage representation utilizes homogeneous models in which microcracks and microvoids are represented by continuous variables that correspond to the mechanical behavior of continua. Furthermore, accumulation of damage resulting from manufacturing defects is common in materials that are utilized in structural applications. Engineers are required to model the damage process in quasi-brittle materials in order to reduce the risk of sudden failures in which the material does not show sufficient signs that failure is imminent. Unlike elastic-plastic and pure brittle failures, quasi- brittle failure processes involve characteristics that resemble both of these types of failure. This requires that methods of both plasticity and damage mechanics be combined to model quasi-brittle failures. Over the last two decades, a number of discrete numerical tools based on X-FEM, mesh-free, and cohesive-zone methods have been developed to address the need for quasi-brittle models of failure. For applications like damage modeling of laminated fiber composites in aircraft, there is no single technique that engineers can utilize to provide confidence in failure prediction due to mathematical intricacies and deficiencies in the current techniques to enable mechanics based calibration of model parameters using experimental data. Lately, researchers are making significant strides to implement advanced simulation techniques in commercial software.

The design and certification of aerospace composite structures require extensive use of experimental data over a range of specimens and loading scenarios, from coupons to full-scale components. In addition to being expensive and time-consuming, this approach may lead to over-conservative designs. Specifically, the lack of a full understanding of damage initiation and growth at the microscopic level culminating into failure at the macroscopic or structural level in composites prevents the use of the damage tolerant approaches commonly used in the design of metallic aerospace structures. As a result, conventional composite airframe designs cannot fully capitalize on the weight and performance gains that are possible with composites. As the potential benefits are being recognized of incorporating predictive failure modeling and simulation in aircraft design, certification, and maintenance processes, there is significant effort aimed at improving predictive computational methods, as exemplified by the works of the U.S. DoD [22] and NASA [57, 52]. A validated predictive modeling capability is critical to rapid and economical aircraft design and certification processes using new composite materials.

1.2 Literature Review

In the case of composites, loss of strength may be the result of mesoscale phenomena like matrix fracture, fiber-matrix debonding, matrix crushing, fiber breakage, inter-fiber interaction, and so on. Of these mesoscale manifestations of material damage, the first two sources of damage (matrix fracture and fiber-matrix debonding) are of primary concern to engineers. Damage processes are often associated with the release of mechanical energy. In cross-plied laminates, the failure paths in an angle ply are often aligned along the orientation of the fiber. For accurate prediction of the failure process in such composites, the development of three-dimensional failure criteria for fiber composites is an important step towards developing a mechanics-based progressive damage model. But these failure criteria are more phenomenological than mechanics-based in nature and, hence, have limited usefulness in mechanical performance prediction in the context of a multiscale modeling framework. From 1980 through 1990, continuum damage mechanics has advanced considerably in modeling progressive degradation, as presented in Krajcinovic [43]; Chaboche [13, 14]; Simo and Ju [76]. Continuum damage mechanics offers a framework for modeling initiation, growth and coalescence of microcracks and microvoids that is consistent with the scale of the damage phenomena involved. These advances have provided a framework from which to develop a model of distributed damage in quasi-brittle materials. This framework offers computational efficiency without loss of accuracy. The work presented here assumed deformations are small and elastic in nature. Temperature change and fatigue loading effects are not considered in this study.

1.2.1 Damage Modeling Techniques

Within the continuum framework, material cracking is often modeled with either the discrete crack concept using the principles of fracture mechanics or the smeared crack concept using continuum mechanics. Hillerborg *et al.* [37] applied a cohesive zone approach, which was introduced by Dugdale [23] and Barenblatt [4], to quasi-brittle materials. In the Cohesive Zone Model (CZM), fracture formation is regarded as a phenomenon in the growth of a crack across an extended crack tip and is resisted by cohesive tractions. CZM is usually classified as extrinsic or intrinsic. Extrinsic CZM assumes interface separation only after exceeding the cohesive strength as described in Camacho *et al.* [11] and Zhang *et al.* [90]. In the extrinsic CZM case, the model is implemented by adaptive insertion of interface elements with zero-thickness as damage progresses. On the other hand, intrinsic methods rely on the assumption of gradual increase of cohesive traction, as proposed by Xu and Needleman [89]. These authors described a concept of adaptive insertion between the continuum elements following a potential-based traction–separation law . This approach is implemented by a priori insertion of interface elements within the finite element mesh, along all potential crack paths as described by Park *et al.* [63]. A major disadvantage of the CZM approach is its computational cost. A different modeling approach, which is straightforward to implement and computationally more efficient, is based on a smeared crack concept. In this approach, the fracture process is modeled by a banded region of fixed width. It assumes accumulation of microvoids, and (or) microcracks within a band, which later evolves as a macro crack. This approach is referred to as the local approach in the continuum model. Unlike for CZM, no special elements, e.g. interface elements, need to be incorporated in the local approach. The failure path for a continuum damage model evolves based on the thermomechanical properties of the constituent material(s). A thorough treatment of continuum damage modeling with different damage potential functions is provided by Geers [30]. Notwithstanding various differences in formulations, strength prediction by continuum damage mechanics- and fracture mechanics-based models is a function of the model used. In practice, analysts find it more convenient to use methods based on a continuum damage model, which is a rapidly emerging predictive tool suited to design environments (see, for example, Lemaitre [47], Lemaitre and Dufailly [49], Krajcinovic [44], Lemaitre and Desmorat [48], and Voyiadjis and Kattan [88]).

1.2.2 Numerical Regularization Techniques

The accumulation of damage within a material leads to strain softening. Local continuum damage models are strain softening models that obey the principle of local action i.e. the constitutive behavior at a local point does not depend upon any action/variables at a distance (neighboring points). The problem with the local behavior of a softening model is that as soon as a material point starts to soften, it takes up all the deformation. Since all deformation occurs at the material point, damage only grows in that point, resulting in further softening. If damage models are included in the constitutive behavior in a finite element analysis, then after localization all the deformation accumulates in one element (or one row of elements). This makes the analysis mesh size dependent. If the mesh size is selected to be infinitely small then the energy dissipated in the localized band will approach to zero. In reality, damage consists of voids and/or cracks. Therefore, physically, damage cannot continue to grow at a local material point. In a real material, damage spreads over a finite length.

It is known that the results from continuum damage mechanics-based constitutive models demonstrate pathological mesh size dependence. This is purely a numerical issue arising out of loss of ellipticity in local equilibrium equations, as identified by de Borst *et al.* [21]. Several regularization techniques have been proposed to alleviate this sensitivity to mesh size. Bažant and Oh [6] proposed the fracture energy based crack band model that links the energy dissipation process with finite element size in a local framework. The paper reasoned that for a quasi-brittle material, microcracks span a region with a characteristic length scale quantifying the extent of the process zone. It is, therefore, physically appropriate to model localization as a crack band. The formulation related the fracture energy (typically experimentally characterized) to the energy dissipated within the crack band. In the context of numerical analysis, the crack band width is taken as the element size parameter, which is used to adjust the failure parameters. The major advantage of this formulation is that the formulation remains local and the algorithmic structure of FE code requires minor adjustment. This method was previously employed by several researchers (e.g. [65, 39, 59]) for single-scale models. These studies focused on comparing methodologies to estimate the element size parameter based on the geometry of the discretization.

Subsequently, several nonlocal damage models were developed in the 1980s and 1990s. These non-local models can be categorized into two groups: (1) nonlocal or integral damage models of Bažant [5], Pijaudier-Cabot and Bažant [66], Jirásek [38] and (2) the gradient enrichment approach by de Borst and Muhlhaus [20], Peerlings *et al.* [64], Jirásek and Rolshoven [40, 41]. The nonlocal damage models incorporate the nonlocal effect of damage using either an equivalent strain or a damage measure averaged over the domain of interest. The difference between the nonlocal integral and enrichment gradient approach depends solely on their methods of implementation. But both these methods are computationally expensive. On the other hand, the crack band model is more straightforward to implement in the finite element framework because it does not need weighted averaging of the damage at each increment. Many researchers have employed the crack band method primarily for numerical regularization. This approach guarantees mesh size objective results because the dissipation of fracture energy is regularized by a characteristic length parameter ensuring mesh size objective results. The engineering research community has embraced the crack band model for simulating quasi-brittle materials like concrete (Jirásek and Bauer [39]; Slobbe *et al.* [78]; Cervenka *et al.* [87]) and fiber composite laminates (Pinho *et al.* [70]; Reinoso *et al.* [71]; Pineda *et al.* [67]; Heinrich and Waas [35]; Maimi *et al.* [54, 55]). For this reason, most of the commercial nonlinear finite element software packages are incorporating this model. They have addressed the issue of estimating critical mesh size for different modes of failure of the composite.

1.2.3 Progressive Damage Analysis of Fiber Composites

Progressive Damage Analysis (PDA) is a terminology that applies to all modeling techniques that allow for the prediction of the initiation and evolution of damage. Several material constitutive models are proposed in the existing literature. Pinho *et al.* [69, 70] presented a physically-based failure criteria to model fiber kinking in laminated composites. In addition, their study has the ability to capture 3D effects and a generic non-linear shear behavior. The physical model for matrix compression failure is based on the Mohr-Coulomb failure criterion and also predicts the fracture angle. Ridha *et al.* [72] and Su *et al.* [81] modeled carbon fiber reinforced epoxy composite open-hole laminates under using failure criteria under tensile and compressive loading. Leone *et al.* [50] used used a continuum damage assumption to model intra-ply damage. For interply delamination and adhesive damage, they implemented cohesive elements. In addition to continuum damage models, computational modeling involving the use of cohesive zone modeling is also presented in the literature, such as in Higuchi *et al.* [36], van Dongen *et al.* [84]. PDA in the context of multiscale modeling is presented in Laurin *et al.* [46], Pineda *et al.* [68], and Massarwa *et al.* [56]. In PDA the researchers predominantly use a continuum damage model, which is straightforward to implement computationally. In addition, application of a mechanics-based model is more physically meaningful compared to a failure criteria. In the proposed Eigenstrain-based Reduced-Order Homogenization Method (ERHM) based modeling approach presented herein, a hierarchical multiscale method due to Fish [27] is used. In this method, the nucleation and propagation of damage within the composite are tracked at the level of constituent materials using a continuum damage model without applying any phenomenological failure criterion at the macroscale.

In ERHM the microstructural information like localization operators, concentration tensors, and influence functions are precomputed before undertaking the progressive damage analysis at the macroscale. The microstructural analyses are performed over a Representative Unit Cell (RUC), which is coupled with the structural analysis at the macroscale. The computational cost of homogenization is reduced by developing a reduced-order microstructural geometry. The microstructural analyses are concurrently performed during PDA. ERHM can account for progressive debonding between the fiber and the matrix at the scale of the microstructure, and ERHM is equipped with an adaptive model improvement capability to hierarchically increase model fidelity as discussed by Oskay and Fish [60] and Crouch and Oskay [17]. A symmetric version of ERHM (S-ERHM) was employed in the prediction of failure under static loading for open hole specimens by Crouch *et al.* [18] and Bogdanor and Oskay [9]. In all these studies, an arctangent type damage potential was used.

Composite materials under shear loading exhibit a nonlinear stress-strain response prior to failure. Evidence of shear nonlinearity in laminated composites containing high strength fibers embedded in an epoxy resin was discussed in Soutis *et al.* [79], Gilat *et al.* [32], Littell *et al.* [51], Park *et al.* [62], and Salavatian *et al.* [74]. This nonlinear plane shear response of composite materials is well known, and there are several approaches to consider this effect in material modeling, e.g., such as the approaches by Paepegem *et al.* [85] and Lomakin *et al.* [53]. Computational considerations are discussed in Paepegem *et al.* [86] and Fedulov *et al.* [25]. In contrast, brittle failure is observed in composites under pure uniaxial loading. In damage mechanics-based models, the ductility of a material is controlled by model parameters that are meant to capture the damage evolution process. A novel weighting approach for the damage evolution model is proposed in this to account for the differences in damage evolution of composites under purely normal and purely shear loads. Earlier, in Bogdanor and Oskay [9], the range of strain triaxiality varied from pure hydrostatic to pure shear loading. No experimental evidence is available to validate the general shape of the failure surface employed; however, a discussion is provided that gives a rational explanation for the observed nature of the failure surface. The lack of experimental data is due to the fact that the constitutive model represents the behavior of the in-situ resin.

1.3 Research Goal and Objectives

Research goal: Develop a mesh size independent multiscale computational framework to model progressive damage in carbon fiber reinforced polymer composites. The matrix constituent is 977-3 epoxy resin, which demonstrates brittle failure under uniaxial loading and ductile failure under shear dominated loading. In particular, the focus of this dissertation is on unidirectional carbon-fiber reinforced polymer composites under quasi-static loading.

Based on the research goal for the dissertation, the following objectives were identified to accomplish the goal.

1. Develop a constitutive model to predict microscale damage propagation leading to laminate failure in CFRP composites under mixed-mode loading.
2. Develop a mesh size independent multiscale computational framework for modeling damage and failure of CFRP structural components.
3. Incorporate uncertainty in progressive damage modeling arising from epistemic uncertainty.

1.4 Organization of the Dissertation

The ERHM multiscale model used in this dissertation is presented in Chapter 2. The treatment of alleviating spurious residual stiffness is described. The computational implementation of the microscale analysis using parallel computing is presented. The development of the continuum damage mechanics based constitutive relation for carbon fiber and polymer matrix material is described in Chapter 3. A new parameter weighting approach to capture the disparate damage evolution characteristics under pure uniaxial and pure shear loading is presented. The novel contribution towards constitutive model development is its ability to predict strength under multi-axial loading. Calibration of constitutive model parameters under epistemic uncertainty is described in Chapter 4. For this purpose properties of laminated composite IM7/977-3 is used. The second objective of this dissertation, alleviation of spurious mesh size dependence, is presented in Chapter 5. Formulation of a novel multiscale crack band model and its implementation in commercial software, Abaqus, is presented. The new constitutive model is applied to multiscale modeling framework for the purpose of validation. The results in Chapter 6 represent the three different composite laminates with unnotched and open-hole specimens. The validation study is conducted under tension and compression load. Finally, conclusions from this research and suggestions for future research are provided in Chapter 7.

CHAPTER 2

MULTISCALE MODELING FRAMEWORK

In this chapter, the multiscale modeling framework used in the proposed research is discussed. An eigenstrain based reduced-order model is implemented. A new constitutive function is defined to model the effects of damage accumulation and expressions for model calibration based on experimental data are derived in the mechanics-based approach.

During numerical modeling of heterogeneous materials the microstructure is often presented using unit cell with periodic microstructure [58, 82]. In reality, most of the materials do not possess material periodicity. It has been proven [82, 91] that even for non-periodic materials, the microstructural analysis based on periodic boundary conditions lead to satisfactory effective responses. In multiscale analysis, a domain comprising of three-dimensional fiber composite having fine ($\mathcal{F}$) and coarse ($\mathcal{C}$) effects can be denoted by $\mathbf{\Omega} = \mathbf{\Omega}^{(\mathcal{F})} \cup \mathbf{\Omega}^{(\mathcal{C})}$. This leads to the problem of defining a representative unit cell with locally periodic boundary conditions over which the averaging is performed [31, 83, 45]. This is followed by the construction of numerical models of its heterogeneity under the assumption of local periodicity. Consider a three-dimensional macroscopic fiber composite domain, $\mathbf{\Omega} \subset \mathbb{R}^3$, made up of heterogeneous but locally periodic repeating representative unit cell, $\mathbf{\Theta} \subset \mathbb{R}^3$. The multiscale structure of the material is schematically illustrated in Figure 2.1.

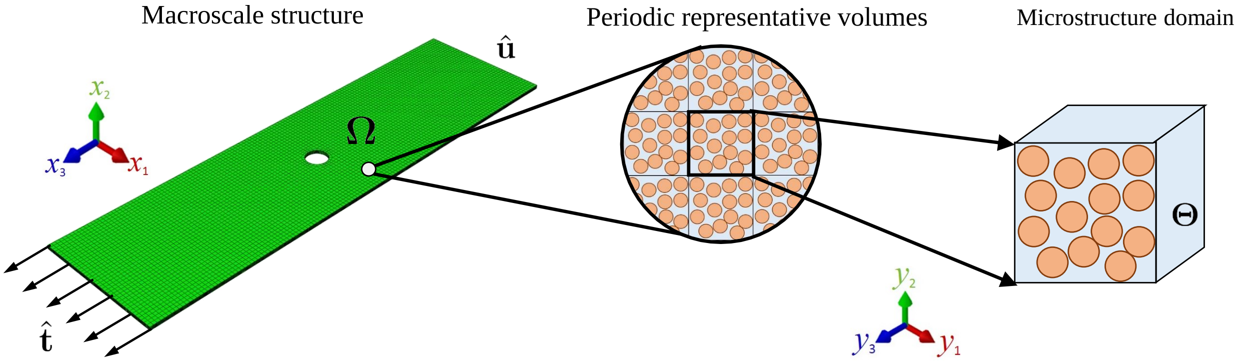

Figure 2.1: Schematic representation of Macro- and Micro-scale problem in CFRP

Due to heterogeneity in fiber composites, the displacement fields fluctuate at the scale of the microstructure, $\boldsymbol{\Theta}$. A scaled coordinate system, $\mathbf{y} = \mathbf{x}/\zeta$, is introduced to capture the scale of material heterogeneity. The scaling parameter, ζ, satisfies the condition $0 < \zeta \ll 1$. The representative volume, $\boldsymbol{\Theta}$, in terms of the $\mathbf{y}$ coordinate. Any response field $\boldsymbol{\Xi}$ and its macroscopic spatial gradient can then be expressed as

$$\Xi^{\zeta}(\mathbf{x}) = \Xi(\mathbf{x}, \mathbf{y}(\mathbf{x})); \quad \nabla_{\mathbf{x}} \Xi^{\zeta}(\mathbf{x}) = \nabla_{\mathbf{x}} \Xi(\mathbf{x}) + \frac{1}{\zeta} \nabla_{\mathbf{y}} \Xi(\mathbf{x}, \mathbf{y}) \tag{2.1}$$

The macroscale stress ($\overline{\boldsymbol{\sigma}}$) and strain ($\overline{\boldsymbol{\epsilon}}$) are obtained by spatial averaging of the stresses and strains, as shown below.

$$\overline{\boldsymbol{\sigma}}(\mathbf{x}, t) = \frac{1}{|\Theta|} \int_{\Theta} \boldsymbol{\sigma}(\mathbf{x}, \mathbf{y}, t) \; d\mathbf{y} \tag{2.2}$$

$$\overline{\boldsymbol{\epsilon}}(\mathbf{x}, t) = \frac{1}{|\Theta|} \int_{\Theta} \boldsymbol{\epsilon}(\mathbf{x}, \mathbf{y}, t) \; d\mathbf{y} \tag{2.3}$$

in which $|\Theta|$ is the volume of the representative volume element. The equilibrium equations at two different scales, namely, $\mathcal{O}(\zeta^{-1})$ and $\mathcal{O}(1)$ are represented as:

$$\mathcal{O}(\zeta^{-1}): \qquad \nabla_y \cdot \left[\mathbf{C}(\mathbf{x}, \mathbf{y}) : \left(\overline{\boldsymbol{\epsilon}}(\mathbf{x}, t) + \nabla_y \mathbf{u}^1(\mathbf{x}, \mathbf{y}, t) - \boldsymbol{\mu}(\mathbf{x}, \mathbf{y}, t) \right) \right] = 0 \tag{2.4}$$

$$\mathcal{O}(1): \qquad \nabla_x \cdot \boldsymbol{\sigma}(\mathbf{x}, \mathbf{y}, t) = 0 \tag{2.5}$$

in which the tensor of elastic moduli, $\mathbf{C}$, is considered to vary as a function of the microscopic coordinate ($\mathbf{y}$) only, $\boldsymbol{\mu}$ are the inelastic strains in the microstructure due to damage and $\mathbf{u}^1$ is the locally fluctuating displacement. Equation (2.4) constitutes the microscale equilibrium equation applied over the domain of the representative volume, $\boldsymbol{\Theta}$. Equation (2.5) is averaged over $\boldsymbol{\Theta}$ to obtain the macroscopic equilibrium equation defined over the problem domain, $\boldsymbol{\Omega}$.

2.1 Eigenstrain-based Reduced Order Modeling

Implementation of mathematical homogenization using Equations (2.4) and (2.5) leads to the standard computational homogenization (also known as FE^2) method as proposed by Feyel and Chaboche [26]. As the direct implementation of the FE^2 approach is computationally expensive, eigenstrain based Reduced Order Model (ROM) is developed herein following Oskay and Fish [60] and Crouch and Oskay [17]. For completeness, a concise overview of the reduced-order modeling approach for computational homogenization is presented here. In a heterogeneous microstructure, the microscale displacement field ($\mathbf{u}^1$) is defined by the macroscopic applied strains, ($\overline{\boldsymbol{\epsilon}}$), and the inelastic strains at the microscale, ($\boldsymbol{\mu}$), as given below.

$$\mathbf{u}^1(\mathbf{x},\mathbf{y},t) = \mathbf{H}(\mathbf{y}) : \bar{\boldsymbol{\epsilon}}(\mathbf{x},t) + \int_\Theta \mathbf{h}(\mathbf{y},\hat{\mathbf{y}}) : \boldsymbol{\mu}(\mathbf{x},\hat{\mathbf{y}},t)d\hat{\mathbf{y}} \quad ; \qquad \mathbf{y},\hat{\mathbf{y}} \in \boldsymbol{\Theta} \tag{2.6}$$

where $\mathbf{H}$ and $\mathbf{h}$ are third order tensors representing the elastic influence function and part damage induced influence function, respectively. These influence functions are obtained from the elastic behavior of the microstructure both in the absence and presence of damage.

For reduced-order modeling, the microstructure response is described using a reduced number of degrees of freedom. By precomputing the coefficient tensors for displacement in the representative volume, the reduced-order modeling approach economizes the computational cost, as discussed by Oskay and Fish [60]. The representative volume domain, $\boldsymbol{\Theta}$, is partitioned into n non-overlapping subdomains, $\boldsymbol{\Theta}^{(\xi)}$, referred to as the failing part or damaged part, where $\xi = 1, 2, \dots n$ indicates the part number. Mathematically, it can be expressed as given by,

$$\boldsymbol{\Theta} \equiv \bigcup_{\xi=1}^{n} \boldsymbol{\Theta}^{(\xi)} \quad ; \quad \boldsymbol{\Theta}^{(\xi)} \bigcap \boldsymbol{\Theta}^{(\delta)} \equiv \emptyset \qquad \forall\ \xi \neq \delta \tag{2.7}$$

The reduced-order model is partitioned to avoid parts with no intersecting constituent phase, as shown in Equation (2.8). The parts of the representative volume are partitioned to enable grouping of the similar regions of the microstructure corresponding to the macroscopic failure modes.

$$\boldsymbol{\Theta}_\iota^{(\xi)} \bigcap \boldsymbol{\Theta}_\varrho^{(\xi)} \equiv \emptyset \qquad \forall\ \iota \neq \varrho \tag{2.8}$$

In this equation, the subscripts ι and ϱ identify the constituent phases in a subdomain $\boldsymbol{\Theta}^{(\xi)}$ or damaged part, ξ . Implementation of a reduced order model for a unidirectionally reinforced fiber composite is described in Section 5.3.

Shape functions, $N^{(\xi)}$, are defined as piecewise constant functions, which form a partition of unity in the characteristic volume (i.e. $N^{(\xi)} = 1$ if $\mathbf{y} \in \boldsymbol{\Theta}^{(\xi)}$ and 0 otherwise). The reduced basis representation for damage fields, ω and damage induced inelastic fields, $\boldsymbol{\mu}$, of n^{th} order reduced basis are represented as follows,

$$\omega(\mathbf{x},\mathbf{y},t) = \sum_{\xi=1}^{n} N^{(\xi)}(\mathbf{y})\omega^{(\xi)}(\mathbf{x},t) \tag{2.9}$$

$$\boldsymbol{\mu}(\mathbf{x},\mathbf{y},t) = \sum_{\xi=1}^{n} N^{(\xi)}(\mathbf{y})\boldsymbol{\mu}^{(\xi)}(\mathbf{x},t) \tag{2.10}$$

In Equation (2.6), the microscale displacement field is decomposed into linear and damage-induced components. (Ref. Crouch and Oskay [17]). The governing equation of the representative volume takes the form:

$$\int_{\Theta} \Big(1-\omega(\mathbf{x},\mathbf{y},t)\Big)\mathbf{g}(\mathbf{y},\hat{\mathbf{y}})\ \mathbf{C}(\mathbf{y})\cdot\Big[\mathbf{A}(\mathbf{y}):\bar{\boldsymbol{\epsilon}}(\mathbf{x},t)+\widetilde{\boldsymbol{\epsilon}}(\mathbf{x},\mathbf{y},t)\Big]d\mathbf{y}=0 \tag{2.11}$$

where the fourth-order damage polarization tensor, $\mathbf{g}$, is given by

$$\mathbf{g}(\mathbf{y},\hat{\mathbf{y}}) = \nabla^s_{\mathbf{y}}\mathbf{h}(\mathbf{y},\hat{\mathbf{y}}) \tag{2.12}$$

The fourth-order elastic strain concentration tensor, $\mathbf{A}$, is expressed as:

$$\mathbf{A} = \mathbf{I} + \mathbf{G}(\mathbf{y}) \tag{2.13}$$

where $\mathbf{I}$ is the fourth order identity tensor and $\mathbf{G}$ is the elastic polarization tensor, evaluated as:

$$\mathbf{G} = \nabla^s_{\mathbf{y}}\mathbf{H} \tag{2.14}$$

The damage induced strain, $\widetilde{\boldsymbol{\epsilon}}$, can be explicitly expressed as:

$$\widetilde{\boldsymbol{\epsilon}} = \nabla^s_{\mathbf{y}}\tilde{\boldsymbol{u}} = \sum_{\xi=1}^{n}\widetilde{\mathbf{P}}^{(\xi)}(\mathbf{y}) : \boldsymbol{\mu}^{(\xi)}(\mathbf{x},t)$$

where,

$$\widetilde{\mathbf{P}}^{(\xi)}(\mathbf{y}) = \int_{\Theta^{(\xi)}} \mathbf{g}(\mathbf{y},\check{\mathbf{y}})N^{(\xi)}(\check{\mathbf{y}})\ d\check{\mathbf{y}} \quad ; \qquad \mathbf{y},\check{\mathbf{y}} \in \boldsymbol{\Theta} \tag{2.15}$$

2.2 Macroscale Boundary Value Problem

The macroscale equilibrium and kinematic equations as well as boundary conditions under quasi-static conditions are as follows:

$$\nabla\cdot\overline{\boldsymbol{\sigma}}(\mathbf{x},t) + \overline{\mathbf{b}}(\mathbf{x}) = 0; \quad t \in [0,t_{\mathrm{f}}] \tag{2.16}$$

$$\bar{\boldsymbol{\epsilon}}(\mathbf{x},t) = \nabla^s\bar{\mathbf{u}}(\mathbf{x},t) \tag{2.17}$$

$$\bar{\mathbf{u}} = \hat{\mathbf{u}}(\mathbf{x},t) \quad \mathbf{x}\in\Gamma_u \qquad \overline{\boldsymbol{\sigma}}\cdot\mathbf{n} = \hat{\mathbf{t}}(\mathbf{x},t) \quad \mathbf{x}\in\Gamma_t \tag{2.18}$$

where $\overline{\boldsymbol{\sigma}}$ is the homogenized Cauchy stress field and $\overline{\mathbf{b}}$ is the body force. The spatial and temporal coordinates are $\mathbf{x}$ and t. $\bar{\mathbf{u}}$ is the macroscale displacement field. The displacement and traction boundary are denoted as $\hat{\mathbf{u}}$ and $\hat{\mathbf{t}}$, respectively. $\nabla \cdot (\cdot)$ and $\nabla^s(\cdot)$ are the divergence and symmetric gradient operators, respectively.

2.3 Microscale Boundary Value Problem

Given the macroscale strain state, $\bar{\boldsymbol{\epsilon}}$, and damage measure, $\omega^{(\xi)}$, in each damaged part, ξ, of the microstructure defined by the evolution equations for part-averaged damage, the evolution of microscopic damage is described by continuum damage mechanics based on the history-dependent strain state in each damaged part and is stored as an internal state variable in the macroscale model. The unknown eigenstrains in each damaged part, $\boldsymbol{\mu}^{(\xi)}$, are obtained using Equation (2.19):

$$\sum_{\Delta=1}^{n} \left\{ \left(1 - \omega^{(\xi)}\right) \left[\mathbf{B}^{(\delta\Delta)} : \bar{\boldsymbol{\epsilon}} + \sum_{\xi=1}^{n} \mathbf{F}^{(\delta\Delta\xi)} : \boldsymbol{\mu}^{(\xi)} \right] \right\} = 0 \quad \forall\, \delta = 1, 2, \ldots, n \tag{2.19}$$

Here, n is the number of damaged parts in $\boldsymbol{\Theta}$. The homogenized macroscopic stress is computed as a function of part averaged damage and eigenstrain coefficients, as given below:

$$\overline{\boldsymbol{\sigma}} = \sum_{\xi=1}^{n} \left(1 - \omega^{(\xi)}\right) \left[\overline{\mathbf{L}}^{(\xi)} : \bar{\boldsymbol{\epsilon}} + \sum_{\delta=1}^{n} \overline{\mathbf{P}}^{(\delta\xi)} : \boldsymbol{\mu}^{(\delta)} \right] \tag{2.20}$$

In Equations (2.19) and (2.20), $\mathbf{B}^{(\delta\Delta)}$, $\mathbf{F}^{(\delta\Delta\xi)}$, $\overline{\mathbf{L}}^{(\xi)}$ and $\overline{\mathbf{P}}^{(\delta\xi)}$ are coefficient tensors due to Bhattacharyya and Basu [7] defined as follows:

$$\mathbf{B}^{(\delta\Delta)} = \int_{\Theta^{(\Delta)}} \widetilde{\mathbf{P}}^{(\delta)}(\mathbf{y}) : \mathbf{C}(\mathbf{y}) : \mathbf{A}(\mathbf{y}) N^{(\Delta)} \, d\mathbf{y} \tag{2.21}$$

$$\mathbf{F}^{(\delta\Delta\xi)} = \int_{\Theta^{(\Delta)}} \widetilde{\mathbf{P}}^{(\delta)}(\mathbf{y}) : \mathbf{C}(\mathbf{y}) : \widetilde{\mathbf{P}}^{(\xi)} N^{(\Delta)} \, d\mathbf{y} \tag{2.22}$$

$$\overline{\mathbf{L}}^{(\xi)} = \frac{1}{|\Theta|} \int_{\Theta^{(\xi)}} \mathbf{C}(\mathbf{y}) : \mathbf{A}(\mathbf{y}) \; N^{(\xi)} \, d\mathbf{y} \tag{2.23}$$

$$\overline{\mathbf{P}}^{(\delta\xi)} = \frac{1}{|\Theta|} \int_{\Theta^{(\delta)}} \mathbf{C}(\mathbf{y}) : \widetilde{\mathbf{P}}^{(\xi)}(\mathbf{y}) \; N^{(\delta)} \, d\mathbf{y} \tag{2.24}$$

Since the microstructural morphology and elastic constants of the constituents are treated as deterministic, the coefficient tensors are also deterministic. The homogenized macroscopic stress in Equation (2.20) constitutes a stress update in the solution for the macroscale boundary value problem.

2.4 Numerical Implementation of Microscale Boundary Value Problem

In this section, implementation at microscale is discussed in detail. The governing equations for mathematical homogenization were discussed in the previous section. The weak form of these governing equations and corresponding finite element approximation for three dimensional simulation are presented here.

2.4.1 The Reduced Order Model

Progressive damage evaluation of the composite involves analysis at two different scales - micro and macro. These two analyses are undertaken separately. The Graphical User Interface (GUI) in the commercially available software Abaqus 6.14 is used for creating the morphology of the representative unit cell and the macroscale coupons. The microscale analysis is performed using the in-house `CoefTensCompute`, developed by Crouch and Oskay [17]. The macroscale analysis was undertaken using the user-defined material model subroutine capability of Abaqus. The microscale analysis of a composite representative volume is performed prior to the simulation as a preprocessing step. The geometry of the microstructure and corresponding reduced-order model parts are generated first.

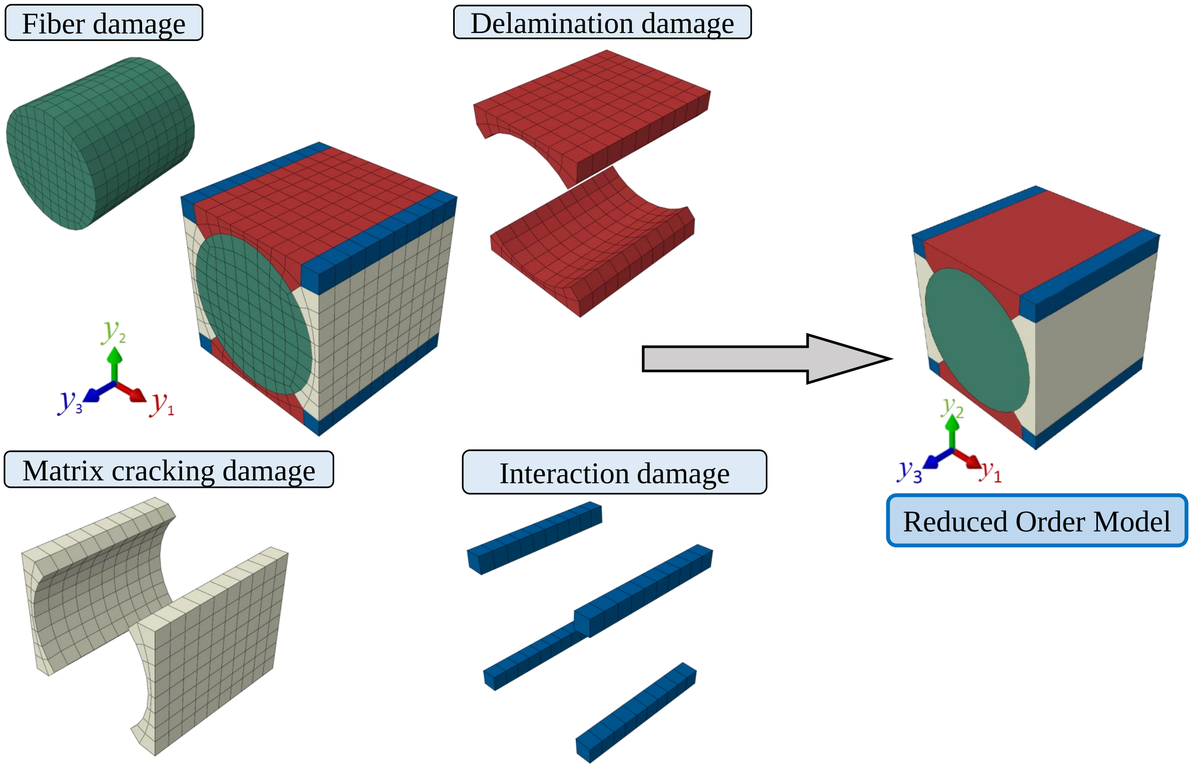

Figure 2.2: Partitioning of the representative volume and Reduced Order Model

The inputs to the microstructural analysis are the morphology of the representative volume (e.g. cell type, fiber volume fraction) and the constituent material elastic parameters. In this study a square packed fiber composite microstructure is assumed. Accordingly a representative volume consisting of the matrix and fiber material phases is modeled to represent the microstructure of the unidirectionally reinforced composite of approximately 65% fiber volume fraction. The microstructure domain of size $10\mu m \times 10\mu m \times 10\mu m$ is discretized with 1640 hexahedron (also referred as C3D8) elements and 2035 nodes. This representative volume is then partitioned (Figure 2.2) into 4 self-uniform damaged parts correspond to the macroscale failure modes of the composite, namely, fiber failure, transverse matrix cracking, and delamination. The 'interaction damage' part represents the maximum damage accumulated in either, transverse matrix cracking or, delamination. The 'fiber damage' part consists of 960 elements and 1243 nodes. The 'matrix cracking' and 'delamination' parts consist of 320 elements and 594 nodes. The 'interaction part' part consists of 40 elements and 176 nodes. Unlike Crouch and Oskay [17] and Bogdanor and Oskay [9], perfect bonding is assumed at the interface and no additional interfacial properties between the fiber and matrix within the representative volume were considered. For microscale analysis all 8 vertex nodes are assigned as fixed in all three directions. In the next step periodicities in the representative volume are identified. The periodicity of displacements on the boundaries of the representative volume are accounted for by identifying edge periodicity and face periodicity. The resulting following two steps solely for computational convenience.

1. **Edge periodicity:** In the representative volume element there are 4 edges parallel to each spatial coordinate. Considering one spatial direction (e.g. Z-direction) one among the four edges is assigned as 'master edge' and rest three edges are assigned as the 'slave edges'. An injective mapping is performed for 'master edge nodes' to 'slave edge nodes'. In Figure 2.3a, the nine nodes marked with solid blue circles on the edge highlighted with a blue line which is parallel to the Z-axis are termed as master nodes. The remaining three edges parallel to z-axis are marked with nine open red circles and are termed as slave edge nodes. Likewise, master and slave nodes are identified in remaining eight edges, parallel to x- and y-axes. The edges parallel to x-axis is marked in red and the ones parallel to y-axis in pink. Master-slave node pairing is also done for the edges parallel to X and Y directions.

2. **Face periodicity:** In face periodicity 3 pairs of faces are parallel to XY, YZ and ZX planes. As for example, Z- plane face periodicity is shown in Figure 2.3b. All the nodes on the back faces of the cube are considered as 'face master node'. Corresponding slave nodes on the front face in XY plane are marked with orange circles. Similar face

periodicity is evident for the other two pair of planes. In mathematical sense, this again is injective mapping.

These definitions ensured the periodicity of the representative volume during coefficient tensor computation. In this step, Abaqus compatible input file (`Input_filename.inp`) is converted to an in-house code '`CoefTensCompute`' compatible file (`MicroInput.inp`) using a Python script (named as `AbaInp2MicroInp_conversion.py`) written for the purpose. Node and element sets are predefined in the Abaqus compatible input file. All the node and element descriptions are processed first. Next, the assembled element and node sets are identified. Finally, the representative volume discretized with 1640 finite elements, and four damage parts, as shown in Figure 2.2, is efficiently analyzed as a reduced order model.

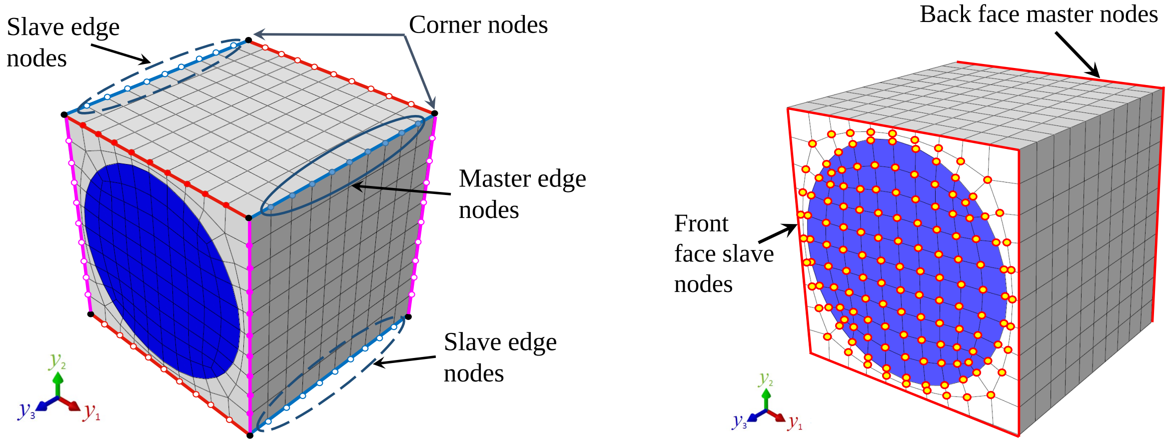

(a) Edge periodicity scheme (b) Face periodicity scheme for Z-plane

Figure 2.3: Pictorial representation of the concept of periodicity

2.4.2 Solving the Unit Cell Problems

The first step in the homogenization process is the evaluation of elastic and phase influence functions, which are third-order tensors. To solve these problems the governing equations need to be written in the weak form. Let $\hat{\boldsymbol{\Theta}}$ be an arbitrary subdomain of $\boldsymbol{\Theta}$ and $\mathbf{w} \in \mathscr{W}$ is the weight function; and $\mathscr{W} = \left\{\mathbf{w} \in \mathbb{H}^1(\boldsymbol{\Theta}) \middle| \mathbf{w} \text{ is } \boldsymbol{\Theta} - \text{periodic}\right\}$, where $\mathbb{H}$ is a Hilbert space. The weak-form for elastic influence function problem can be written as Eq. 2.25, as detailed in Ref. [34].

$$\int_{\boldsymbol{\Theta}} \nabla_{\mathbf{y}} \mathbf{w}(\mathbf{y}) : \mathbf{C}(\mathbf{y}) : \mathbf{G}(\mathbf{y}, \hat{\mathbf{y}}) : \boldsymbol{\epsilon}(\mathbf{x}) \, d\boldsymbol{\Theta} + \int_{\boldsymbol{\Theta}} \nabla_{\mathbf{y}} \mathbf{w}(\mathbf{y}) : \mathbf{C}(\mathbf{y}) : \boldsymbol{\epsilon}(\mathbf{x}) \, d\boldsymbol{\Theta} = 0 \qquad (2.25)$$

The trial function $\mathbf{w}$ and the elastic influence function $\mathbf{H}$ are approximated as:

$$\mathbf{w}(\mathbf{y}) = \mathbf{N}(\mathbf{y})\ C \tag{2.26}$$

$$\mathbf{H}(\mathbf{y}) = \mathbf{N}(\mathbf{y})\ \mathbf{d} \tag{2.27}$$

where, $\mathbf{N}$ is the element shape function matrix. $\mathbf{d}$ and C denote nodal degrees of freedom of trial and weight functions. The strain-displacement relationship matrix, $\boldsymbol{\mathcal{B}}$, can be written as:

$$\boldsymbol{\mathcal{B}}(\mathbf{y}) = \nabla_{\mathbf{y}}\mathbf{N}(\mathbf{y}) \tag{2.28}$$

The elastic polarization tensor, $\mathbf{G}$ is:

$$\mathbf{G}(\mathbf{y}) = \boldsymbol{\mathcal{B}}(\mathbf{y})\mathbf{d} \tag{2.29}$$

Finally the, discrete form of the governing elastic influence function problem is solved for $\mathbf{d}$ as shown below:

$$[\mathbf{K}]\{\mathbf{d}\} = -\{\mathbf{f}\} \tag{2.30}$$

where,

$$\mathbf{K} = \int_{\boldsymbol{\Theta}} \boldsymbol{\mathcal{B}}^{\mathsf{T}}(\mathbf{y}) : \mathbf{C}(\mathbf{y}) : \boldsymbol{\mathcal{B}}(\mathbf{y})\ d\boldsymbol{\Theta} \tag{2.31}$$

and

$$\mathbf{f} = \int_{\boldsymbol{\Theta}} \boldsymbol{\mathcal{B}}^{\mathsf{T}}(\mathbf{y}) : \mathbf{C}(\mathbf{y})\ d\boldsymbol{\Theta} \tag{2.32}$$

For microscale analysis, all eight corner nodes are assumed as fixed in all three directions. In matrix notation, the degrees of freedom for corner nodes $\mathbf{d}_{\mathrm{c}}$ is set as $\mathbf{d}_{\mathrm{c}} = 0$. Thereafter, the periodicities in the representative unit cell are identified. The periodicity of displacements on the boundaries of the representative cell are enforced. In the RUC there are 4 edges parallel to each spatial coordinate. Considering one spatial direction (say, y_3-direction), one of the four edges is designated as the 'master edge' and the remaining three parallel edges are designated as 'slave edges'. An injective mapping is performed from 'master edge nodes' to 'slave edge nodes'. In Fig. 2.4, the nine nodes marked with solid blue circles on the edge highlighted with a blue line which is parallel to the y_3-axis are termed as master nodes. The remaining three edges parallel to y_3-axis marked with nine open red circles are termed as slave edge nodes. Likewise, master and slave nodes are identified in the remaining eight edges, parallel to y_1- and y_2-axes. The edges parallel to y_1-axis is marked in red and the ones parallel to y_2-axis in pink. Master-slave node pairing is also done for the edges parallel to y_1 and y_2 directions. In addition to the edges, 3 pairs of faces parallel to y_1y_2, y_2y_3 and

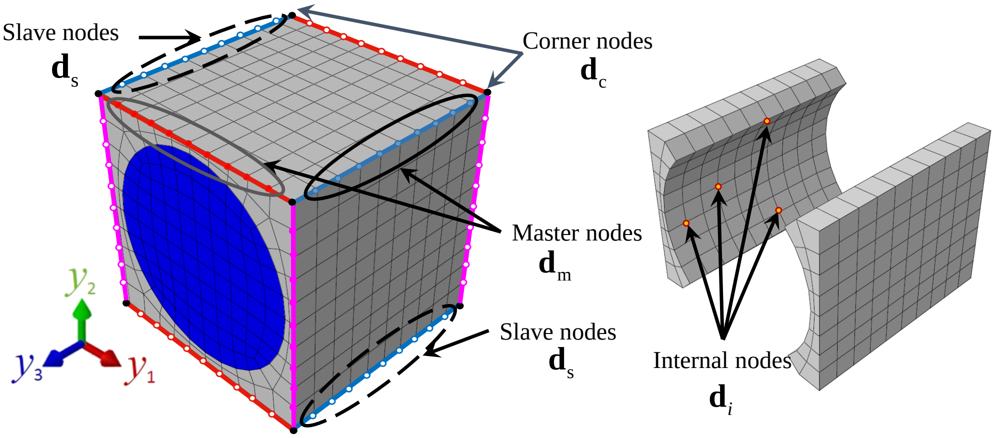

Figure 2.4: Pictorial representation of the concept of periodicity

$y_3 y_1$ planes are considered. All the nodes on the back faces of the domain in Fig. 2.4 are considered as 'face master nodes'. Corresponding slave nodes are on the front face in the $y_1 y_2$ plane. Similar face periodicities are identified for the faces corresponding to y_2- and y_3-planes. In mathematical sense, this again is injective mapping.

The degrees of freedom for master and slave nodes are denoted by $\mathbf{d}_\mathrm{m}$ and $\mathbf{d}_\mathrm{s}$ respectively. All degrees of freedom other than $\mathbf{d}_\mathrm{c}$, $\mathbf{d}_\mathrm{m}$ and $\mathbf{d}_\mathrm{s}$ are considered as internal degrees of freedom and denoted by $\mathbf{d}_\mathrm{i}$. After imposing the corner node fixity boundary condition by setting $\mathbf{d}_\mathrm{c} = 0$, the degrees of freedom are rearranged in the following form:

$$\mathbf{d} = \{\mathbf{d}_\mathrm{m}, \mathbf{d}_\mathrm{s}, \mathbf{d}_\mathrm{i}\}^\intercal \tag{2.33}$$

The microscale mesh periodicity requires enforcing another boundary condition:

$$\mathbf{d}_\mathrm{s} = \mathbf{d}_\mathrm{m} \tag{2.34}$$

Applying variational principle, the energy functional, $\Pi(\mathbf{d})$, becomes:

$$\Pi(\mathbf{d}) = \frac{1}{2}\mathbf{d}^\intercal \mathbf{K} \mathbf{d} - \mathbf{d}^\intercal \mathbf{f} + \lambda^\intercal (\mathbf{d}_\mathrm{m} - \mathbf{d}_\mathrm{s}) \tag{2.35}$$

where, λ is the Lagrange multiplier. The minimum energy equations can now be obtained by taking the derivative of Eq. 2.35 with respect to $\mathbf{d}$ and set to zero. The set of equations so obtained are:

$$\mathbf{K}_\mathrm{mm}\mathbf{d}_\mathrm{m} + \mathbf{K}_\mathrm{ms}\mathbf{d}_\mathrm{s} + \mathbf{K}_\mathrm{mi}\mathbf{d}_\mathrm{i} - \mathbf{f}_\mathrm{m} + \lambda^\intercal = 0 \tag{2.36}$$

$$\mathbf{K}_\mathrm{sm}\mathbf{d}_\mathrm{m} + \mathbf{K}_\mathrm{ss}\mathbf{d}_\mathrm{s} + \mathbf{K}_\mathrm{si}\mathbf{d}_\mathrm{i} - \mathbf{f}_\mathrm{s} + \lambda^\intercal = 0 \tag{2.37}$$

$$\mathbf{K}_{\mathrm{im}}\mathbf{d}_{\mathrm{m}} + \mathbf{K}_{\mathrm{is}}\mathbf{d}_{\mathrm{s}} + \mathbf{K}_{\mathrm{ii}}\mathbf{d}_{\mathrm{i}} - \mathbf{f}_{\mathrm{i}} = 0 \tag{2.38}$$

Applying static condensation and enforcing mesh periodicity (Eq. 2.34), a set of discrete equations are obtained as in Eq. 2.39. These equations can be solved simultaneously to obtain $\mathbf{d}_{\mathrm{m}}$ and $\mathbf{d}_{\mathrm{i}}$.

$$\begin{bmatrix} (\mathbf{K}_{\mathrm{mm}} + \mathbf{K}_{\mathrm{ms}} + \mathbf{K}_{\mathrm{sm}} + \mathbf{K}_{\mathrm{ss}}) & (\mathbf{K}_{\mathrm{mi}} + \mathbf{K}_{\mathrm{si}}) \\ (\mathbf{K}_{\mathrm{mi}} + \mathbf{K}_{\mathrm{si}}) & \mathbf{K}_{\mathrm{ii}} \end{bmatrix} \begin{Bmatrix} \mathbf{d}_{\mathrm{m}} \\ \mathbf{d}_{\mathrm{i}} \end{Bmatrix} = \begin{Bmatrix} \mathbf{f}_{\mathrm{m}} + \mathbf{f}_{\mathrm{s}} \\ \mathbf{f}_{\mathrm{i}} \end{Bmatrix} \tag{2.39}$$

From this solution the elastic polarization function, $\mathbf{H}$, can be extracted. Similarly, the weak-form for the phase damage influence function problem is written as Eq. 2.40 and solved for $\mathbf{g}$.

$$\int_{\boldsymbol{\Theta}} \nabla_{\mathbf{y}} \mathbf{w}(\mathbf{y}) : \mathbf{C}(\mathbf{y}) : \mathbf{g}(\mathbf{y}, \hat{\mathbf{y}}) : \boldsymbol{\epsilon}(\mathbf{x}) \, d\boldsymbol{\Theta} + \int_{\hat{\boldsymbol{\Theta}}} \nabla_{\mathbf{y}} \mathbf{w}(\mathbf{y}) : \mathbf{C}(\mathbf{y}) : \boldsymbol{\epsilon}(\mathbf{x}) \, d\boldsymbol{\Theta} = 0; \hat{\mathbf{y}} \in \hat{\boldsymbol{\Theta}} \tag{2.40}$$

2.4.3 Computation of Coefficient Tensors

The coefficient tensors for the composite reduced order model are computed using `CoefTensCompute` as described below.

i) The geometrical features of the representative volume domain and elastic material parameters are the input.

ii) Elastic and part damage polarization functions are computed using Equations (2.12) and (2.14). Coefficient tensors $\mathbf{A}$ and $\widetilde{\mathbf{P}}$ are also computed in this step using Equations (2.13) and (2.15).

iii) Partitioning of damaged part for the representative volume is constructed.

iv) Coefficient tensors $\mathbf{B}$, $\mathbf{F}$, $\overline{\mathbf{L}}$ and $\overline{\mathbf{P}}$ are obtained using Equations (2.21) to (2.24).

v) Finally, all the coefficient tensors are transferred to an output file.

2.5 Alleviation of Spurious Residual Stiffness

The reduced order microstructure problem constitutes a full nonlinear system that is used to evaluate the microstructural behavior. If low order models are used, this approach has been shown to demonstrate a significant post-peak residual stiffness Crouch and Oskay [17] and Bogdanor and Oskay [9]. The residual stiffness is spurious and must be alleviated to ensure accurate load redistribution in a failure propagation scenario. This issue has been tied to the concept of the incompatibility of the eigenstrains as described in Furuhashi and Mura [29] and Fish *et al.* [28]. The coefficient tensors with degraded constituent properties in the damage path represents cracking across the microstructural domain, which in turn eliminates the corresponding stiffness properties of the composite material in the appropriate loading direction. The identification of failure path and implementation of modified coefficient tensors for the reduced order model is described in depth in Sparks and Oskay [80]. For the sake of brevity, minimally required mathematical details are presented. In addition, implementation of a generalized "m-th order" failure path approach is considered. The proposed approach needs storage of m additional sets of modified coefficient tensors, which are also computed prior to the macroscale analysis. This implementation poses insignificant additional computational cost at the macroscale.

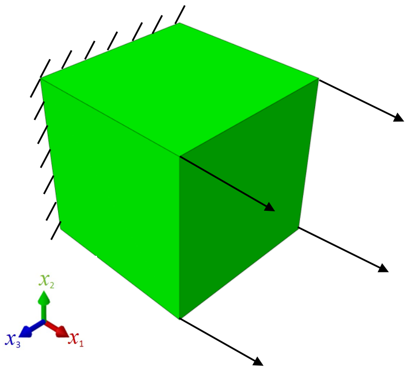

Figure 2.5: One element model for verification

The capability of the proposed approach is demonstrated with only "first order" numerical verification study. A unidirectionally reinforced composite subjected to uniaxial loading along the vertical (transverse) direction is considered. The geometry of the verification example is illustrated in Figure 2.5. The boundary conditions are chosen to be symmetric on three sides of the domain. As shown in Figure 2.2, the reduced order model used in this study consist of four parts. The macroscale discretization consists of a single linear hexahedron. The analyses were performed using both full integration and reduced integration elements. The nodes on the right side face of the geometry are subjected to displacement controlled loading with the maximum amplitude of 0.50 mm.

In this analysis the predominant failure mode is matrix cracking (i.e., the failure in matrix damage part). The stress vs. strain plot corresponding to stated loading direction is shown in Figure 2.6a. The figure clearly demonstrates an irregular stress pattern beyond failure in the matrix cracking part of the reduced order model and residual stress for the macroscale element. The origin of the irregular stress pattern can be attributed to the presence of residual stresses.

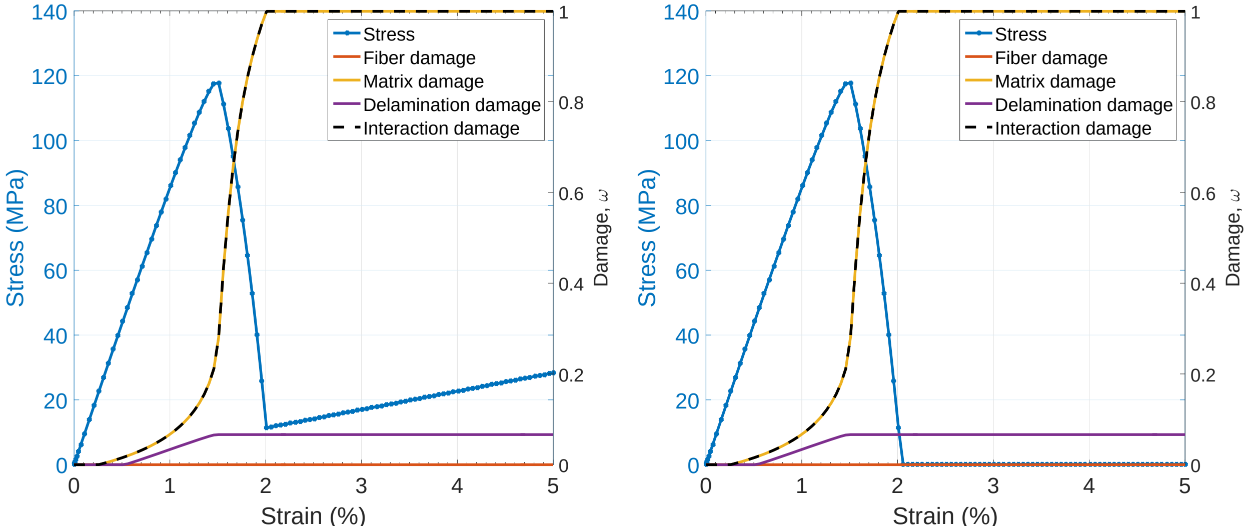

(a) Before using modified coefficient tensor

(b) After using modified coefficient tensor

Figure 2.6: Structural scale stress-strain plots under unidirectional loading

Despite the failure observed in the matrix-cracking part, on further loading of the remainder of the fiber and delamination damage parts, residual stresses continue to persist due to spurious stiffness effect ultimately culminating into failure. The progressive failure of the remainder of the damage parts results in a prolonged failure process. To remove the post-failure residual stresses, modified coefficient tensors are computed corresponding to delamination damage prior to macroscale analysis. The stress vs. strain plots in Figure 2.6b shows that both irregular stress patterns and residual stresses are effectively removed. This approach is further enhanced within the model for failure of each damage part as well as in the failure of combination of several damaged parts.

2.6 Enhancement of Computational Efficiency

The hierarchical multiscale framework used in this research follows a sequential algorithmic structure. The numerical problem at microscale, as described in Section 2.4, is solved in the following steps.

1. Preprocessing of input data
2. Solution of the Elastic Unit Cell problem
3. Solution of the Part damage Unit Cell problem
4. Evaluation of Elastic polarization function
5. Evaluation of Part polarization function

6. Computation of coefficient tensors

Among these steps, solving the Part damage Unit Cell problem consumes a much higher computing time in comparison with the other steps. To improve the computational cost, parallel programming is used. Fundamentally, parallel programming is more involved than sequential programming.

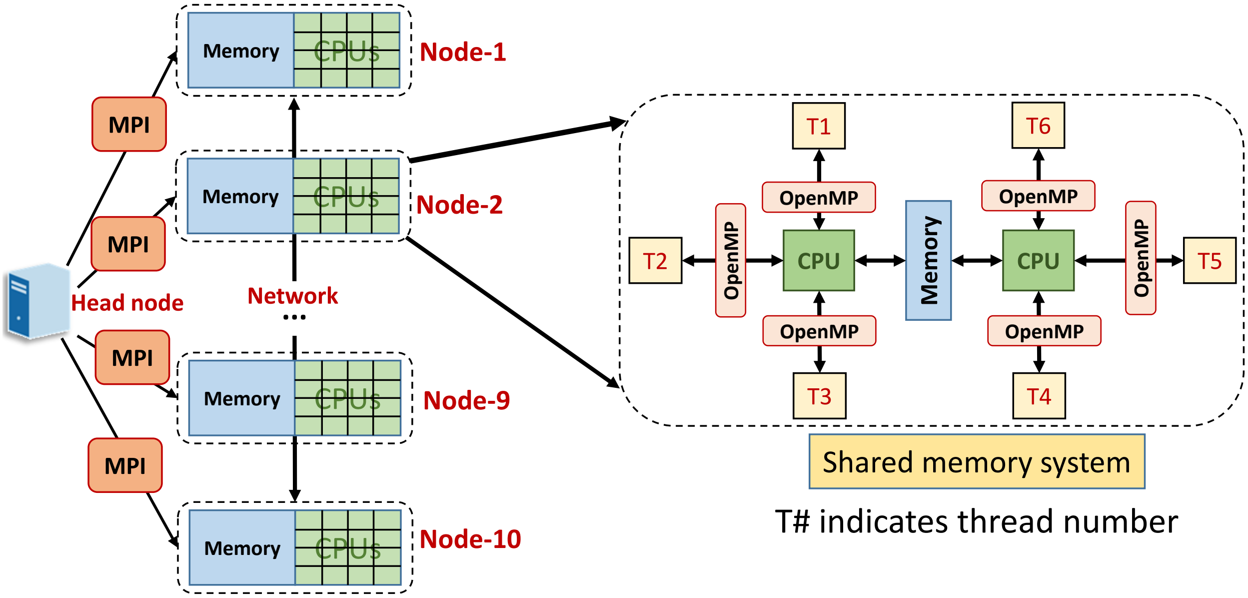

Figure 2.7: Computer architecture for parallel computing on a cluster

2.6.1 Parallel Computing Framework

In order to realize the `OpenMP` like that of Ref. [19], the API is implemented to enable multi-threaded, shared memory parallelism, because of three major advantages. First, `OpenMP` is high-level API to automate multi-threading. Second, unlike `Pthreads` which is thread based, `OpenMP` is task-based that allocates the same number of threads as the available number of cores. Finally, `OpenMP` has an important advantage over `MPI` which makes it possible to start with a sequential code, and transform it by incremental parallelization. These three aspects of `OpenMP` will lead to an efficient, scalable and effective solution. A common setup of clusters uses distributed memory nodes, where each node contains several sockets, which share memory. This suggests that `MPI` allows communicate between the nodes (inter-node communication) and `OpenMP` invokes parallelism on the nodes (intra-node communication). Based on these considerations,the microscale analysis is undertaken on a cluster as shown in Fig. 2.7. Several `OpenMP` directives were used within the Fortran code for microstructure analysis. `OpenMP` implementation for phase damage polarization function evaluation is created as a pseudo-code as shown in Listing 2.1. The processors assigned required number of threads to perform the calculations. An alternative way would have been the replacement of the `omp do` (in line 6) by specifically assigning the number of elements to each thread for computation. In that case, the sheared variables should also be assigned accordingly. In the first approach the original structure of the sequential program remains unaffected. Finally, the thread safety was verified by comparing the result with sequential program.

```
 1 USE omp_lib
 2 start_time = omp_get_wtime()
 3 ALLOCATE (Pol_Ph(ndim,ndim*nel,ngp,nel))
 4 !$omp parallel private(tid, i, m, igp, PDp) shared(Node,ElConn)
 5 tid=omp_get_thread_num()
 6 !$omp do
 7 DO iel = 1, nel
 8      nen = SIZE (ElConn(iel)%nodes)
 9      ngp = SIZE (ElConn(iel)%DetJ, DIM = 1)
10      ALLOCATE (PDp (nen*nsd, ndim*nel))
11   DO k = 1, nen
12        PDp((k-1)*nsd+1:k*nsd,:) = Node(ElConn(iel)%nodes(k))%PDp(:,:)
13   END DO
14   DO igp = 1, ngp
15        Pol_Ph(:,:,igp,iel) = MATMUL (ElConn(iel)%B_Mat(:,:,igp),PDp)
16   END DO
17      DEALLOCATE (PDp)
18 END DO
19 !$omp end do
20 !$omp end parallel
21 end_time = omp_get_wtime()
22 WRITE (*,'(A20,F20.4)') 'Pol_Ph_time:',end_time-start_time
```

Listing 2.1: Evaluation of phase damage polarization function

2.6.2 Evaluation of Computational Efficiency

The effectiveness of implementing parallel computing tool is quantified in terms of speedup and computational efficiency. In this study the communication overhead for synchronizing processors is ignored. Let T_n and T_1 denote the wall time between the start and end of the computation on a machine that has N_p processors and single processor respectively. It is evident that $T_n \leq T_1$. The gain in computing speed made by parallel execution compared to sequential execution is referred to as *speedup ratio* (S_p).

$$S_p = \frac{T_1}{T_n} \tag{2.41}$$

A perfect liner speedup can be obtained when $S_p = N_p$. In practice, a super-linear speedup, i.e. $S_p \leq N_p$ can also be achieved due to memory hierarchy effect. An algorithm which demonstrates linear speedup is said to be scalable. The efficiency is the measure of speedup per processor and calculated as:

$$\text{Efficiency} = \frac{S_p}{N_p} \times 100\% \tag{2.42}$$

The computational efficiency of the stochastic multiscale modeling framework proposed in this paper is presented in Sec. 2.6.3.

2.6.3 Computational Efficiency

The performance of the microscale analysis code, `CoefTensCompute`, was tested on three different computers having different hardware configurations, designated as **MC-1**, **MC-2** and **MC-3**. The configurations of all three computers are given in Table 2.1. For the purpose of parallel computing only 4 cpus were available on **MC-1**; whereas 32 cpus were used on both **MC-2** and **MC-3**. The wall time was used as the metric of computation time.

Table 2.1: Configuration of computing resources

Configuration	**MC-1**	**MC-2**	**MC-3**
Processor	Intel i5-2400	AMD Opteron	Intel Xeon E5
RAM (GB)	8	64	256
CPU	4	32	64
Thread per core	1	2	2
Core per socket	4	8	16
Socket	1	2	2
L3 cache memory (MB)	6	16	40

2.6.3.1 Microscale computation time

Wall time (in minutes) is recorded for solving phase damage unit cell problem, evaluating phase damage polarization function and computing the coefficient tensors as shown in Fig 2.8. The results shown in this figure are corresponding to single microscale realization. It is evident that with increased number of CPUs the computing time reduced significantly. This example problem demonstrates that significant improvement in computing time can be achieved by using `OpenMP` on **MC-2** and **MC-3**.

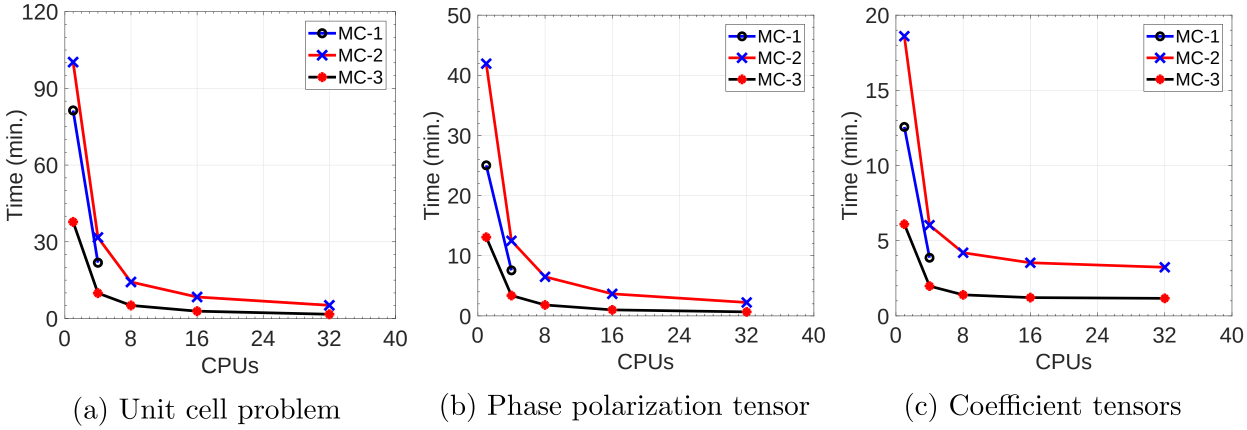

(a) Unit cell problem (b) Phase polarization tensor (c) Coefficient tensors

Figure 2.8: Computing time for each block on different computers

Adding the time for preprocessing and postprocessing of data, the total wall time (in hours) for the code `CoefTensCompute` is given in Fig. 2.9. The results show that on **MC-2**, the computing time for sequential simulation was close to 3 hours. Using parallel computing with 32 cpus, the total run time could be reduced to nearly 15 minutes. Due to higher configuration, the computer **MC-3** ran the sequential program in about an hour. Using parallel computing the run time was reduced to 5 minutes. In the case of a sampling based analysis using the stochastic framework, such performance represents significant improvement.

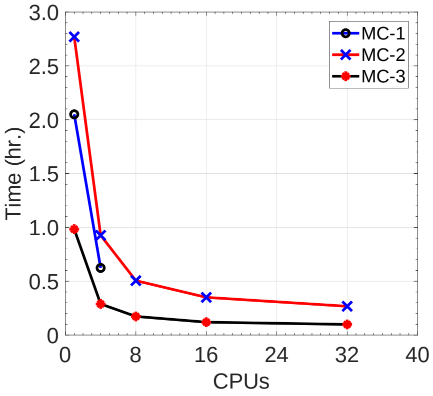

Figure 2.9: Total computing time for microscale numerical specimen

The speedup ratio and efficiency (as defined in Eqs. 2.42 and 2.41) for the microscale problem using parallel computing are presented in Table 2.2. Each of the cases is compared with the sequential code ran on the corresponding machine. It can be seen that in all the cases the speedup factor is less than the number of cpus used for multithreading. Relatively lesser efficiency is realized in the case of coefficient tensor computation, compared to solving the unit cell problem and evaluating the phase damage polarization function. This lower efficiency can be attributed to relatively lower computing time involved in coefficient tensor computation, as shown in Fig. 2.8.

Table 2.2: Computational speed up and efficiency for RUC using different hardware configurations

Computer	**MC-1**	**MC-2**				**MC-3**			
No. of CPUs	**4**	**4**	**8**	**16**	**32**	**4**	**8**	**16**	**32**
Speedup ratio									
Solving part damage UCP	3.7	3.2	7.0	11.9	19.5	3.8	7.4	13.3	22.9
Evaluating part damage polarization tensor	3.3	3.4	6.5	11.4	18.8	3.9	7.2	13.1	19.6
Computing coefficient tensors	3.3	3.1	4.4	5.3	5.8	3.1	4.4	5.0	5.2
Efficiency (%)									
Solving part damage UCP	93.2	79.1	87.9	74.6	60.8	95.2	92.6	82.8	71.5
Evaluating part damage polarization tensor	82.7	84.0	80.6	71.5	58.7	96.7	90.0	81.8	61.3
Computing coefficient tensors	81.3	77.1	55.4	32.9	18.0	76.9	54.5	31.3	16.3

CHAPTER 3

DEVELOPMENT OF CONSTITUTIVE RELATIONSHIP

In this chapter a rate-independent continuum damage evolution potential is proposed. The development of the continuum damage model is restricted to isotropic and transversely isotropic materials only. Employing the conventional formulation for continuum damage mechanics, the stress-strain relationship in each reduced-order model damage part ξ is expressed using Equation (3.1):

$$\boldsymbol{\sigma}^{(\xi)}(\mathbf{x},t) = \Big(1-\omega^{(\xi)}(\mathbf{x},t)\Big)\ \mathbf{C}^{(\xi)} : \boldsymbol{\epsilon}^{(\xi)}(\mathbf{x},t) \tag{3.1}$$

in which $\boldsymbol{\sigma}^{(\xi)}$ and $\boldsymbol{\epsilon}^{(\xi)}$ denote the part-averaged stress and strain tensors for each damage part, respectively; and $\mathbf{C}^{(\xi)}$ is the tensor of elastic moduli for the constituent (i.e., fiber or matrix) that occupies the damaged part, ξ. Damage accumulation in each constituent damaged part is driven by the phase damage equivalent strain, $\upsilon^{(\xi)}$,

$$\upsilon^{(\xi)} = \sqrt{\frac{1}{2}(\hat{\mathbf{F}}^{(\xi)}\hat{\boldsymbol{\epsilon}}^{(\xi)})^{\mathsf{T}} :\ \mathbf{C}^{(\xi)} : (\hat{\mathbf{F}}^{(\xi)}\hat{\boldsymbol{\epsilon}}^{(\xi)})} \tag{3.2}$$

where $\hat{\mathbf{F}}^{(\xi)}$ and $\hat{\boldsymbol{\epsilon}}^{(\xi)}$ represent the strain weighting matrix and the principal strain vector within damaged part ξ. The superscript T indicates the transpose operation. The strain weighting matrix is computed as:

$$\hat{\mathbf{F}}^{(\xi)}(\mathbf{x},t) = \begin{bmatrix} \hat{h}_1^{(\xi)} & 0 & 0 \\ 0 & \hat{h}_2^{(\xi)} & 0 \\ 0 & 0 & \hat{h}_3^{(\xi)} \end{bmatrix} \tag{3.3}$$

$$\hat{h}_\iota^{(\xi)} = \begin{cases} 1 & \text{if} \ \ \hat{\epsilon}_\iota^{(\xi)} > 0 \\ c^{(\xi)} & \text{otherwise} \end{cases} \qquad \text{for } \iota = 1,2,3 \tag{3.4}$$

in which $c^{(\xi)}$ is a material parameter that represents the damage anisotropy of the tensile and compressive loading in the principle directions. The part damage field, $\omega^{(\xi)}$, satisfies Eq. 3.5.

$$\omega^{(\xi)} = \Phi(\upsilon^{(\xi)}(t)) \quad ; \qquad \frac{\partial \Phi(\upsilon^{(\xi)}(t))}{\partial \upsilon} \geq 0 \tag{3.5}$$

The hardening segment of the constituent is modeled using an arctangent evolution function, whereas the softening segment is derived to follow a linear function. This damage model is referred to as the Arctangent Hardening Linear Softening (AHLS) model. A schematic stress-strain diagram is presented in Figure 3.1. The transition strain, $\epsilon_{\mathrm{tr}}^{(\xi)}$, for damaged part, ξ, is defined as a strain corresponding to the ultimate stress or a strain in the vicinity of the strain corresponding to the ultimate stress. This parameter is depends on the transition damage equivalent strain, $\upsilon_{\mathrm{tr}}^{(\xi)}$, which is an algorithmic parameter:

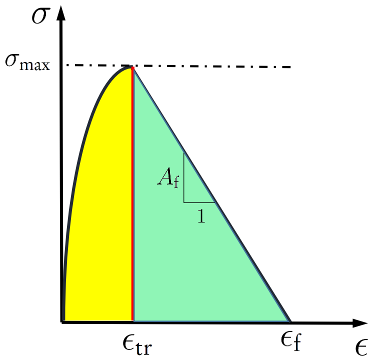

Figure 3.1: A typical representation of the stress-strain diagram for constituent

The new damage potential function is defined by two different evolution functions as given in Equation (3.6):

$$\Phi(\upsilon^{(\xi)}) = \begin{cases} 0 & \text{if } \upsilon^{(\xi)} \leq \upsilon_0^{(\xi)} \\[2ex] \dfrac{\operatorname{atan}(\alpha^{(\xi)} \langle \upsilon^{(\xi)} - \upsilon_0^{(\xi)} \rangle - \beta^{(\xi)}) + \operatorname{atan}(\beta^{(\xi)})}{\dfrac{\pi}{2} + \operatorname{atan}(\beta^{(\xi)})} & \text{if } \upsilon_0^{(\xi)} < \upsilon^{(\xi)} \leq \upsilon_{\mathrm{tr}}^{(\xi)} \\[2ex] \dfrac{\upsilon_{\mathrm{tr}}^{(\xi)}}{\upsilon^{(\xi)}} \left[\Phi\left(\upsilon_{\mathrm{tr}}^{(\xi)}\right) - \left(1 + A_{\mathrm{f}}^{(\xi)}\right) \right] + \left(1 + A_{\mathrm{f}}^{(\xi)}\right) & \text{if } \upsilon_{\mathrm{tr}}^{(\xi)} < \upsilon^{(\xi)} < \upsilon_{\mathrm{f}}^{(\xi)} \\[2ex] 1 & \text{if } \upsilon^{(\xi)} \geq \upsilon_{\mathrm{f}}^{(\xi)} \end{cases} \tag{3.6}$$

in which the damage evolution parameters, $\alpha^{(\xi)}$ and $\beta^{(\xi)}$, control the nonlinearity and strength of a damage part, ξ, depending upon the constituent material. $\upsilon_0^{(\xi)}$ is the value of the damage equivalent strain at the initiation threshold for damage, $\upsilon_{\mathrm{tr}}^{(\xi)}$ is the damage equivalent strain value at the transition point, and $\upsilon_{\mathrm{f}}^{(\xi)}$ is the damage equivalent strain value at failure. In addition to $\alpha^{(\xi)}$ and $\beta^{(\xi)}$, this model is characterized by these three damage equivalent strain parameters. $A_{\mathrm{f}}^{(\xi)}$ is the slope of the linear function in the softening regime.

3.1 Modeling Hardening Regime

One of the primary objectives of this constitutive model for the polymer matrix is to capture the strain triaxiality present in pure shear loading. The new triaxiality factor, k_b, is proposed in Bhattacharyya and Basu [7] in the form defined by Equation 3.7.

$$k_b = \left\langle \frac{(3+\nu)}{(1-\nu)} \left[\frac{\gamma_{\max}}{\left(\frac{\gamma_{\max}}{2} + \epsilon_{\max}\right)} - \frac{2(1+\nu)}{(3+\nu)} \right] \right\rangle_+ \tag{3.7}$$

where ν is the Poisson's ratio of the polymer matrix, and $\langle\cdot\rangle_+$ denote the Macaulay brackets. The numerical value of k_b for pure uniaxial loading is 0 and for pure shear loading it is 1. This new expression for triaxiality factor is expected to ease parametric calibration based on experimental data. Here, $\gamma_{\max}$ is the maximum engineering shear strain and $\epsilon_{\max}$ is the maximum absolute principal strain. For the sake of simplicity, the superscript (ξ) has been dropped. The parameters controlling damage evolution in any damaged part, ξ, are weighted as a function of the maximum principal strain, $(\epsilon_{\max})$, and maximum shear strain, $(\gamma_{\max})$, as defined below:

$$\epsilon_{\max} = \max\Big\{|\hat{\epsilon}_1|, |\hat{\epsilon}_2|, |\hat{\epsilon}_3|\Big\} \tag{3.8}$$

$$\frac{\gamma_{\max}}{2} = \frac{\max\{\hat{\boldsymbol{\epsilon}}\} - \min\{\hat{\boldsymbol{\epsilon}}\}}{2} \tag{3.9}$$

The derivation of this new triaxiality factor is shown in Appendix A.

The variables of damage evolution under an arbitrary loading state are expressed as a function of this triaxiality factor. The parameters are calibrated based on pure shear (subscript S) and pure uniaxial (subscript N) load states, as shown in Equations (3.15) to (3.17). Based on the triaxiality state of the stress, the weighting factor k_b is evaluated using Equation (3.7). Then the damage evolution parameters, $\alpha^{(\xi)}$ and $\beta^{(\xi)}$, are weighted using the triaxiality factor, k_b. The weighting parameter η is specific to a given material. These two triaxiality parameters dictate the values of parameters, α and β, which together control the extent of ductility in the hardening regime as well as the ultimate strength of the material.

$$\alpha = (k_b)^{\eta} \alpha_{\mathrm{S}} + \big(1 - \sqrt[\eta]{k_b}\big) \alpha_{\mathrm{N}} \tag{3.10}$$

$$\beta = (k_b)^{\eta} \beta_{\mathrm{S}} + \big(1 - \sqrt[\eta]{k_b}\big) \beta_{\mathrm{N}} \tag{3.11}$$

Here, α_{N}, β_{N} are the damage model parameters for pure uniaxial loading. On the other hand, α_{S}, β_{S} denote the damage model parameters for pure shear loading. Note that in these equations, the subscript N becomes T for tension and C for compression. For a specific strain state, the direction of axial loading is evaluated first and the parameters are selected accordingly. These four damage model parameters can be calibrated directly with the experiment data. In this proposed damage model, the damage evolution for each loading condition (either, pure uniaxial or, pure shear) depends on the corresponding three damage equivalent strain parameters. These parameters can be obtained using Equations (3.12) and (3.13). The details of formulation and evaluation of the damage equivalent strain parameters are given in Appendix B.

$$\upsilon_{(\cdot)}^{(\mathrm{T})} = \epsilon_{(\cdot)}^{(\mathrm{T})} \sqrt{\frac{E}{2(1+\nu)(1-2\nu)}} \sqrt{1-\nu+2\nu^2(c^2-2c)} = \epsilon_{(\cdot)}^{(\mathrm{T})} \chi_{\mathrm{T}}^{(m)} \tag{3.12}$$

$$\upsilon_{(\cdot)}^{(\mathrm{S})} = \epsilon_{(\cdot)}^{(\mathrm{S})} \sqrt{\frac{E}{2(1+\nu)(1-2\nu)}} \sqrt{(1+c^2)(1-\nu)-2\nu c} = \epsilon_{(\cdot)}^{(\mathrm{S})} \chi_{\mathrm{S}}^{(m)} \tag{3.13}$$

$$\upsilon_{(\cdot)}^{(\mathrm{C})} = \epsilon_{(\cdot)}^{(\mathrm{C})} \sqrt{\frac{E}{2(1+\nu)(1-2\nu)}} \sqrt{c^2(1-\nu)+2\nu^2(1-2c)} = \epsilon_{(\cdot)}^{(\mathrm{C})} \chi_{\mathrm{C}}^{(m)} \tag{3.14}$$

In Equations (3.12) to (3.14), E is the Young's modulus of the constituent polymer matrix material. The subscript $(\cdot)$ is a generalized representation of the damage initiation, transition and failure of the constituent matrix. The damage equivalent strain parameters corresponding to damage initiation, transition and failure under pure uniaxial loading are denoted by $\upsilon_0^{(\mathrm{N})}$, $\upsilon_{\mathrm{tr}}^{(\mathrm{N})}$ and $\upsilon_{\mathrm{f}}^{(\mathrm{N})}$, respectively. Similarly, damage equivalent strain parameters corresponding to damage initiation, transition and failure under pure shear loading are denoted by $\upsilon_0^{(\mathrm{S})}$, $\upsilon_{\mathrm{tr}}^{(\mathrm{S})}$ and $\upsilon_{\mathrm{f}}^{(\mathrm{S})}$, respectively. Under a mixed mode state of strain loading, the parameters for damage initiation, transition and failure are evaluated using Equations (3.15) to (3.17).

$$\upsilon_0 = (k_b)^\eta \upsilon_0^{(\mathrm{S})} + \big(1-(k_b)^\eta\big)\upsilon_0^{(\mathrm{N})} \tag{3.15}$$

$$\upsilon_{\mathrm{tr}} = (k_b)^\eta \upsilon_{\mathrm{tr}}^{(\mathrm{S})} + \big(1-(k_b)^\eta\big)\upsilon_{\mathrm{tr}}^{(\mathrm{N})} \tag{3.16}$$

$$\upsilon_{\mathrm{f}} = (k_b)^\eta \upsilon_{\mathrm{f}}^{(\mathrm{S})} + \big(1-(k_b)^\eta\big)\upsilon_{\mathrm{f}}^{(\mathrm{N})} \tag{3.17}$$

By extending the AHLS damage model to the case of transversely isotropic fiber, the expression for damage equivalent strain parameters is given by Equations (3.18) and (3.19).

$$\upsilon_{(\cdot)}^{(\mathrm{T})} = \epsilon_{(\cdot)}^{(\mathrm{T})} \sqrt{\frac{C_{33}+2c^2\nu_{31}^2(C_{11}+C_{12})-4c\nu_{31}C_{13}}{2}} = \epsilon_{(\cdot)}^{(\mathrm{T})} \chi_{\mathrm{T}}^{(f)} \tag{3.18}$$

$$\upsilon_{(\cdot)}^{(\mathrm{C})} = \epsilon_{(\cdot)}^{(\mathrm{C})} \sqrt{\frac{c^2 C_{33} + 2\nu_{31}^2 (C_{11} + C_{12}) - 4c\nu_{31} C_{13}}{2}} = \epsilon_{(\cdot)}^{(\mathrm{C})} \chi_{\mathrm{C}}^{(f)} \tag{3.19}$$

where, C_{11}, C_{12}, C_{13} and C_{33} are components of the tensor of elastic moduli for transversely isotropic carbon fiber. These components are given by:

$$C_{11} = \frac{E_{11}(1 - \nu_{13}\nu_{31})}{1 - \nu_{12}^2 - 2\nu_{13}\nu_{31} - 2\nu_{12}\nu_{13}\nu_{31}} \tag{3.20}$$

$$C_{12} = \frac{E_{11}(\nu_{12} + \nu_{13}\nu_{31})}{1 - \nu_{12}^2 - 2\nu_{13}\nu_{31} - 2\nu_{12}\nu_{13}\nu_{31}} \tag{3.21}$$

$$C_{13} = \frac{E_{11}(\nu_{31} + \nu_{12}\nu_{31})}{1 - \nu_{12}^2 - 2\nu_{13}\nu_{31} - 2\nu_{12}\nu_{13}\nu_{31}} \tag{3.22}$$

$$C_{33} = \frac{E_{33}(1 - \nu_{12}^2)}{1 - \nu_{12}^2 - 2\nu_{13}\nu_{31} - 2\nu_{12}\nu_{13}\nu_{31}} \tag{3.23}$$

Here, E_{33} is the longitudinal Young's modulus, E_{11} is the transverse Young's modulus, ν_{12} is the longitudinal Poisson's ratio and ν_{31} is the transverse Poisson's ratio. The derivation of above mentioned expressions is shown in Appendix C.

3.1.1 Modeling of softening regime

The underlying assumption in the damage potential model of Equation (3.6) is that the softening behavior of each reduced-order part can be modeled using a linear stress-strain law, which allows nonlinear damage evolution within the hardening regime. The damage evolution law derived here corresponds to linear softening and follows C^0 continuity. The spatial (not temporal) stress rate tensor in terms of strain-rate tensor is computed using Equation (3.24).

$$\dot{\boldsymbol{\sigma}} = (1 - \omega)\mathbf{C} : \dot{\boldsymbol{\epsilon}} - \dot{\omega}\mathbf{C} : \boldsymbol{\epsilon} \tag{3.24}$$

In order to ensure continuity, the damage model must satisfy the following constraints:

1. Damage parameter reaches unity,(i.e. complete loss of load carrying capacity) at failure strain $\Phi(\upsilon_{\mathrm{f}}) = 1$.
2. Stress remains continuous at the transition point: $\Phi(\upsilon_{\mathrm{tr}}^{-}) = \Phi(\upsilon_{\mathrm{tr}}^{+})$

The solutions of the differential equations for a polymer matrix constituent under pure uniaxial and pure shear loading are presented in Equations (3.25) and (3.26), respectively.

$$\omega^{(\mathrm{N})} = \frac{\upsilon_{\mathrm{tr}}^{(\mathrm{N})}}{\upsilon} \Big[\Phi(\upsilon_{\mathrm{tr}}^{(\mathrm{N})}) - \big(1 + A_{\mathrm{f}}^{(\mathrm{N})}\big) \Big] + \big(1 + A_{\mathrm{f}}^{(\mathrm{N})}\big) \tag{3.25}$$

$$\omega^{(\mathrm{S})} = \frac{\upsilon_{\mathrm{tr}}^{(\mathrm{S})}}{\upsilon}\Big[\Phi(\upsilon_{\mathrm{tr}}^{(\mathrm{S})}) - \big(1 + A_{\mathrm{f}}^{(\mathrm{S})}\big)\Big] + \big(1 + A_{\mathrm{f}}^{(\mathrm{S})}\big) \tag{3.26}$$

In Equations (3.25) and (3.26),

$$A_{\mathrm{f}}^{(\mathrm{N})} = \frac{\sigma_{\max}}{E\Big(\epsilon_{\mathrm{f}}^{(\mathrm{N})} - \epsilon_{\mathrm{tr}}^{(\mathrm{N})}\Big)}\ ; \qquad A_{\mathrm{f}}^{(\mathrm{S})} = \frac{\tau_{\max}(1+\nu)}{E\Big(\epsilon_{\mathrm{f}}^{(\mathrm{S})} - \epsilon_{\mathrm{tr}}^{(\mathrm{S})}\Big)}$$

where, $\sigma_{\max}$ and $\tau_{\max}$ are ultimate stress under pure uniaxial and pure shear loading. The elastic tensor in the softening regime is based on the weighted sum of the elastic contributions in pure uniaxial and pure shear loading, as shown in Equation (3.27):

$$A_{\mathrm{f}} = k_b A_{\mathrm{f}}^{(\mathrm{S})} + (1 - k_b) A_{\mathrm{f}}^{(\mathrm{N})} \tag{3.27}$$

The constituent carbon fiber is assumed to demonstrate brittle failure under uniaxial loading. The mathematical expression for damage evolution in fiber is same as Equation (3.25), with

$$A_{\mathrm{f}}^{(\mathrm{N})} = \frac{\sigma_{\max}}{C_{33}(\epsilon_{\mathrm{f}} - \epsilon_{\mathrm{tr}})} \tag{3.28}$$

The derivation of linear softening damage expression is in Appendix D.

CHAPTER 4

MODEL PARAMETER CALIBRATION UNDER UNCERTAINTY

Once the constitutive model is developed as in Chapter 3, for accurate prediction of ultimate strength the model parameters need to be calibrated. The calibration process involves quantifying the errors and estimating the unknown model parameters to minimize the difference between model predictions and experimental observations. For this purpose error models need to be built as the knowledge about the state of a composite laminate and the governing damage evolution process suffer from lack of completeness and/or accuracy [15]. In case of a mechanics-based model, the source of uncertainty in model prediction arises due to (1) aleatory uncertainty and (2) epistemic uncertainty. Aleatory uncertainty address the issues of natural variability, which is irreducible and modeled by assigning probability distributions to the variables. On the other hand, epistemic uncertainty addresses uncertainty in model form errors, model parameters, and errors in solution approximations [75]. In the calibration of model parameters with input-output data, three approaches are often used: least squares, maximum likelihood, and Bayesian calibration. In case of the Bayesian calibration, both prior information and experimental data are combined to quantify the epistemic uncertainty in the calibration result. During Bayesian calibration, Kennedy and O'Hagan [42] proposed the idea of including a discrepancy function between the model prediction and the experimental data. Inclusion of appropriate model discrepancy functions has been shown to improve the calibration of model parameters [10]. In this dissertation only the effect of epistemic uncertainty is considered.

4.1 Constitutive model parameters

The constitutive relation is characterized by 11 material parameters and 4 algorithmic parameters. Algorithmic parameters are appropriately defined to ensure desired performance of the model. Table 4.1 lists the algorithmic parameters and procedures for evaluating the parameters are given in Appendices B and C.

Table 4.1: Algorithmic parameters and their execution

Name of parameter	**Execution**
Transition strain for uniaxial tension , $\epsilon_{\mathrm{tr}}^{\mathrm{N}}$	Automated
Transition strain for pure shear loading, $\epsilon_{\mathrm{tr}}^{\mathrm{S}}$	Automated
Transition strain for uniaxial compression, $\epsilon_{\mathrm{tr}}^{\mathrm{C}}$	Automated
Triaxiality weighting parameter, η	Smooth transition in failure envelope

The constituent material parameters are calibrated for IM7/977-3 graphite epoxy composite with approximately 65% fiber volume fraction. The elastic material parameters for polymer matrix and carbon fiber are listed in Tables 4.2 and 4.3 respectively.

Table 4.2: Polymer matrix material

Parameter	**Value**
Elastic modulus, $E^{(\mathrm{m})}$ (GPa)	3.72
Poisson's ratio, $\nu^{(\mathrm{m})}$	0.37
Compression-Tension anisotropy, c	0.85
Strain to initial damage, ϵ_0	0.0055
Failure strain under uniaxial tensile loading, $\epsilon_{\mathrm{f}}^{\mathrm{N}}$	0.14
Failure strain under pure shear loading, $\epsilon_{\mathrm{f}}^{\mathrm{S}}$	0.16
Failure strain under pure uniaxial compression loading, $\epsilon_{\mathrm{f}}^{\mathrm{C}}$	0.10

Table 4.3: Carbon fiber material

Parameter	**Value**
Longitudinal elastic modulus, $E_{33}^{(\mathrm{f})}$ (GPa)	257.40
Transverse elastic modulus, $E_{11}^{(\mathrm{f})}$ (GPa)	12.45
Shear modulus, $G_{13}^{(\mathrm{f})}$ (GPa)	14.60
Longitudinal Poisson's ratio, $\nu_{12}^{(\mathrm{f})}$	0.291
Transverse Poisson's ratio, $\nu_{31}^{(\mathrm{f})}$	0.206
Compression-Tension anisotropy, c	1.4481
Strain to initial damage in tension, ϵ_0	0.0098
Strain to initial damage in compression, ϵ_0	0.0055
Failure strain under uniaxial loading, $\epsilon_{\mathrm{f}}^{\mathrm{N}}$	0.0275

Standardized ASTM uniaxial tension [1], uniaxial compression [3],and V-notch shear [2] tests were conducted at Air Force Research Laboratory. Calibration of the material parameters is accomplished using experimental data from Clay and Knoth [16]. Since the elastic material parameters can be either measured in experiments or computed from other physics models, these are considered as the model input ($\mathbf{X}$) for the computational model.

Consider a computational model, $Y_{\text{model}} = \mathcal{G}(\mathbf{X}, \boldsymbol{\theta})$, with parameters $\boldsymbol{\theta}$, and output Y_{model}. This model is constructed to predict the ultimate strength of laminate, Y, which is observed through experiments. In contrast to $\mathbf{X}$, the constitutive model parameter set $\boldsymbol{\theta}$ is considered unknown due to the lack of direct measurement or physical knowledge. The objective of model parameter calibration is to estimate these parameters based on available input–output observations. The model calibrations is schematically shown in Figure 4.1.

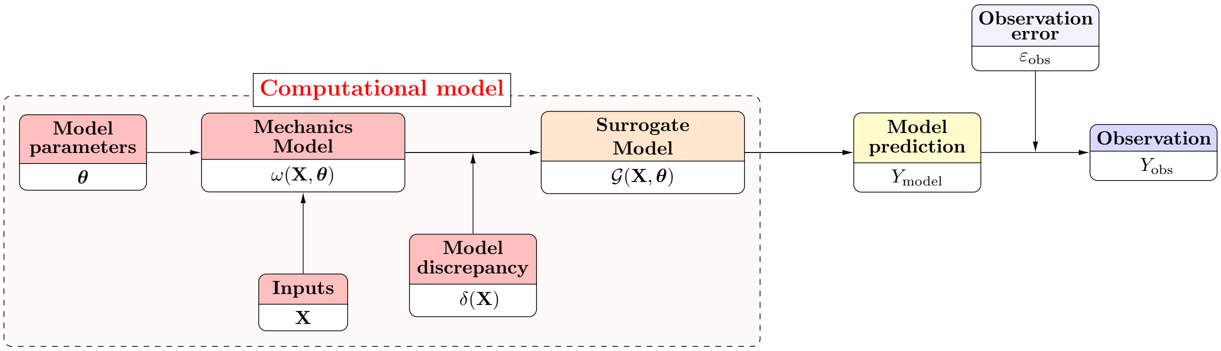

Figure 4.1: Schematic representation of model parameter calibration

Following the idea of the Kennedy-O'Hagan framework, the relationship between experimental observation Y_{obs}, true value of the quantity Y, and model output Y_{model} is described as:

$$Y_{\text{obs}} = Y + \varepsilon_{\text{obs}} \tag{4.1}$$

$$Y = Y_{\text{model}} + \delta = \mathcal{G}(\mathbf{X}_{\text{obs}}, \boldsymbol{\theta}) + \delta(\mathbf{X}_{\text{obs}}) \tag{4.2}$$

where ε_{obs} represents measurement uncertainty and is often treated as a zero-mean Guassian random variable with variance σ_{obs}^2. Uncertainty due to model inadequacy is represented by a model discrepancy term δ. Since σ_{obs} and δ are unknown, they also need to be calibrated. Here, Y_{obs} is treated as a random variable in Equation (4.1). The samples of Y_{obs} are the actual observation data of Y. Assuming p samples of Y_{obs} (denoted as $Y_{\text{obs}}^{(1)}, Y_{\text{obs}}^{(2)}, \cdots, Y_{\text{obs}}^{(p)}$) are collected for a single input setting $\mathbf{X}_{\text{obs}}$, the unknown parameters $\boldsymbol{\theta}$, σ_{obs}, and δ can be calibrated using a least square based approach.

4.2 Construction of surrogate model

To quantify the effect of multiple uncertainty sources on the prediction of ultimate strength, the computational model needs to be run repeatedly by varying the model parameters. However, the computational model mentioned in Chapter 3 is computationally expensive. To alleviate the computational cost a surrogate model, which is inexpensive approximations of the original model, need to be built to replace the mechanics-based simulation model for the purpose of uncertainty quantification analysis. Based on the loading condition and composite layup configuration, five surrogate models need to be developed. The models and corresponding parameters are shown in Table 4.4. In the model name the superscript indicates constituent material and the subscript indicates loading condition. The fiber angle orientation is denoted as φ. The tensile and compressive loading in the laminates are written as f_T and f_C, respectively.

Table 4.4: Model parameters for calibration

Model	**Input**	**Parameters**	**Experiments**
$\mathcal{G}_{\mathrm{C}}^{(\mathrm{f})}$	$f_C, \varphi = 0°$	$\alpha_{\mathrm{C}}^{(\mathrm{f})},\ \beta_{\mathrm{C}}^{(\mathrm{f})}$	Uniaxial compression: $[0°]_{8s}$
$\mathcal{G}_{\mathrm{T}}^{(\mathrm{f})}$	$f_T, \varphi = 0°$	$\alpha_{\mathrm{T}}^{(\mathrm{f})},\ \beta_{\mathrm{T}}^{(\mathrm{f})}$	Uniaxial tension: $[0°]_{4s}$
$\mathcal{G}_{\mathrm{C}}^{(\mathrm{m})}$	$f_C, \varphi = 90°$	$\alpha_{\mathrm{C}}^{(\mathrm{m})},\ \beta_{\mathrm{C}}^{(\mathrm{m})}$	Uniaxial compression: $[90°]_{12s}$
$\mathcal{G}_{\mathrm{T}}^{(\mathrm{m})}$	$f_T, \varphi = 90°$	$\alpha_{\mathrm{T}}^{(\mathrm{m})},\ \beta_{\mathrm{T}}^{(\mathrm{m})}$	Three point bending: $[90°]_{8s}$
$\mathcal{G}_{\mathrm{S}}^{(\mathrm{m})}$	$f_T, \varphi = \pm 45°$	$\alpha_{\mathrm{S}}^{(\mathrm{m})},\ \tau_{\mathrm{parm}}^{(\mathrm{m})}$	Uniaxial tension loading: $[\pm 45°]_{4s}$

Constructing surrogate models for composite laminate analysis is not straightforward since the constitutive model parameters have a range, beyond which the numerical solution is not possible. Hence, at first numerically feasible ranges of constituent model parameters are evaluated. Each mechanics model is ran for the corresponding range of model parameters. The range of model parameters considered in this study is given in Table 4.5. The response of the predicted laminate ultimate strengths are plotted with respect to the model parameters.

Table 4.5: Range of model parameters

Model	**Range of α**	**Rage of β**	**Range of τ_{parm}**
$\mathcal{G}_{\mathrm{C}}^{(\mathrm{f})}$	1.50 – 2.10	1.50 – 2.50	–
$\mathcal{G}_{\mathrm{T}}^{(\mathrm{f})}$	0.50 – 0.75	3.50 – 4.50	–
$\mathcal{G}_{\mathrm{C}}^{(\mathrm{m})}$	1.45 – 2.00	5.00 – 5.85	–
$\mathcal{G}_{\mathrm{T}}^{(\mathrm{m})}$	1.50 – 2.50	2.00 – 4.00	–
$\mathcal{G}_{\mathrm{S}}^{(\mathrm{m})}$	0.30 – 0.38	–	84 – 94

Response surface, Polynomial chaos expansion, Gaussian process models, radial basis functions, support vector machine, neural networks, etc. are some of the popular surrogate models. In this work, response surface based regression type surrogate model is used. For each mechanics model, the extremum values of model parameters (α and β) are discretized with 10 point having 9 equal intervals. The combination of the model parameters are used to run the mechanics model and predict the ultimate strength. Based on each set of model parameters the response surface of the model prediction is constructed. The response surface for ultimate strength of fiber constituent under tension and compression are shown in Figure 4.2.

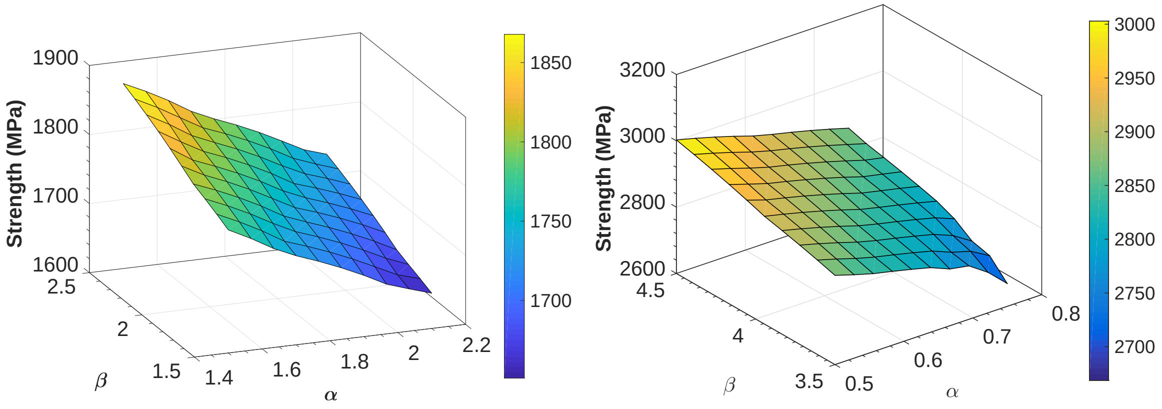

(a) Model: $\mathcal{G}_{\mathrm{C}}^{(\mathrm{f})}$ (b) Model: $\mathcal{G}_{\mathrm{T}}^{(\mathrm{f})}$

Figure 4.2: Response surface of ultimate strength of fiber dominated laminate failure

Similarly, the polymer matrix dominated laminate failure response surface are shown in Figure 4.3. In case of pure shear loading there are three mechanistic prediction points which do not lie on the flat response surface.

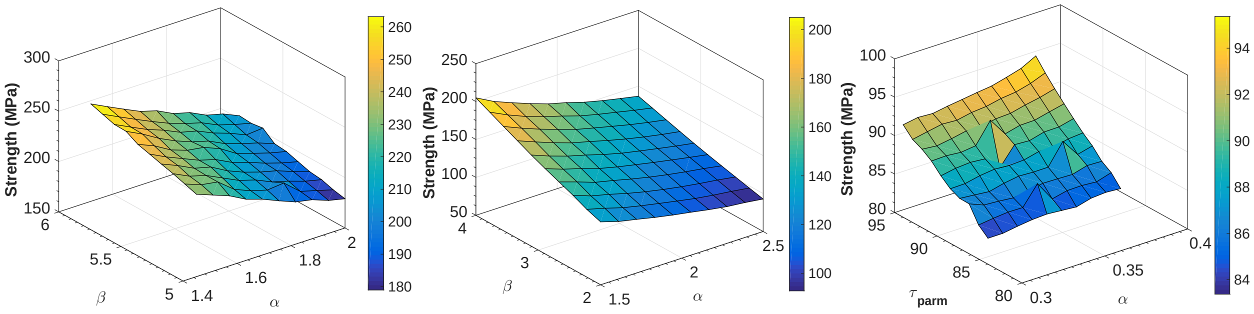

(a) Model: $\mathcal{G}_{\mathrm{C}}^{(\mathrm{m})}$ (b) Model: $\mathcal{G}_{\mathrm{T}}^{(\mathrm{m})}$ (c) Model: $\mathcal{G}_{\mathrm{S}}^{(\mathrm{m})}$

Figure 4.3: Response surface of ultimate strength of matrix dominated laminate failure

As the response surfaces of the ultimate strength output primarily show a flat surface, the regression model is developed as a linear combination of the two model parameters with a constant term. The mathematical expressions for models $\mathcal{G}_{\mathrm{C}}^{(\mathrm{f})}$, $\mathcal{G}_{\mathrm{T}}^{(\mathrm{f})}$, $\mathcal{G}_{\mathrm{C}}^{(\mathrm{m})}$, $\mathcal{G}_{\mathrm{T}}^{(\mathrm{m})}$ are shown in Equation (4.3). The model, $\mathcal{G}_{\mathrm{S}}^{(\mathrm{m})}$, considering shear loading aspect is represented in Equation (4.4). The simulation data are used to train each surrogate model.

$$Y_{\mathrm{model}} = b_0 + b_1\alpha + b_2\beta \tag{4.3}$$

$$Y_{\text{model}} = b_0 + b_1\alpha + b_2\ \tau_{\text{parm}} \tag{4.4}$$

Finally, values of the regression model coefficients and coefficient of determination (R^2) are shown in Table 4.6. All these surrogate models are acceptable as the value of R^2 is greater than 0.95.

Table 4.6: Coefficients of surrogate models

Model	b_0	b_1	b_2	R^2
$\mathcal{G}_{\text{C}}^{(\text{f})}$	1979.343	-221.123	86.0415	0.9973
$\mathcal{G}_{\text{T}}^{(\text{f})}$	2670.5	-576.677	138.65	0.9875
$\mathcal{G}_{\text{C}}^{(\text{m})}$	217.5355	-102.2869	32.5543	0.9909
$\mathcal{G}_{\text{T}}^{(\text{m})}$	158.588	-53.6932	27.9172	0.9987
$\mathcal{G}_{\text{S}}^{(\text{m})}$	0.0478	21.0565	0.9135	0.9649

Prior to applying the surrogate models, a global sensitivity analysis of the model parameters are performed. The results showing total sensitivity of the model parameters are shown in Figure 4.4.

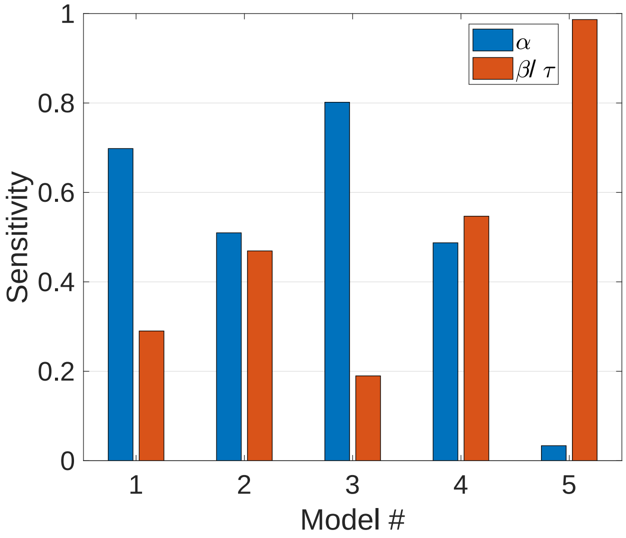

Figure 4.4: Global sensitivity analysis for surrogate model parameters

4.3 Model calibration

Once the surrogate model construction is complete, the model is ready for calibration. For this purpose, Equation (4.3) is substituted in Equations (4.1) and (4.2) to get the final expression for the calibration as in Equation (4.5):

$$\hat{Y}_{\text{obs}} = \begin{cases} \big(b_0 + b_1\alpha + b_2\beta\big) + \varepsilon_{\text{obs}} + \delta & \text{for } \mathcal{G}_{\text{C}}^{(\text{f})}, \mathcal{G}_{\text{T}}^{(\text{f})}, \mathcal{G}_{\text{C}}^{(\text{m})}, \mathcal{G}_{\text{T}}^{(\text{m})} \\ \\ \big(b_0 + b_1\alpha + b_2\ \tau_{\text{parm}}\big) + \varepsilon_{\text{obs}} + \delta & \text{for } \mathcal{G}_{\text{S}}^{(\text{m})} \end{cases} \tag{4.5}$$

$b_0 + b_1\alpha + b_2\ \tau_{\text{parm}}$ where, $\hat{Y}_{\text{obs}}$ is the the random variable of observation obtained from the prediction model. Based on Equation (4.5), two model parameters, measurement error (σ_{obs}) and model discrepancy (δ) need to be calibrated. In the presence of experimentally observed data, the error (ε) between the each observation and observation random variable from the prediction model can be calculated. The range of the model discrepancy and the standard deviation for measurement error are given in Table 4.7.

Table 4.7: Range of uncertainty parameters

Model	**Range of σ_{obs}**	**Rage of δ**
$\mathcal{G}_{\text{C}}^{(\text{f})}$	80 – 100	-50 – 40
$\mathcal{G}_{\text{T}}^{(\text{f})}$	80 – 110	-50 – 40
$\mathcal{G}_{\text{C}}^{(\text{m})}$	8 – 16	-15 – 20
$\mathcal{G}_{\text{T}}^{(\text{m})}$	5 – 10	-10 – 5
$\mathcal{G}_{\text{S}}^{(\text{m})}$	10 – 20	-25 – 20

To obtain the estimate of the 4 parameters a least square based approach is used and the sum of squares of the errors are minimized. Mathematically, the optimization problem is described as:

$$\varepsilon^{(i)} = \hat{Y}_{\text{obs}} - Y_{\text{obs}}^{(i)} \quad \text{where, } i = 1, 2, \cdots, p \tag{4.6}$$

$$\min \sum \left(\varepsilon^{(i)}\right)^2 \tag{4.7}$$

Due to presence of random measurement error in the prediction model, it is not possible to obtain unique combination of estimated parameters. Therefore, each model is run for 10,000 times to obtain the minimum value of the objective function. The estimated parameters for the surrogate model is given in Table 4.8.

Table 4.8: Estimate of model parameters

Model	α	β or τ	σ_{obs}	δ
$\mathcal{G}_{\text{C}}^{(\text{f})}$	1.8185	1.7513	88.9954	-4.7684
$\mathcal{G}_{\text{T}}^{(\text{f})}$	0.69008	4.1074	95.1039	-6.8263
$\mathcal{G}_{\text{C}}^{(\text{m})}$	1.4507	5.5591	12.4853	-5.3176
$\mathcal{G}_{\text{T}}^{(\text{m})}$	1.9689	3.0175	7.4399	-2.516
$\mathcal{G}_{\text{S}}^{(\text{m})}$	0.33994	88.9963	14.9787	-2.0014

These parameters are used in Chapter 6 to validate the prediction of the constitutive model.

CHAPTER 5

DEVELOPMENT OF MULTISCALE CRACK BAND MODEL

Mesh sensitivity issues can be resolved using approaches such as integral type non-local formulation [39], gradient type enhancement [40, 41] and crack band modeling [6]. Considering the computational needs in a structural scale simulation, the crack band model has been identified as an appropriate approach to be incorporated and implemented within the existing multiscale framework [8]. The mathematical formulation of the implementation of a multiscale crack band model is presented in Section 5.1.

5.1 Formulation of Multiscale Crack Band Model

The crack band model (CBM) needs to be incorporated in the current multiscale framework to facilitate the implementation of the weighted approach to model damage evolution in composites. The primary objective here is to ensure that the fracture energy is computed as a function of individual constituent deformation and that the failure process is consistent, regardless of macroscopic discretization. While the mesh bias issue (i.e., the propensity of the failure to follow the mesh lines) has been partially addressed by previous researchers using the CBM approach, but such efforts were focused solely on alleviating sensitivity to mesh size.

In the context of the current multiscale framework, there are three length scales to account for: (1) size of the microscopic crack band as defined by the width of the microstructural failure parts (w); (2) size of the unit cell (l); and (3) size of the macroscopic finite element (h). The fracture energy computed at the scale of the material microstructure can then be related to the macroscale mesh size parameter, h (as in the case of classical CBM) as well as w and l.

Let G_{f} be the fracture energy necessary to form all microcracks per unit (microscale) area within the composite material, so that

$$\widetilde{G}_{\mathrm{f}}(\epsilon_{\mathrm{f}}) = \int_0^{\epsilon_{\mathrm{f}}} \sigma_{\perp}^{(\xi)} : d\epsilon_{\perp}^{(\xi)} \tag{5.1}$$

in which, $\sigma_{\perp}^{(\xi)}$ and $\epsilon_{\perp}^{(\xi)}$ are the components of the part-averaged stress tensor (of part ξ) along a direction normal to the part, and ϵ_{f} denotes the ductility of the constituent. The total fracture energy per unit cell within the element is then $w\widetilde{G}_f$, where w is the width of a microstructural failure part. Employing the concept of periodicity, the total fracture energy within the coarse finite element can be related to the part fracture energy by:

$$G_{\mathrm{f}} = \frac{wh}{l}\widetilde{G}_{\mathrm{f}}\left(\epsilon_{\mathrm{f}}\right) \tag{5.2}$$

The fracture strain can then be expressed as a function of the unit cell fracture energy as:

$$\epsilon_{\mathrm{f}}(h) = \widetilde{G}_{\mathrm{f}}^{-1}\left(\frac{l}{wh}G_{\mathrm{f}}\right) \tag{5.3}$$

in which, $\tilde{G}_{\mathrm{f}}$ is taken to be a smooth and invertible function. Within the finite element discretization of the macroscopic structure, the value of the failure strain, ϵ_{f}, which is a parameter of the damage model, as explained below, is different and dictated by the size parameter of the element.

Analytical expressions for the fracture energy as well as the failure strain parameter are needed to efficiently implement the Multiscale Crack Band Model (MsCBM), such as

$$\left[\widetilde{G}_{\mathrm{f}}^{(1)} + \widetilde{G}_{\mathrm{f}}^{(2)}\left(\epsilon_{\mathrm{f}}\right)\right]\frac{wh}{l} = G_{\mathrm{f}} \tag{5.4}$$

where, $\widetilde{G}_{\mathrm{f}}^{(1)}$ and $\widetilde{G}_{\mathrm{f}}^{(2)}$ represent fracture energy in hardening and softening regimes, respectively, at the microscale, and under uniaxial loading. Considering the hardening part of the curve under uniaxial loading and the second condition on the right hand side of damage evolution Eq. 3.6, $\widetilde{G}_{\mathrm{f}}^{\mathrm{N}(1)}$ can be shown to take the following form:

$$\begin{aligned}\widetilde{G}_{\mathrm{f}}^{\mathrm{N}(1)} = \int_{0}^{\epsilon_{\mathrm{tr}}^{(\mathrm{N})}} \sigma d\epsilon = \frac{(1-d_{\mathrm{N}})E(\epsilon_{\mathrm{tr}}^{\mathrm{N}})^2}{2} + \hat{C}_{\mathrm{N}}\frac{\beta_{\mathrm{N}}\ln[(\hat{\alpha}_{\mathrm{N}}\epsilon_{\mathrm{tr}}^{\mathrm{N}} - \beta_{\mathrm{N}})^2+1] - \beta^{\mathrm{N}}\ln(1+(\beta_{\mathrm{N}})^2)}{2(\hat{\alpha}_{\mathrm{N}})^2} + \\ \hat{C}_{\mathrm{N}}\frac{[(\hat{\alpha}_{\mathrm{N}}\epsilon_{\mathrm{tr}}^{\mathrm{N}})^2 + (\beta_{\mathrm{N}})^2 + 1]\mathrm{atan}(\beta_{\mathrm{N}} - \hat{\alpha}_{\mathrm{N}}\epsilon_{\mathrm{tr}}) - [1-(\beta_{\mathrm{N}})^2]\mathrm{atan}(\beta_{\mathrm{N}})}{2(\hat{\alpha}_{\mathrm{N}})^2} + \hat{C}_{\mathrm{N}}\frac{\epsilon_{\mathrm{tr}}^{\mathrm{N}}}{2\hat{\alpha}_{\mathrm{N}}}\end{aligned} \tag{5.5}$$

where,

$$\hat{\alpha}_{\mathrm{N}} = \alpha_{\mathrm{N}}\chi_{\mathrm{N}}, \quad \hat{C}_{\mathrm{N}} = \frac{E}{\dfrac{\pi}{2} + \mathrm{atan}(\beta_{\mathrm{N}})}, \quad d_{\mathrm{N}} = \frac{\mathrm{atan}(\beta_{\mathrm{N}})}{\dfrac{\pi}{2} + \mathrm{atan}(\beta_{\mathrm{N}})} \tag{5.6}$$

Here, the superscript N represents normal loading. The analytical expression for the second part of the fracture energy using the third condition on the right hand side of damage evolution Eq. 3.6 is:

$$\widetilde{G}_{\mathrm{f}}^{\mathrm{N}(2)} = \int_{\epsilon_{\mathrm{tr}}^{\mathrm{N}}}^{\epsilon_{\mathrm{f}}^{\mathrm{N}}} \sigma d\epsilon = -E\left[A_{\mathrm{f}}^{\mathrm{N}}\frac{(\epsilon_{\mathrm{f}}^{\mathrm{N}})^2-(\epsilon_{\mathrm{tr}}^{\mathrm{N}})^2}{2} + \left[\Phi(\upsilon_{\mathrm{tr}}^{\mathrm{N}}) - (1+A_{\mathrm{f}}^{\mathrm{N}})\right]\frac{\upsilon_{\mathrm{tr}}^{\mathrm{N}}}{\chi_{\mathrm{N}}}(\epsilon_{\mathrm{f}}^{\mathrm{N}}-\epsilon_{\mathrm{tr}}^{\mathrm{N}})\right] \tag{5.7}$$

Fracture energy for the first and second parts under pure shear loading can be obtained similarly. Finally, the dissipated energy adjusted constituent failure strain can be defined as:

$$\epsilon_{\mathrm{f}}^{\mathrm{N}} = \epsilon_{\mathrm{tr}}^{\mathrm{N}} + 2\frac{\frac{1}{\widetilde{c}_1}\left(\frac{h_0}{h}-1\right)\widetilde{G}_{\mathrm{f}}^{\mathrm{N}(1)} + \left[1+\frac{1}{\widetilde{c}_1}\left(\frac{h_0}{h}-1\right)\right]\widetilde{G}_{\mathrm{f}}^{\mathrm{N}(2)}}{\left[1-\Phi(\upsilon_{\mathrm{tr}}^{\mathrm{N}})\right]E\epsilon_{\mathrm{tr}}^{\mathrm{N}}} \tag{5.8}$$

$$\epsilon_{\mathrm{f}}^{\mathrm{S}} = \epsilon_{\mathrm{tr}}^{\mathrm{S}} + 2(1+\nu)\frac{\frac{1}{\widetilde{c}_2}\left(\frac{h_0}{h}-1\right)\widetilde{G}_{\mathrm{f}}^{\mathrm{S}(1)} + \left[1+\frac{1}{\widetilde{c}_2}\left(\frac{h_0}{h}-1\right)\right]\widetilde{G}_{\mathrm{f}}^{\mathrm{S}(2)}}{\left[1-\Phi(\upsilon_{\mathrm{tr}}^{\mathrm{S}})\right]E\epsilon_{\mathrm{tr}}^{\mathrm{S}}} \tag{5.9}$$

where, $\widetilde{c}_1$ and $\widetilde{c}_2$ are the fracture energy scaling parameters. The reference and arbitrary mesh sizes are denoted by h_0 and h, respectively. The derivation of the multiscale crack band model expression is given in Appendix E.

Here, it is worth noting that the proposed crack band model regularization scheme can be extended to any microstructure morphology. The present study focuses on a square unit cell geometry with single fiber. In the case of a unit cell containing multiple fibers, all the 'damage parts' need to be identified first. Based on the morphology of newly identified 'damage parts', the development of a new reduced order model geometry will be necessary. The coefficient tensors for the new reduced order geometry can then be applied.

5.2 Computation of Dissipated Energy for Reduced Order Model

The performance of the multiscale crack band approach can be considered in the context of two macroscopic properties: (1) the overall strength of a macroscopic specimen, and (2) the amount of energy dissipated during the damage process. Given the macroscopic stress states from S-ERHM, the assessment of the energy dissipation characteristics requires

i. derivation of the dissipation energy density equation directly from the S-ERHM systems,

ii. implementation of the dissipation energy computation in the existing S-ERHM software, and

iii. verification of the S-ERHM computations under simplified conditions.

For brevity, only the thermodynamic treatment of isotropic damage is given here. Based on the strain-based continuum damage theory, the Helmholtz's free energy density is expressed as Eq. 5.10.

$$\boldsymbol{\Psi}(\boldsymbol{\epsilon},\omega)=(1-\omega)\boldsymbol{\Psi}_e(\boldsymbol{\epsilon}) \tag{5.10}$$

For small deformations, elastic free energy density is given by $\boldsymbol{\Psi}_e(\boldsymbol{\epsilon})=\dfrac{1}{2}\boldsymbol{\epsilon}:\mathbf{C}:\boldsymbol{\epsilon}$. The constitutive equation and thermodynamics force (i.e. damage energy release rate) are given as Eqs. 5.11 and 5.12, respectively.

$$\boldsymbol{\sigma}=\frac{\partial\boldsymbol{\Psi}(\boldsymbol{\epsilon},\omega)}{\partial\boldsymbol{\epsilon}}=(1-\omega)\mathbf{C}:\boldsymbol{\epsilon} \tag{5.11}$$

$$\mathcal{Y}=-\frac{\partial\boldsymbol{\Psi}(\boldsymbol{\epsilon},\omega)}{\partial\omega}=-\boldsymbol{\Psi}_e(\boldsymbol{\epsilon}) \tag{5.12}$$

In order for the macroscale variables, stress ($\overline{\boldsymbol{\sigma}}$) and strain ($\overline{\boldsymbol{\epsilon}}$), to be admissible in the macroscale constitutive relation, the Hill-Mandel lemma for macrohomogeneity condition must be satisfied:

$$\overline{\boldsymbol{\sigma}}:\dot{\overline{\boldsymbol{\epsilon}}}=\frac{1}{|\Theta|}\int_{\Theta}\boldsymbol{\sigma}:\dot{\boldsymbol{\epsilon}}\;d\theta \tag{5.13}$$

where, $\boldsymbol{\sigma}$ and $\boldsymbol{\epsilon}$ on the right hand side represent the microscale field variables for stress and strain, respectively. The left hand term corresponds to strain energy density rate which is equal to macroscopic internal power density in the absence of temperature change, signifying an open system. Using the Truesdell-Noll inequality, the inner product $\overline{\boldsymbol{\sigma}}:\dot{\overline{\boldsymbol{\epsilon}}}$ can be decomposed into elastic and damage induced inelastic parts; the latter of which is dissipated as heat. Applying the decomposition principle and Truesdell-Noll inequality, the macroscopic dissipation can be expressed as:

$$\dot{\overline{\Phi}}=\frac{1}{|\Theta|}\int_{\Theta}\mathcal{Y}\;\dot{\omega}\;d\theta \tag{5.14}$$

The discretization for damage field, ω and damage induced inelastic field, $\boldsymbol{\mu}$ for the existing reduced order model are given by Eqs. 2.9 and 2.10. In the incremental form of Eq.5.14, these equations can be expressed as:

$$\Delta\overline{\Phi}=\frac{1}{|\Theta|}\int_{\Theta}\mathcal{Y}\;\Delta\omega\;d\theta=\sum_{\gamma=1}^{n}\frac{1}{|\Theta|}\int_{\Theta^{(\xi)}}\mathcal{Y}\;d\theta\;\Delta\omega \tag{5.15}$$

$$\Delta\omega=\sum_{\gamma=1}^{n}N^{(\xi)}(\mathbf{y})\Delta\omega^{(\xi)} \tag{5.16}$$

where, $\Delta\omega^{(\xi)} = \omega_{n+1}^{(\xi)} - \omega_{n}^{(\xi)}$.

Finally, the incremental dissipated energy within the reduced order model becomes:

$$
\begin{aligned}
\Delta\overline{\Phi} = \frac{1}{2}\Bigg(\sum_{\gamma=1}^{n} \bar{\boldsymbol{\epsilon}} : \widehat{\mathbf{C}}^{(\xi)} : \bar{\boldsymbol{\epsilon}}\ \Delta\omega^{(\xi)} \ + \ \sum_{\xi=1}^{n}\sum_{\gamma=1}^{n} \bar{\boldsymbol{\epsilon}} : \widehat{\mathbf{B}}^{(\xi\gamma)} : \boldsymbol{\mu}^{(\xi)}\ \Delta\omega^{(\xi)} \\
+ \ \sum_{\gamma=1}^{n}\sum_{\xi=1}^{n}\sum_{\delta=1}^{n} \boldsymbol{\mu}^{(\xi)} : \widehat{\mathbf{F}}^{(\xi\gamma\delta)} : \boldsymbol{\mu}^{(\delta)}\ \Delta\omega^{(\xi)} \Bigg)
\end{aligned}
\tag{5.17}
$$

where,

$$
\widehat{\mathbf{C}}^{(\xi)} = \frac{1}{|\Theta|} \int_{\Theta^{(\xi)}} \mathbf{A}^{(\xi)}(\mathbf{y}) : \mathbf{C}^{(\xi)}(\mathbf{y}) : \mathbf{A}^{(\xi)}(\mathbf{y})\ N^{(\xi)}\ d\mathbf{y} \tag{5.18}
$$

$$
\widehat{\mathbf{B}}^{(\xi\gamma)} = \frac{1}{|\Theta|}\Big(\mathbf{B}^{(\xi\gamma)} + (\mathbf{B}^{(\xi\gamma)})^{\intercal} \Big) \tag{5.19}
$$

$$
\widehat{\mathbf{F}}^{(\xi\gamma\delta)} = \frac{1}{|\Theta|}\mathbf{F}^{(\xi\gamma\delta)} \tag{5.20}
$$

5.3 Computational Algorithm and Implementation

The computational aspects of numerical implementation of the multiscale crack band model are presented in this section. The concept of 'characteristic length' and its computation is presented first. The implementation of characteristic length calculation for macroscale analysis of fiber composite lamina is also considered.

5.3.1 Characteristic Length Formulation

Characteristic length of an element is the projected length of an element onto the direction of a crack vector. This concept is useful for calculating the crack band width. Two major types of crack bandwidth formulations are possible: (1) those based on element area or volume [5, 73], and (2) those based on element projection [12]. Computation of characteristic length was first proposed by Oliver [59], and later by Govindjee *et al.* [33]. The difference between Oliver's and Govindjee's methods was tested by Slobbe [78, 77] on a (non-square) rectangular element with one integration point. The crack band widths were computed for crack angles varying over $0 \leq \varphi \leq \frac{\pi}{2}$. According to Oliver, the crack band width can be interpreted as the distance between the sides of the element in a direction normal to the crack; whereas, in Govindjee *et al.*the crack band width is interpreted as the distance between the two farthest corner nodes of an element measured in a direction normal to the crack. In this research, the method proposed by Govindjee *et al.*is adapted in the context of multiple microscale failure modes. The direction of a single failure path in the global coordinate system can be defined as:

$$\mathbf{n}_i(\mathbf{x}) = \mathbf{T}\ \hat{\mathbf{n}}_i(\hat{\mathbf{x}}) \tag{5.21}$$

where, $\mathbf{T}$ is the transformation matrix from local coordinate system ($\hat{\mathbf{x}}$) to global coordinate system ($\mathbf{x}$). The crack orientation for a 3-dimensional element is given by Eq. 5.22.

$$\hat{\mathbf{n}}(\mathbf{x}) = \begin{Bmatrix} \sin\ (\varphi)\ \sin\ (\psi) \\ \cos\ (\psi) \\ \cos\ (\varphi)\ \sin\ (\psi) \end{Bmatrix} \tag{5.22}$$

where, φ and ψ are the azimuthal and polar angles in the local coordinate system. The projection of the element onto the crack vector direction can then be obtained by Eq. 5.23.

$$\hat{p}_i = [(\mathbf{x}_i - \mathbf{x}_c) \cdot \mathbf{n}(\mathbf{x})] \tag{5.23}$$

where, $\mathbf{x}_i$ and $\mathbf{x}_c$ correspond to the corner nodal points and center point of the corresponding element, respectively. Based on the projected length value, a scaling is performed to yield an indicator function $\mathcal{I}$ as

$$\mathcal{I}_i = \frac{[(\mathbf{x}_i - \mathbf{x}_c) \cdot \mathbf{n}(\mathbf{x})] - \hat{p}_{\min}}{\hat{p}_{\max} - \hat{p}_{\min}} \tag{5.24}$$

Finally the characteristic length, h^*, is calculated using Eq. 5.25.

$$h^* = \left(\left[\sum_{i=1}^{n_{\text{node}}} \frac{\partial N_i(\mathbf{x})}{\partial \mathbf{x}} \mathcal{I}_i \right] \cdot \mathbf{n}(\mathbf{x}) \right)^{-1} \tag{5.25}$$

The steps for characteristic length computation are presented in Algorithm 1. The MATLAB implementation of this Algorithm 1 for single scale analysis is given in Appendix F. This algorithm was tested with multiple 3D solid elements of different sizes. Specific to this study, the transformation matrix appearing in Eq. 5.21 takes the following form:

$$\mathbf{T} = \begin{bmatrix} \cos(\varphi) & 0 & \sin(\varphi) \\ 0 & 1 & 0 \\ -\sin(\varphi) & 0 & \cos(\varphi) \end{bmatrix} \tag{5.26}$$

where, φ represents the rotation angle between local to global coordinate in the x_1x_3-plane. The schematic representation of characteristic length for a macroscale specimen is shown in

Algorithm 1 Computation of characteristic length

```
Require: $n_{\text{nodes}}$, $\mathbf{x}$, $\hat{\mathbf{n}}$, $\mathbf{T}$
Ensure: $h^*$
Evaluate center of element, $\mathbf{x}_{\text{c}}$
Compute the direction of crack in global coordinate: $\mathbf{n}(\mathbf{x}) = \mathbf{T}\ \hat{\mathbf{n}}(\hat{\mathbf{x}})$
for $i = 1 \cdots n_{\text{nodes}}$ do
    Compute projection on crack direction: $\hat{p}_i = [(\mathbf{x}_i - \mathbf{x}_{\text{c}}) \cdot \mathbf{n}(\mathbf{x})]$
    Compute indicator function, $\mathcal{I}$:
        $\mathcal{I}_i = \frac{[(\mathbf{x}_i - \mathbf{x}_c) \cdot \mathbf{n}(\mathbf{x})] - \hat{p}_{\text{min}}}{\hat{p}_{\text{max}} - \hat{p}_{\text{min}}}$
    Evaluate characteristic length for the crack path with vector $\mathbf{n}$:
        $h^* = \left( \left[ \sum_{i=1}^{n_{\text{node}}} \frac{\partial N_i(\mathbf{x})}{\partial \mathbf{x}} \mathcal{I}_i \right] \cdot \mathbf{n}(\mathbf{x}) \right)^{-1}$
end for
```

Fig. 5.1. The advantage of using this approach is that the failure paths of the reduced order model are always known a-priori. Therefore, crack vectors for the reduced order model in the local coordinate can be defined as:

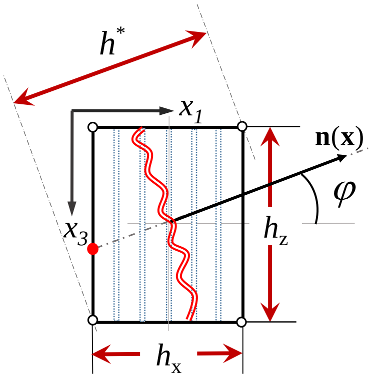

Figure 5.1: Characteristic length for a typical element

$$\hat{\mathbf{n}}_1(\hat{\mathbf{x}}) = \begin{Bmatrix} 0 \\ 0 \\ 1 \end{Bmatrix}; \quad \hat{\mathbf{n}}_2(\hat{\mathbf{x}}) = \begin{Bmatrix} 1 \\ 0 \\ 0 \end{Bmatrix}; \quad \hat{\mathbf{n}}_3(\hat{\mathbf{x}}) = \begin{Bmatrix} 0 \\ 1 \\ 0 \end{Bmatrix} \tag{5.27}$$

The variation of the macroscopic characteristic length with orientation angle φ for a failure path vector $\hat{\mathbf{n}}_2$ is shown in Fig. 5.2. It is clear from the computed characteristic lengths shown in the figure that if the crack lies in the x_1x_3-plane only, the characteristic length does not vary with thickness, which is measured in the x_2-Direction.

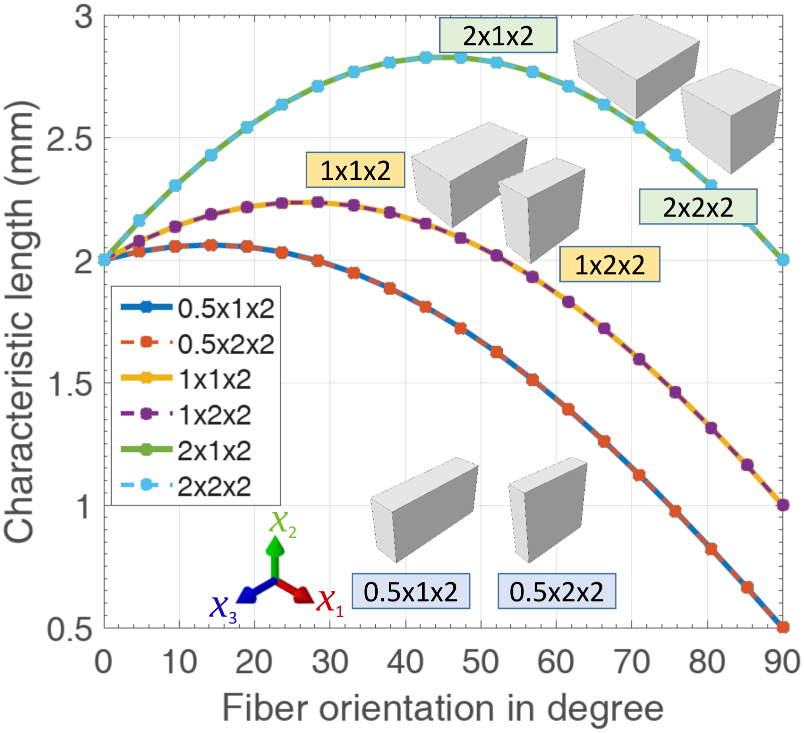

Figure 5.2: Fiber orientation angle vs. macroscale characteristic length plot

5.3.2 Characteristic Length Computation

In the case of multiple instances of a partition, the elements and nodes needed to be renumbered. To explain it further, an example problem is considered. In Fig. 5.3, a three part Abaqus model is created. Part-1 has only one instance namely Part-1-1. On the other hand, Parts 2 and 3 have two instances each, namely, Part-2-1, Part-2-2 and Part-3-1, Part-3-2. The meshing is done on each part, so that Part 1 contains 2 elements, Part 2 contains 4 elements and Part 3 contains 320 elements. Table 5.1 describes how does the geometry information (e.g. node and element numbers) for a user-defined function differs from standard Abaqus input file.

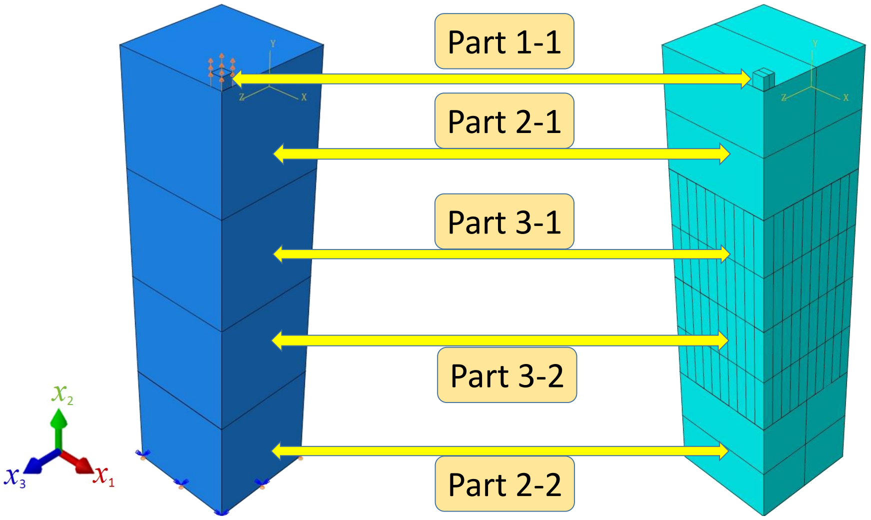

Figure 5.3: Abaqus model with multiple parts no discretization (left), with discretization (right)

Table 5.1: Geometric information of the model

Instance	Angle	Abaqus input file		For user-defined subroutine		New sequence
		Node no.#	Element no.#	Node no.#	Element no.#	
Part-1-1	30°	$1, \cdots, 12$	$1, 2$	$1, \cdots, 12$	$1, 2$	1
Part-2-1	0°	$1, \cdots, 18$	$1, 2, 3, 4$	$13, \cdots, 30$	$3, 4, 5, 6$	2
Part-3-1	45°	$1, \cdots, 543$	$1, \cdots, 320$	$49, \cdots, 591$	$11, \cdots, 330$	4
Part-3-2	45°	$1, \cdots, 543$	$1, \cdots, 320$	$592, \cdots, 1134$	$331, \cdots, 650$	5
Part-2-2	0°	$1, \cdots, 18$	$1, 2, 3, 4$	$31, \cdots, 48$	$7, 8, 9, 10$	3

A Python wrapper, called `MeshInfo.py`, was used to parse the information from Abaqus input file, *e.g.* `jobname.inp`. The part geometry information like nodal coordinates, element connectivity table, and orientation were parsed from Abaqus input file. The renumbering scheme is presented as steps 6 to 16 in Algorithm 2. Once renumbering is complete, the element list is ready for characteristic length calculation using Algorithm 1. Characteristic length for all 3 failure paths are calculated for every element using the crack path vector. The outputs are stored as a list of element number and characteristic lengths in a file called `jobname_meshinfo.ic`.

Algorithm 2 Computing characteristic length for a multi-instance Abaqus model

```
Number of parts in model: $n_{\text{part}}$
Number of instances for each part: $n_{\text{instance}}$
Orientation for each instance : $\varphi$
Instance translation vector, $\widehat{\mathbf{V}}$
Start global numbering of elements and nodes for an instance
$n_{\text{prt}} \leftarrow 0$
for $i = 1 \cdots n_{\text{part}}$ do
    $n_{\text{inst}} \leftarrow 0$
    for $j = 1 \cdots n_{\text{instance}}$ do
        Update node numbers: $\left(1 + n_{\text{prt}} \times n_{\text{inst}} \times n^{(j)}\right) \cdots\cdots \left(n^{(j)} + n_{\text{prt}} \times n_{\text{inst}} \times n^{(j)}\right)$
        Update element numbers: $\left(1+n_{\text{prt}} \times n_{\text{inst}} \times m^{(j)}\right) \cdots\cdots \left(n^{(j)}+n_{\text{prt}} \times n_{\text{inst}} \times m^{(j)}\right)$

        Update nodal coordinates: $\mathbf{x} + \widehat{\mathbf{V}}$
        $n_{\text{inst}} = n_{\text{inst}} + j$
    end for
    $n_{\text{prt}} = n_{\text{prt}} + i$
end for
Total elements: $n^{\text{elm}}$
for all $i$ such that $i = 1 \cdots n^{\text{elm}}$ do
    for $j = 1 \cdots n_{\text{crack}}$ do
        Perform Algorithm 1
    end for
    Obtain characteristic length based on microscale failure path
end for
```

5.4 Macroscale Analysis

The coefficient tensors obtained from microscale analysis is used for micro-macro bridging of local effect within the material. These precomputed coefficient tensors along with damage model parameters are stored as an input companion file. The external database is read in Abaqus at the beginning of the analysis, using the User-defined EXTERNAL DataBase (UEXTERNALDB) subroutine. The characteristic lengths of elements are stored in a file `jobname_meshinfo.ic`. The microscale problem is solved at each quadrature point throughout the macroscale analysis using User-defined MATerial subroutine (UMAT). The damage model parameters are evaluated within UEXTERNALDB, at the beginning of the analysis. The reduced order model problem is solved at each integration point of the macroscale numerical specimen as shown in Figure 5.4.

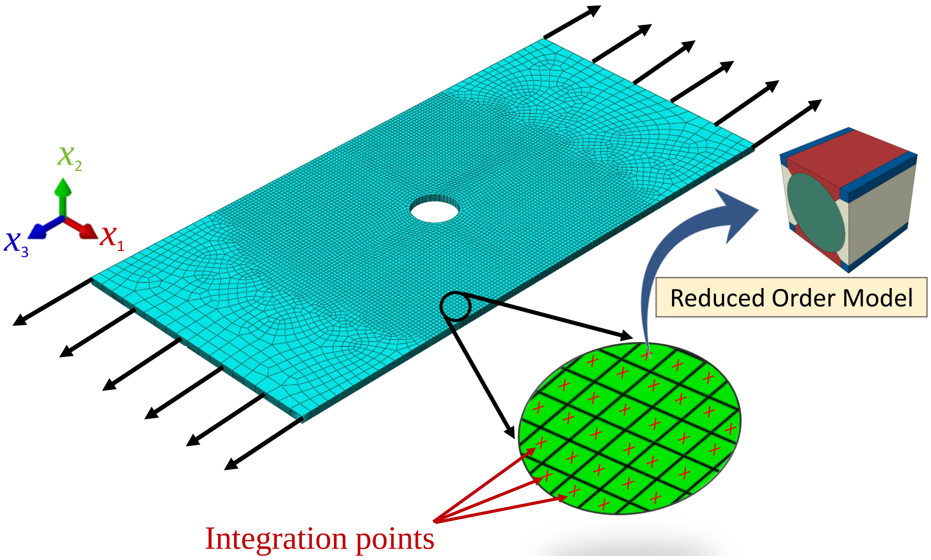

Figure 5.4: Macroscale analysis with reduced order model

The steps employed for macroscale analysis are presented below. Python script is utilized to post-process the information in the Abaqus output data files generated from the numerical simulation. The stress and strain information are extracted from this file to create the stress-strain plots. The steps followed in macroscale analysis are as below.

I) The numerical specimen configurations (i.e. layup, orientations, and mesh) are the inputs for macroscale finite element analysis using Abaqus.The constitutive model parameters for each element are evaluated corresponding to reference mesh size.

II) Displacement controlled loading applied to the numerical specimen is assumed to be monotonic. In the event of cyclic loading, the effects of load reversal will require appropriate modification of AHLS model.

III) The solution of the micro-problem is performed at each integration point of the macroscale finite element. The precomputed coefficient tensors expedited the macrostructural analysis, as on-the-fly evaluation of the microscale model could be undertaken for the reduced order model (with reduced number of parts), without fully resolved microstructure.

IV) At each increment, the triaxiality parameter, k_b, is evaluated for all three reduced order damaged parts, such as 'transverse matrix cracking', 'delamination', and 'fiber cracking'. Accordingly, appropriate damage model parameter is evaluated to capture the damage state, using Equations (3.15) to (3.17).

V) The shape parameters are weighted using Equations (3.10) and (3.11). Once the material starts to soften, damage evolution is governed by the parameters, υ_{tr} and A_{f}, only, as in Equation (3.6).

VI) Since damage is considered directly at the scale of the constituents, damaged parts are the consequence of the microscale response, which is explicitly evaluated within the multiscale model. The damage within each part of the reduced order model is computed using Eq. 5.17. For each increment, the computed dissipation energy density is evaluated at each integration point.

VII) Ensurance of convergence of the solution for the reduced order model problem for each macroscale finite element. The UMAT computes the homogenized secant stiffness tensor and stress components at each integration point based on the macroscale strains obtained by the finite element solver.

VIII) At each incremental step, for a macroscale element the damages and damage-induced strains within each reduced order part are passed on to Abaqus as state variables.

IX) Once the macroscale analysis is completed, Python script is used to post-process the information in the Abaqus output data (`.odb`) file generated from the numerical simulation. The element volume, $\mathcal{V}_i$, and the incremental dissipation energy density $\mathcal{E}_i(t)$-history of the i-th element are extracted using the Python script.

X) The total analytical dissipation energy history of the macroscale structure is computed as $\mathcal{DE}_{\mathrm{anl}}(t) = \sum_{i=1}^{n^{\mathrm{elm}}} \mathcal{E}_i(t)\mathcal{V}_i(t)$, where n^{elm} represents the number of elements.

Information on stresses and strains are extracted from the resulting file to create the stress-strain plots. In this study, eight-noded hexahedron (C3D8R) elements with reduced integration points were used for domain discretization. In the case of angle plies inside a laminate, the mesh was aligned in the direction of the fiber to avoid mesh bias in the solution. The computational scheme followed the flowchart shown in Fig. 5.5.

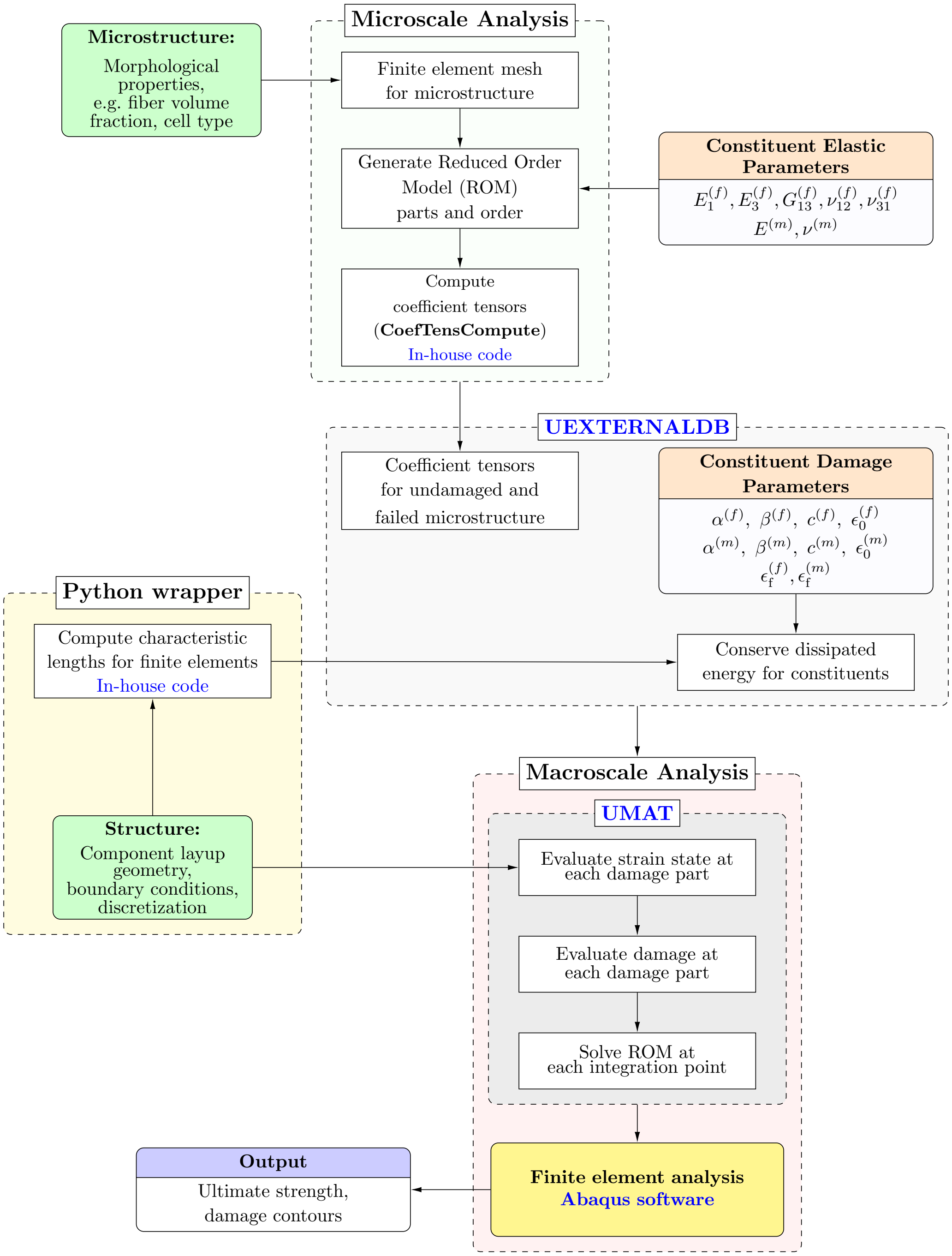

Figure 5.5: Computational implementation of the multiscale crack band model in S-ERHM framework

5.5 Numerical Verification of Multiscale Crack Band Model

In this section, verification of the proposed multiscale crack band model is presented using macroscale numerical specimens. The elastic material parameters used for polymer matrix and carbon fiber are shown in Tables 5.2 and 5.3, respectively. The calibration process of constitutive model parameters for polymer matrix and carbon fiber are discussed in Bhattacharyya and Basu [7].

Table 5.2: Polymer matrix elastic material parameters

Parameter	**Value**
Elastic modulus (in tension), $E^{(\mathrm{m})}$ (GPa)	3.98
Elastic modulus (in compression), $E^{(\mathrm{m})}$ (GPa)	3.69
Poisson's ratio, $\nu^{(\mathrm{m})}$	0.375

Table 5.3: Carbon fiber elastic material parameters

Parameter	**Value**
Longitudinal elastic modulus (in tension), $E_{33}^{(\mathrm{f})}$ (GPa)	252.00
Longitudinal elastic modulus (in compression), $E_{33}^{(\mathrm{f})}$ (GPa)	210.50
Transverse elastic modulus, $E_{11}^{(\mathrm{f})}$ (GPa)	12.45
Shear modulus, $G_{13}^{(\mathrm{f})}$ (GPa)	13.20
Longitudinal Poisson's ratio, $\nu_{12}^{(\mathrm{f})}$	0.291
Transverse Poisson's ratio, $\nu_{31}^{(\mathrm{f})}$	0.206

5.5.1 Verification of Multiscale Crack Band Model for Unit Cube

A mesh sensitivity study was performed on a uniformly loaded unidirectional composite cube of size 10 $mm \times 10$ $mm \times 10$ mm, subjected to a uniaxial loading, resembling mode-I loading. This loading caused failure of delamination damage part within the reduced order model. The macroscale numerical specimen was tested for 6 different discretizations. Within the macroscale unit cube domain, the number of elements was varied along the direction of loading using 1, 2, 3, 4, 6 and 8 elements. The numerical specimens discretized with one element and eight elements are shown in Fig. 5.6. The eight element case was considered as the reference case and all six cases were executed. It was found that as the number of elements in the model increased, the stress-strain behavior exhibited a steeper softening slope, as shown in Fig. 5.7a, and the models showed damage localization, which is an indication of mesh sensitivity. To study mesh objectivity, the multiscale crack band

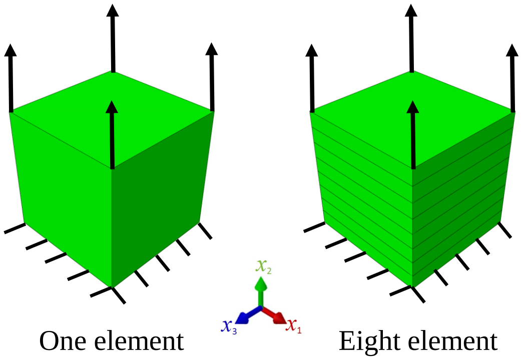

Figure 5.6: Abaqus models for testing mesh sensitivity

model (MsCBM) was applied to same six discretizations. The stress-strain results shown in Fig. 5.7b clearly indicate that the post-peak softening slope has been regularized. Thus, the MsCBM is successfully verified for the unit cube macroscopic model. The uniaxial loading energy scaling parameter $\tilde{c}$ for constituent fiber and matrix were calibrated as 2.75 and 1.052, respectively.

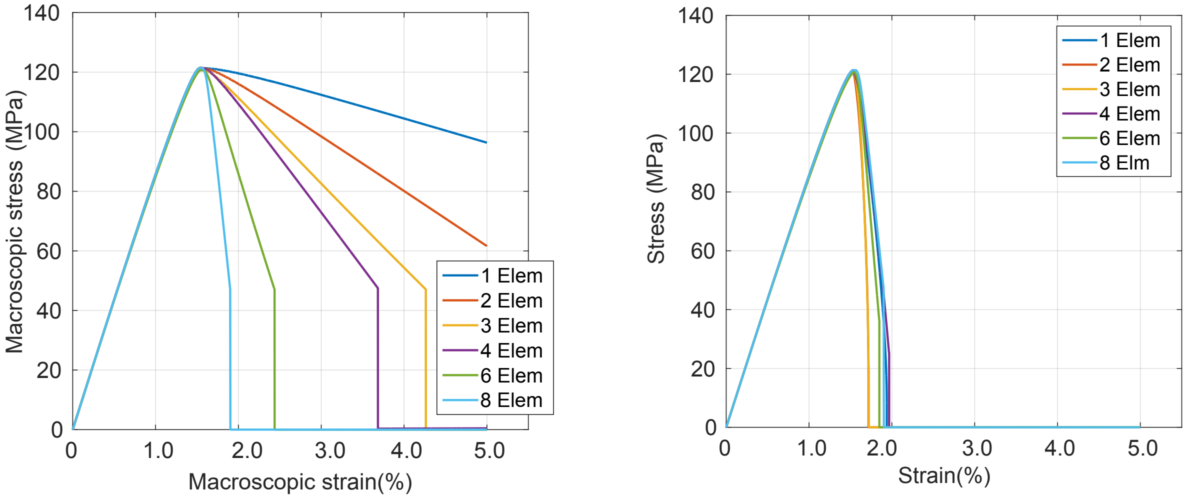

(a) without multiscale crack band model

(b) with multiscale crack band model

Figure 5.7: Six discretization of the unit cube macroscale numerical specimens

5.5.2 Verification of Multiscale Crack Band Model for Open-hole Ply

A second verification study was undertaken on more complex macroscale numerical models comprising of 90° and 0° open-hole ply specimens. The size of the numerical model is $80\ mm \times 38.1\ mm \times 0.125\ mm$ with a hole of diameter $6.35\ mm$. Appropriate boundary conditions were imposed to capture the failure of the open-hole specimen under tensile loading.

The primary purpose of using an open-hole specimen is to evaluate the method's ability to capture the damage caused by stress concentrations near the hole. In this case, the models were tested for 5 discretizations with element size varying from 0.80 mm to 0.30 mm. For computational efficiency, only one layer of element was stacked along through the thickness direction. The mesh was refined uniformly all over the specimen, as shown in Fig. 5.8.

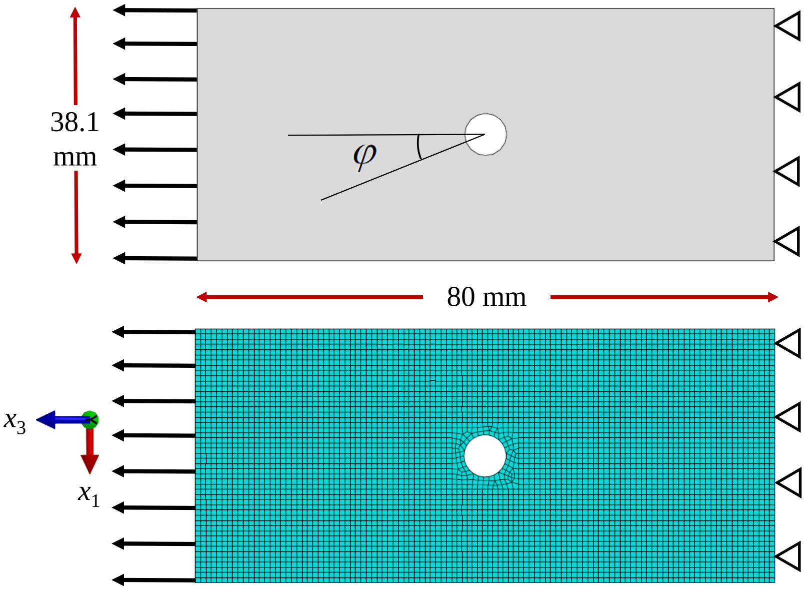

Figure 5.8: Abaqus model for open hole numerical specimen geometry and mesh

5.5.2.1 90° open-hole ply simulation

At first, a mesh-sensitivity study was undertaken on all five numerical specimens without using MsCBM. The specimen strength was found to degrade with increasing mesh refinement, signifying that the stress-concentration near the hole was being captured correctly by model refinement. The corresponding strain vs. stress plot results are shown in Fig. 5.9.

The energy for the reference mesh size is shown in solid black line. It is clear from Fig. 5.10a that wide variations of energy are observed without the MsCBM. On the other hand, MsCBM simulation results in Fig. 5.10b show that the dissipation energy values to coalesce with the reference mesh dissipation energy.

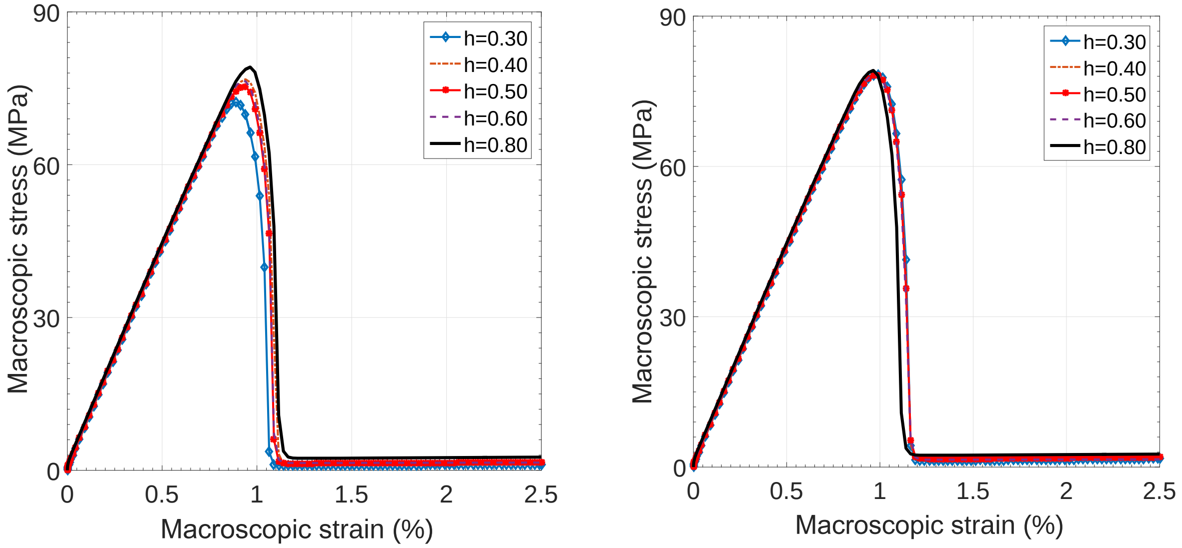

(a) no multiscale crack band model

(b) with multiscale crack band model

Figure 5.9: Strain vs. stress for 90° numerical specimens with and without MsCBM

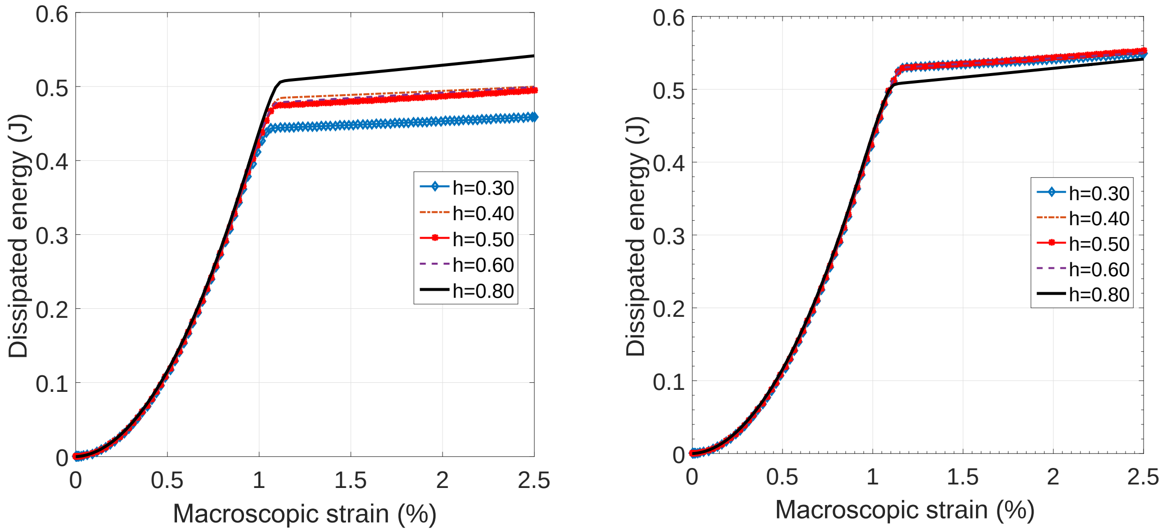

(a) Energy vs strain: no MsCBM

(b) Energy vs strain: with MsCBM

Figure 5.10: Comparative dissipated energy for 90° numerical specimens

By comparing the peak strengths of the specimens it has been confirmed that not only the strength of the specimens is regularized (Fig. 5.11a), but also the energy is conserved for different mesh sizes (Fig. 5.11b). The small discrepancies in the result can, possibly, be attributed to use of extremely small mesh size.

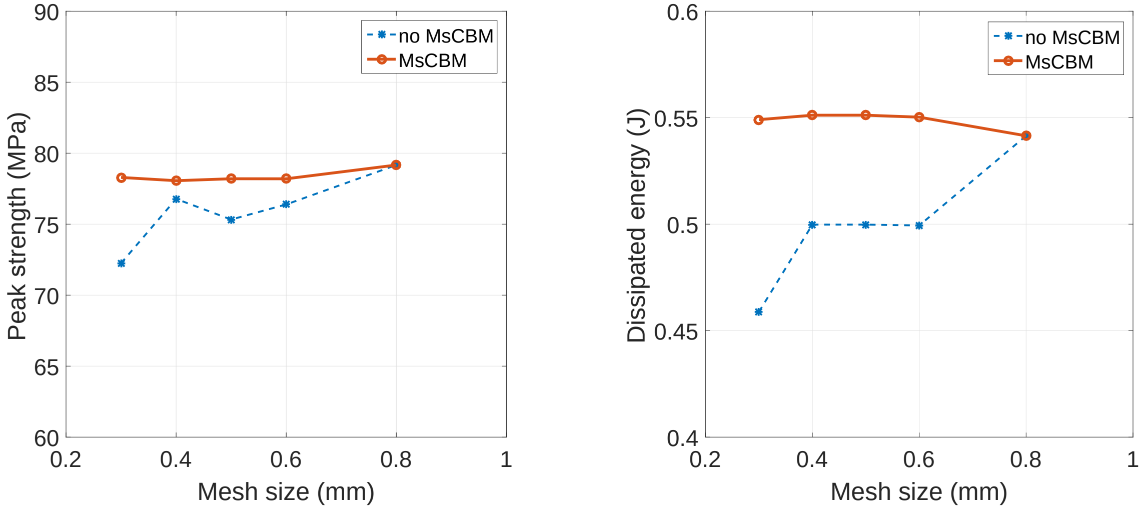

(a) Variation of peak force with mesh size (b) Variation of dissipated energy with mesh size

Figure 5.11: Results for 90° numerical specimens with and without MsCBM

All the 90° numerical models faithfully captured the progressive damage path within the specimen caused by stress concentration near the hole, followed by matrix cracking. No fiber damage was noticed in the simulation. Localized damage propagated along the width into the ligaments of the open hole specimens. The damage contours for different discretizations of the specimens are shown in Fig. 5.12. The reference mesh size is omitted in this figure

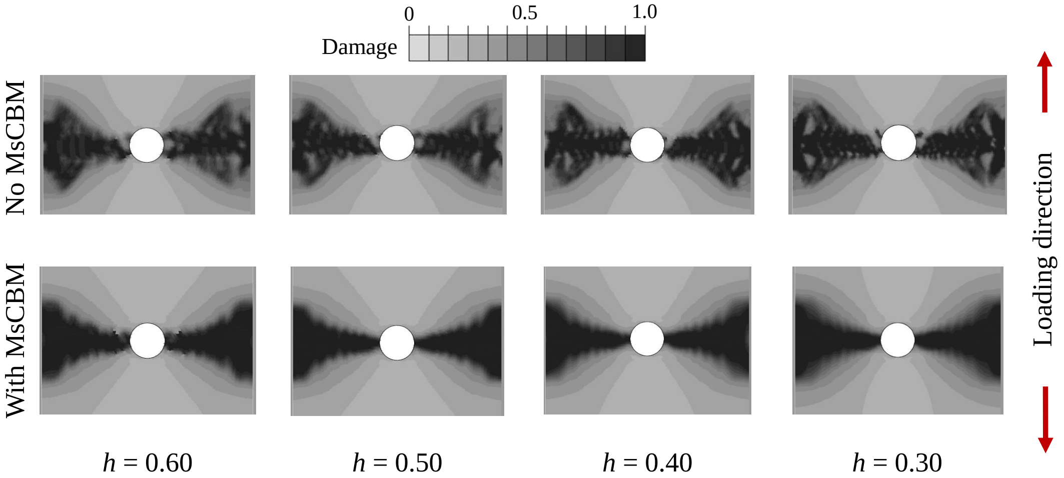

Figure 5.12: Matrix cracking damage of open hole 90° specimens

as no regularization is induced for the reference mesh size. Darker shades indicate more damage; whereas, the progressively lighter ones indicate lesser to no damage state. It is also observed that the specimens subjected to energy regularization show smoother failure pattern compared to the diffused damage pattern obtained with no regularization.

5.5.2.2 0° open-hole ply specimen

Following the 90° layup simulations, implementation of MsCBM was verified for 0° open-hole ply specimens. Similar to 90° ply, the mesh was refined uniformly all over the specimen domain. It was observed that without MsCBM the specimen strength reduced with refinement of discretization. However, with MsCBM the specimen strength remained within a reasonable bound (Fig. 5.13a). In terms of dissipated energy, the smallest mesh size has very high energy, as shown in Fig. 5.13b. This increase in the dissipated energy is contributed by the damage model used, which assumes no shear strength of the fiber constituent.

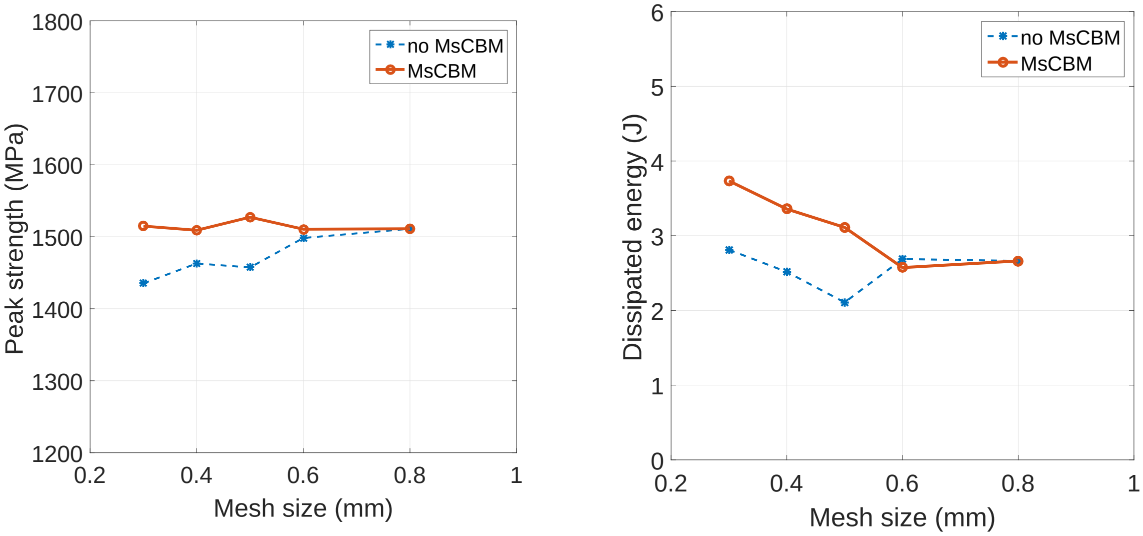

(a) Variation of peak force with mesh size

(b) Variation of dissipated energy with mesh size

Figure 5.13: Results for 0° numerical specimens with and without MsCBM

Unlike 90° open hole specimen, 0° one undergoes both fiber damage and matrix cracking near the hole. Also, matrix splitting was observed in the specimens. The fiber damage contours for different discretizations of the specimens are presented in Fig. 5.14. It is worth noting that in the case of simulations without regularization, the damage progression is not monotonic. On the other hand, the damage accumulation in energy regularized specimens show smoother progression of damage.

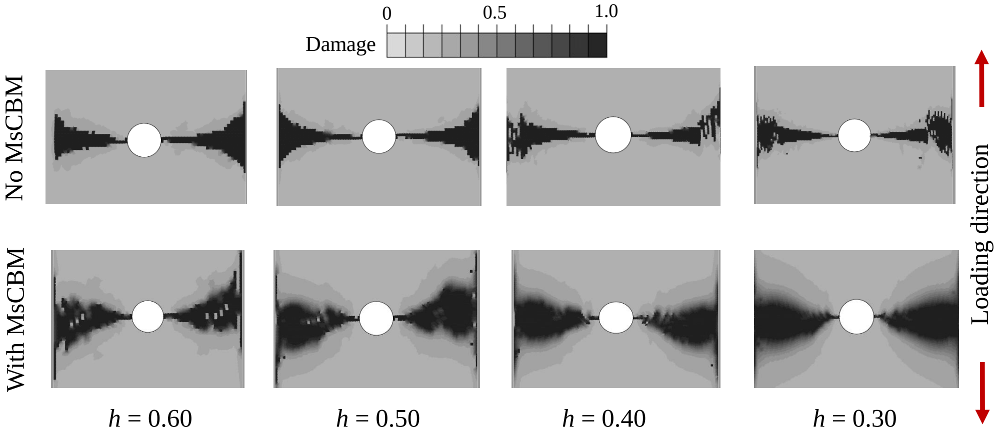

Figure 5.14: Fiber damage for open hole 0° specimens

5.5.3 Verification of Multiscale Crack Band Model for Laminates

Finally, the multiscale crack band model was evaluated for laminate level simulation. For this purpose, cross-ply laminate $[90^\circ_2/0^\circ_2]_s$ with open-hole geometry was chosen. This example demonstrated the performance of multiscale crack band model for a laminate with multiple plies and nonuniform mesh. Four different discretizations were considered. In this study, the mesh size, $h = 1.25$ mm was assumed as the reference mesh size. The refined mesh sizes

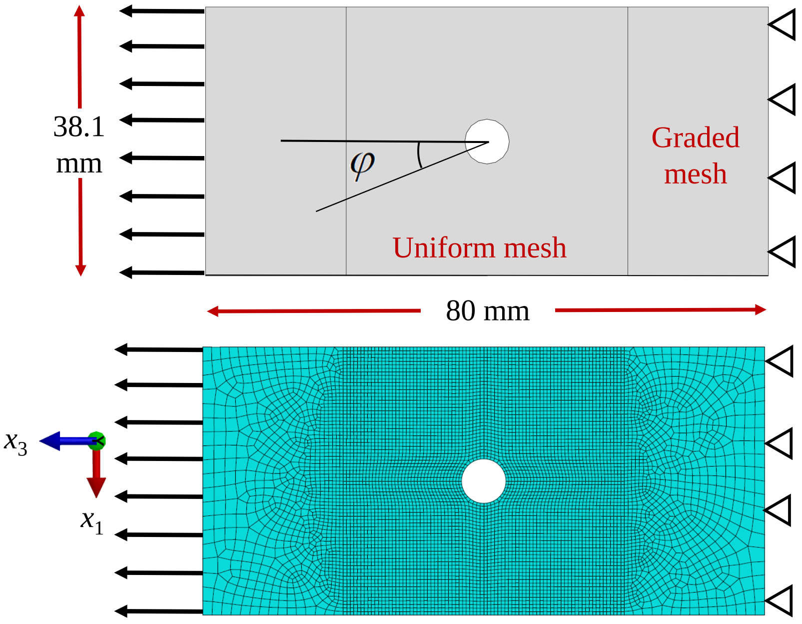

Figure 5.15: Abaqus model for cross-ply specimen geometry with non uniform mesh

considered were for $h = 1.00$ mm, $h = 0.75$ mm and $h = 0.50$ mm. In contrast with the study described in Section 5.5.2, the region of stress concentration only was discretized with refined mesh; whereas, the domain far from the open hole was discretized with transitional mesh. The geometry and meshing of the laminate are shown in Fig. 5.15.

In Fig. 5.16, the peak strength and dissipated energy is found to decrease with mesh refinement. The simulation results with multiscale crack band models demonstrated regularization of peak strength of the laminate. Only marginal increase in dissipated energy is observed for numerical specimens with MsCBM.

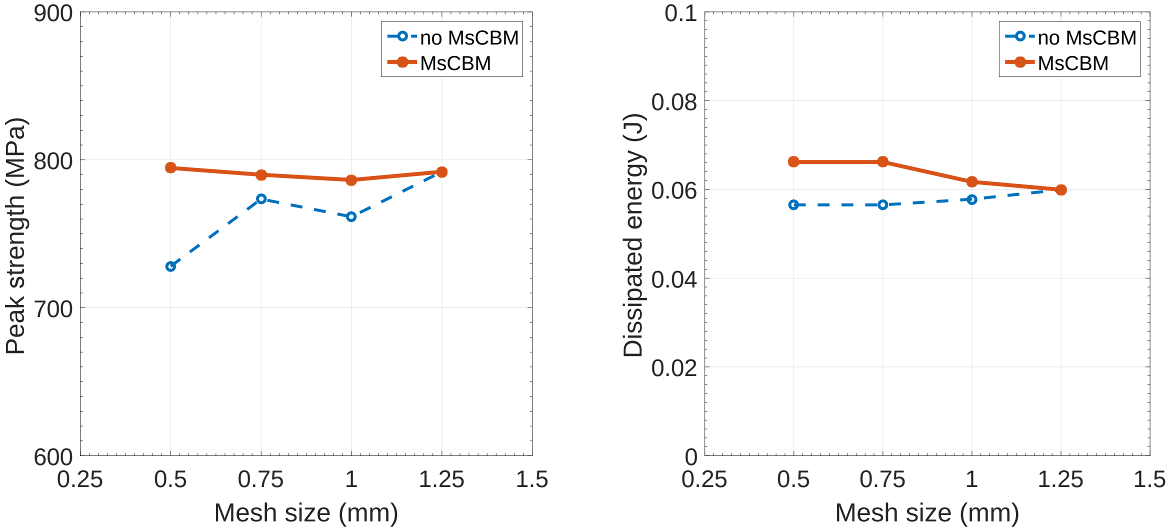

(a) Variation of peak force with mesh size (b) Variation of dissipated energy with mesh size

Figure 5.16: Results for cross-ply numerical specimens with and without MsCBM

The possible reason for increase in dissipated energy can be attributed to the increase in failure strain parameters of the fibers specific to 0° ply. Qualitatively the matrix damage appears to be very close to the results of CFRP cross-ply composites, as documented in O'Higgins [61].

5.5.3.1 Computing times comparison for open-hole plies and cross-ply laminates

To this end, the computing time is compared for the numerical specimens with HPC resources. The simulation of the numerical specimens was undertaken on the computer **MC-2**. Each simulation was performed on a single compute node using 8 cpus in a shared memory parallel configuration. Simulation run times are compared in Table 5.4.

Table 5.4: Comparison of computation times for open-hole plies and cross-ply specimens

Lay up orientation	Mesh size (mm)	Total elements	Wall time (hh:mm:ss)	
			no MsCBM	with MsCBM
90°	0.80	4788	00:09:22	00:09:24
	0.60	8404	00:14:27	00:16:14
	0.50	12100	00:30:18	00:22:03
	0.40	18831	00:48:57	00:31:13
	0.30	33456	01:20:17	00:50:34
0°	0.80	4788	00:09:14	00:07:11
	0.60	8404	00:13:28	00:14:32
	0.50	12100	00:18:41	00:19:51
	0.40	18831	00:27:39	00:29:55
	0.30	33456	00:46:12	00:49:01
$[90^\circ_2/0^\circ_2]_s$	1.25	7280	00:09:30	00:09:30
	1.00	10228	00:13:39	00:14:29
	0.75	23904	00:49:46	00:49:13
	0.50	47522	01:51:39	01:35:27

CHAPTER 6

VALIDATION OF PROGRESSIVE DAMAGE MODEL

The unnotched specimens used for validation had a width of 25.4 mm. The length of specimen in tension was 250 mm and in compression it was 140 mm. The thickness of each ply for validation layup was 0.127 mm. In the case of open-hole specimens, the diameter of the central hole was 6.35 mm. The stress in the laminate is computed for the numerical specimens as the sum of the reactive forces at the pinned end of the specimen divided by the gross cross-sectional area of the specimen. The strain computations closely followed the method the strains were measured in the experiments using extensometers in the case of open-hole specimens and strain-gages for unnotched specimens. For instance, two nodes in the mesh for the outer ply in each numerical specimen were identified corresponding to the gage points of the extensometer. Then the computed strain is obtained as the change in the distance between these two nodes divided by gage length.

6.1 Numerical Specimens in Tension

In this case, all the laminates are subjected to uniaxial tensile loading along the longitudinal direction. It is apparent that the constitutive model predicts the initial stiffness quite accurately. The results for $[0, 45, 90, -45]_{2s}$, $[60, 0, -60]_{3s}$ and $[30, 60, 90, -60, -30]_{2s}$ under uniaxial tension are presented in Figures 6.1, 6.3 and 6.5. In the case of $[0, 45, 90, -45]_{2s}$ unnotched and open-hole numerical specimens, the predicted stiffness is exactly same as observed in experiments. A small variation is noted in the ultimate strength prediction for open-hole specimen shown in Figure 6.1a. However, the constitutive model is able to capture the nonlinearity observed near peak.

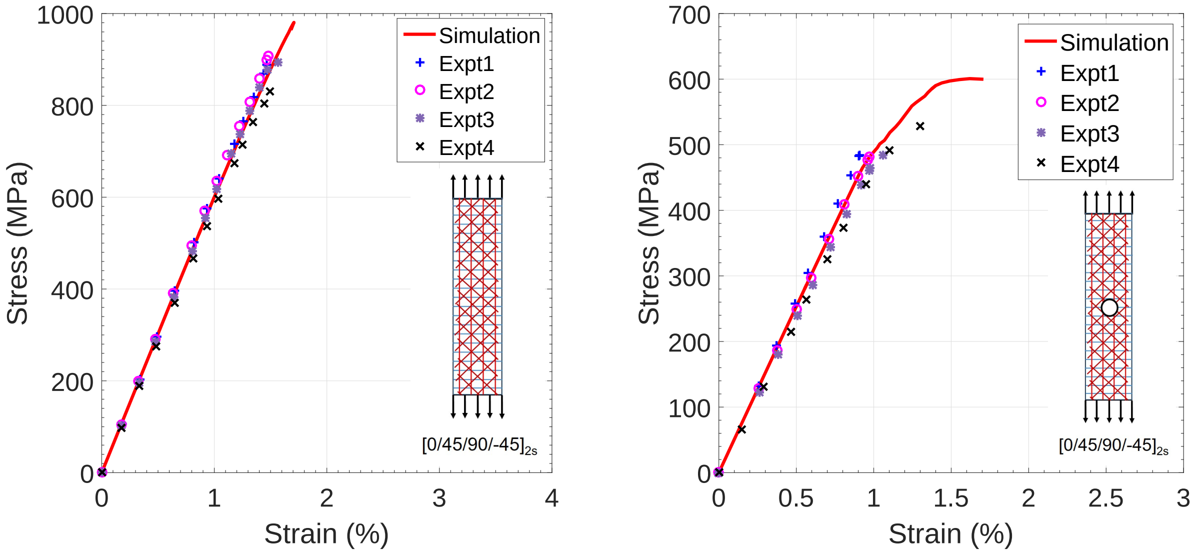

(a) Unnotched specimens (b) Open hole specimen

Figure 6.1: Stress vs. strain for $[0, 45, 90, -45]_{2s}$ quasi-isotropic specimens under tension

Gray scale damage contours of the $[0, 45, 90, -45]_{2s}$ quasi-isotropic open-hole specimen for the layups up to the plane of symmetry are shown in Figure 6.2. The darker shades indicate higher damage whereas the lighter ones indicate low to no damage state. The damage in the 0° plies are contributed by fiber damage, matrix cracking and delamination. On the other hand, 90° and 45° plies observed significant matrix-cracking near the hole.

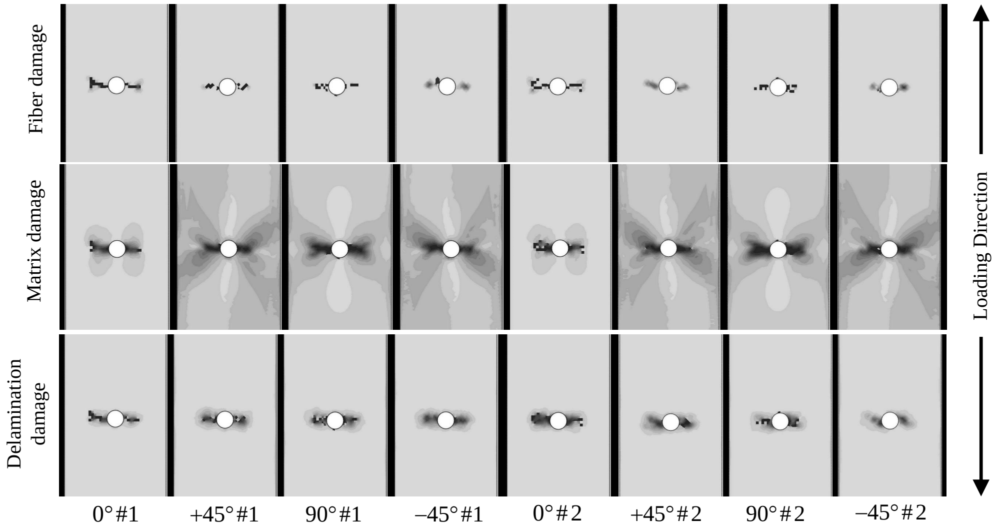

Figure 6.2: Damage contour for $[0, 45, 90, -45]_{2s}$ quasi-isotropic specimen under tension

In the case of $[60, 0, -60]_{3s}$ unnotched and open-hole numerical specimens, the stiffness and ultimate strength predictions are quite accurate. Also, the constitutive model is able to capture the expected nonlinearity near the ultimate strength.

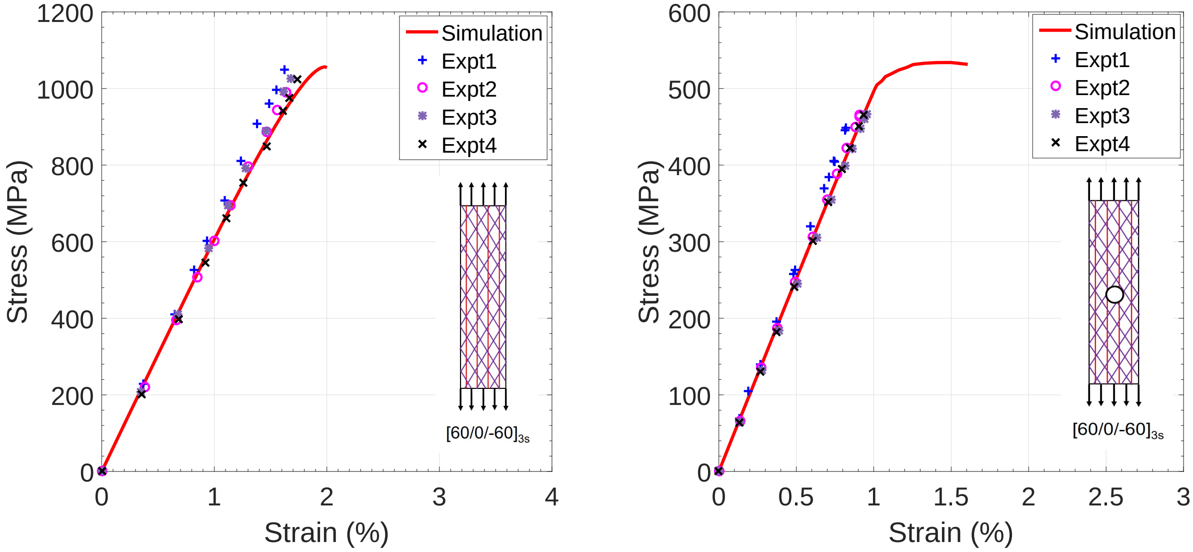

(a) Unnotched specimen (b) Open hole specimen

Figure 6.3: Stress vs. strain for $[60, 0, -60]_{3s}$ specimens under tension

The damage contour for the $[60, 0, -60]_{3s}$ open-hole laminate specimen is shown in Figure 6.4. The 0° plies demonstrated fiber damage, matrix cracking and delamination. In the 60° plies fiber splitting and very small delamination are observed. The −60° ply matrix-cracking is predominant in other failure modes.

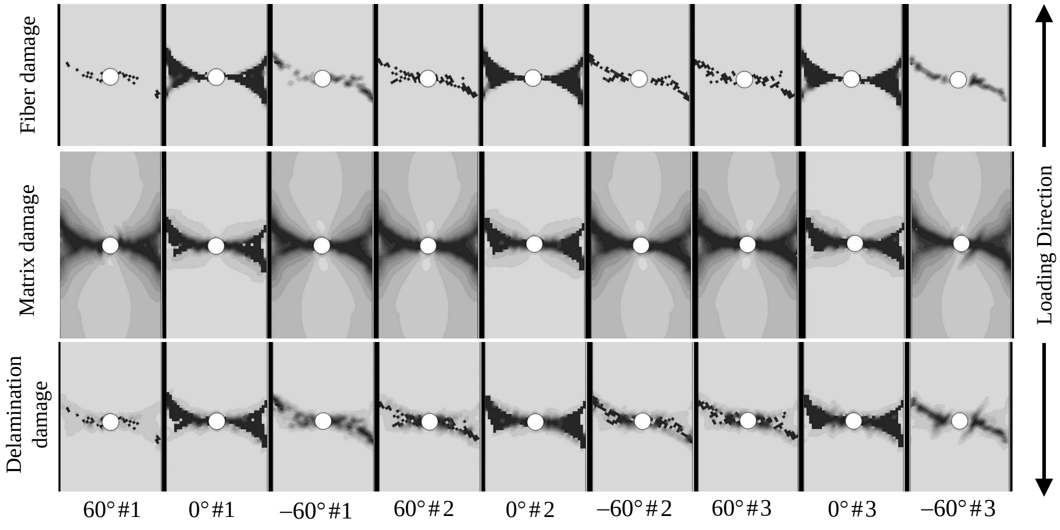

Figure 6.4: Damage contour for $[60, 0, -60]_{3s}$ specimen under tension

In the case of $[30, 60, 90, -60, -30]_{2s}$ unnotched and open-hole 'soft ply' specimens, the stiffness predictions are also quite accurate. The numerical predictions in Figures 6.5a and 6.5b closely follow the experimental data. The damage contour for the $[30, 60, 90, -60, -30]_{2s}$

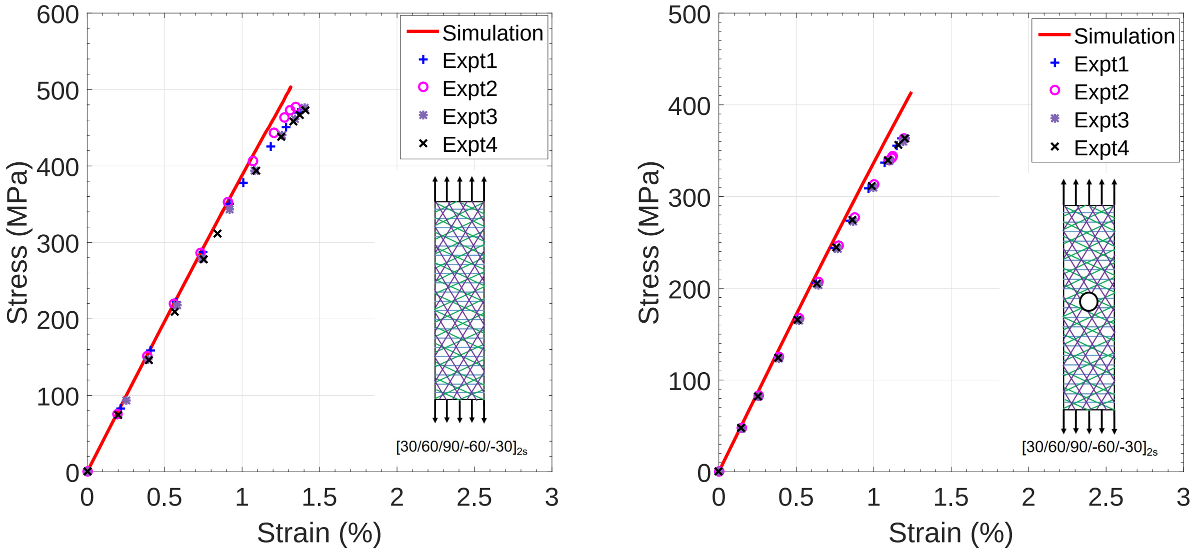

(a) Unnotched specimens

(b) Open hole specimens

Figure 6.5: Stress vs. strain for $[30, 60, 90, -60, -30]_{2s}$ specimens under tension

laminate specimen shows mostly matrix-cracking in the 60° plies, as shown in Figure 6.6. No significant fiber damage or delamination is observed.

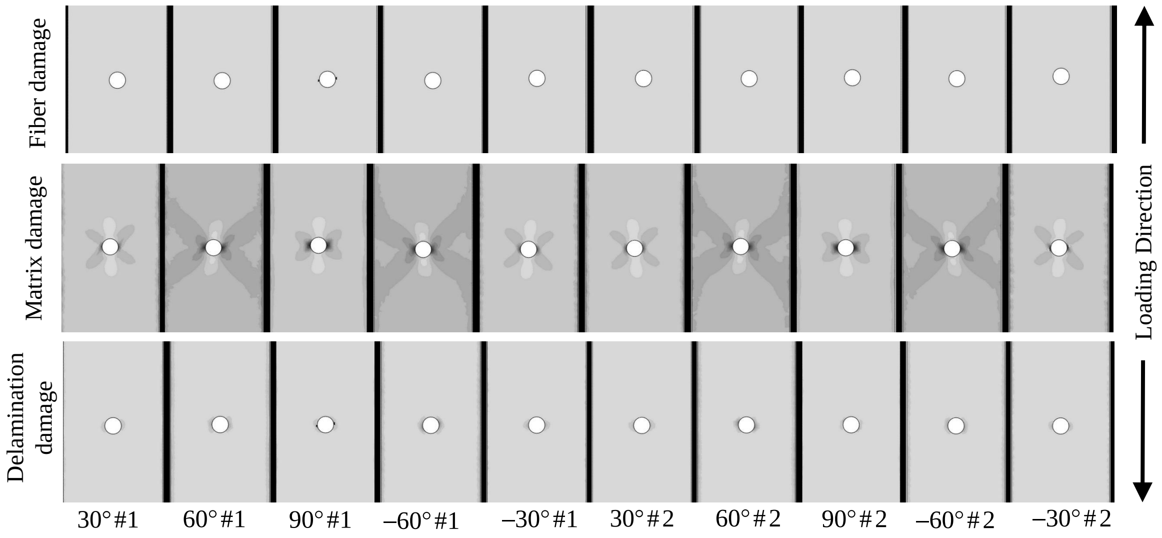

Figure 6.6: Damage contour for $[30, 60, 90, -60, -30]_{2s}$ specimen under tension

6.2 Numerical Specimens in Compression

In this case, all the laminates are subjected to uniaxial compressive loading in the longitudinal direction. It is observed that the initial stiffness predicted by the proposed model closely follows the experimental data. The results for $[0, 45, 90, -45]_{2s}$, $[60, 0, -60]_{3s}$ and $[30, 60, 90, -60, -30]_{2s}$ under uniaxial compression are presented in Figures 6.7, 6.9 and 6.11. It should be noted that in all the open-hole compression cases, the experimental data was found to be noisy, confirming the findings in Clay and Knoth [16].

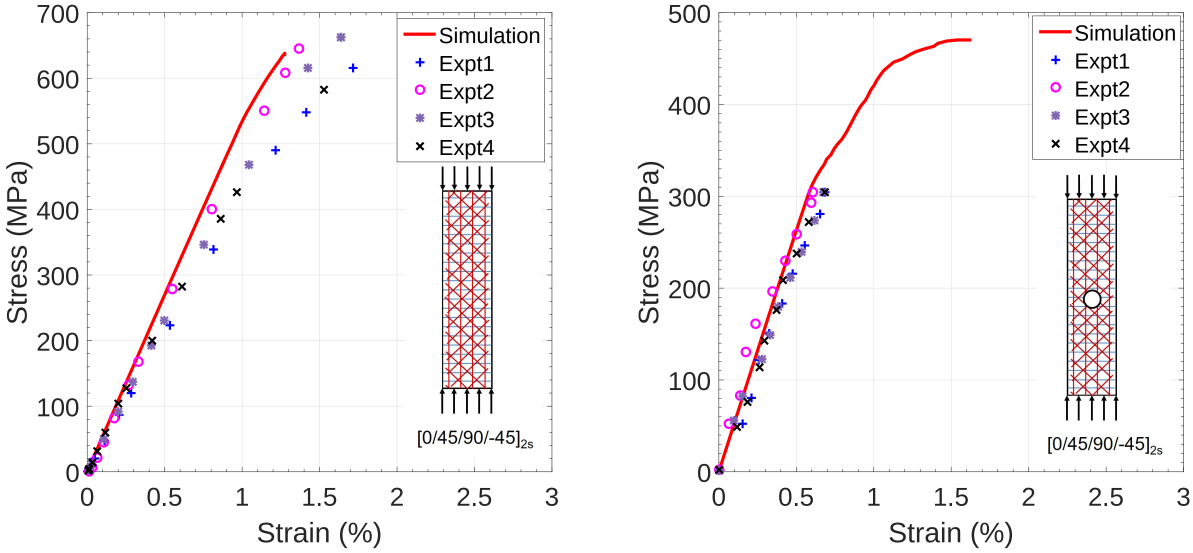

(a) Unnotched specimen (b) Open hole specimen

Figure 6.7: Stress vs. strain for $[0, 45, 90, -45]_{2s}$ quasi-isotropic specimens under compression

The unnotched compression prediction of $[0, 45, 90, -45]_{2s}$ follows the experimentally observed data. However, the experimental data is beset with significant variance, as shown in 6.7a. The prediction for $[0, 45, 90, -45]_{2s}$ open-hole numerical specimen demonstrates higher strength. It is reported by ARFL (see Ref. [24]) that some of the experimental specimen failed prematurely due to buckling. Such second-order phenomenon is not considered in this study.

In the $[0, 45, 90, -45]_{2s}$ quasi-isotropic open-hole specimen under compression the damage contour shows failure of plies in all three failure modes, as shown in Figure 6.8.

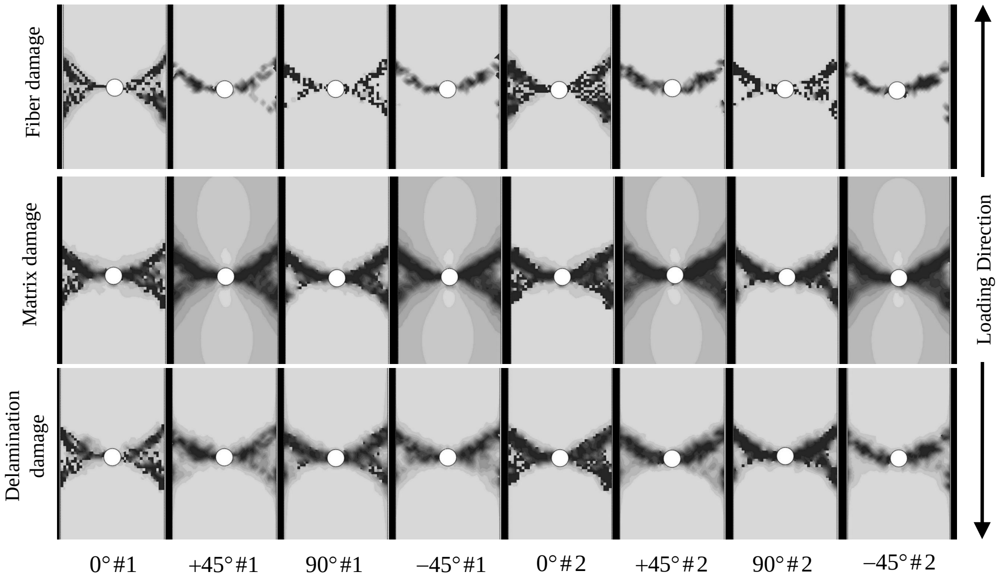

Figure 6.8: Damage contour for $[0, 45, 90, -45]_{2s}$ specimen under compression

In the case of $[60, 0, -60]_{3s}$ unnotched specimen the numerical model underpredicts the strength of the laminate.

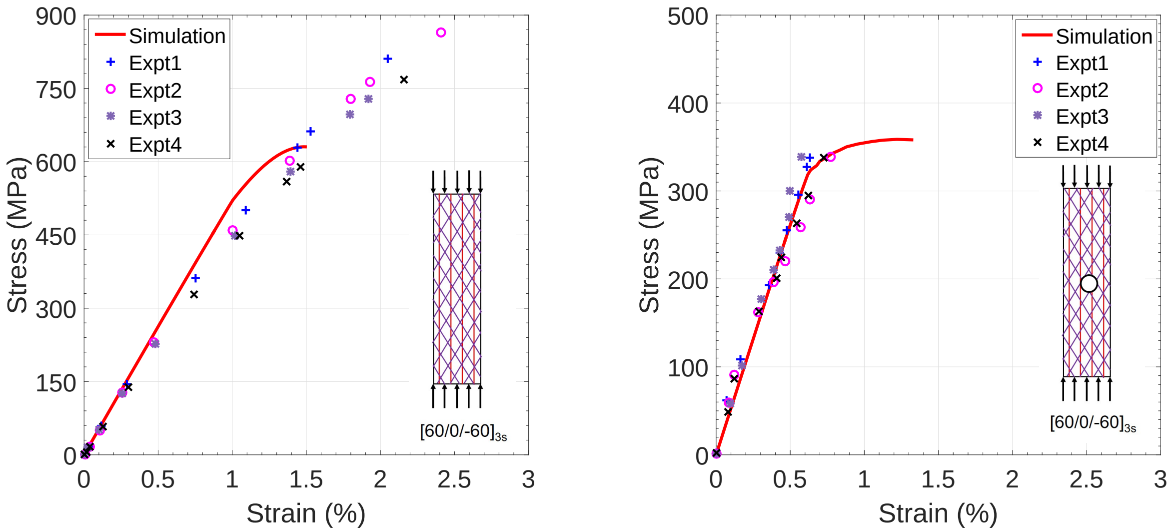

(a) Unnotched specimen

(b) Open hole specimen

Figure 6.9: Stress vs. strain for $[60, 0, -60]_{3s}$ specimens under compression

The possible reasons can partly be attributed to the reduced order modeling process and partly to significant uncertainty in the experimental data, as evident from Figure 6.9a. In the open-hole case, the numerical predictions shown in Figure 6.9b tend to exactly follow the experimental data. In the $[60, 0, -60]_{3s}$ open-hole layup fiber splitting is observed in the 60° plies. Matrix-cracking observed in 0° plies is higher than 60° plies as shown in Figure 6.10.

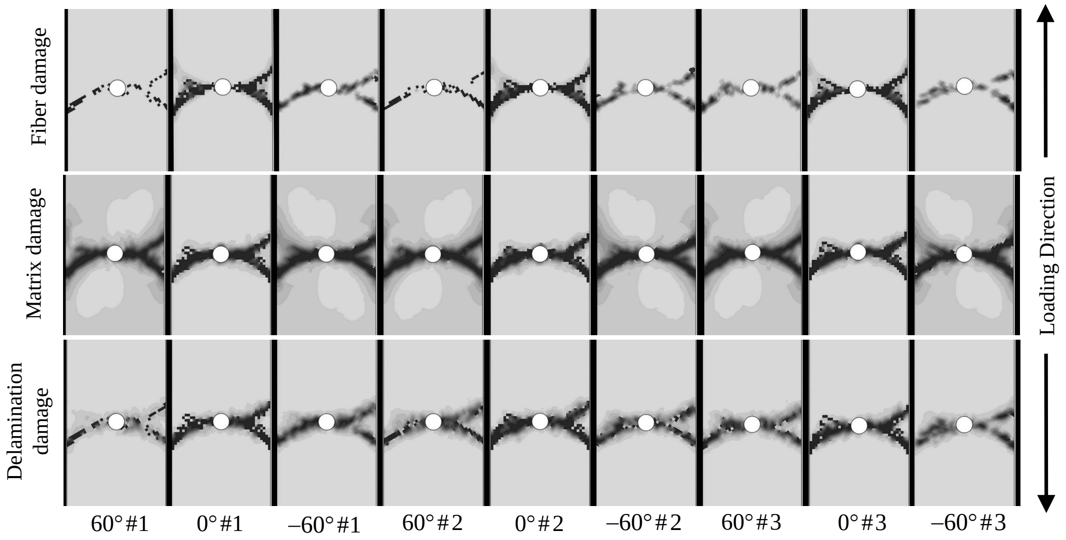

Figure 6.10: Damage contour for $[60, 0, -60]_{3s}$ specimen under compression

Compression stiffness of $[30, 60, 90, -60, -30]_{2s}$ unnotched specimen initially tended to follow the stiffness observed in the experiment. But the reported strength for the layups were suspiciously too high for a soft layup like $[30, 60, 90, -60, -30]_{2s}$. In the case of open-hole compression, the predictions agree well with experimental data except near the tail end, , where the experimental data was reported to be very noisy, and the coupon specimens were loaded till 90% of the ultimate load.

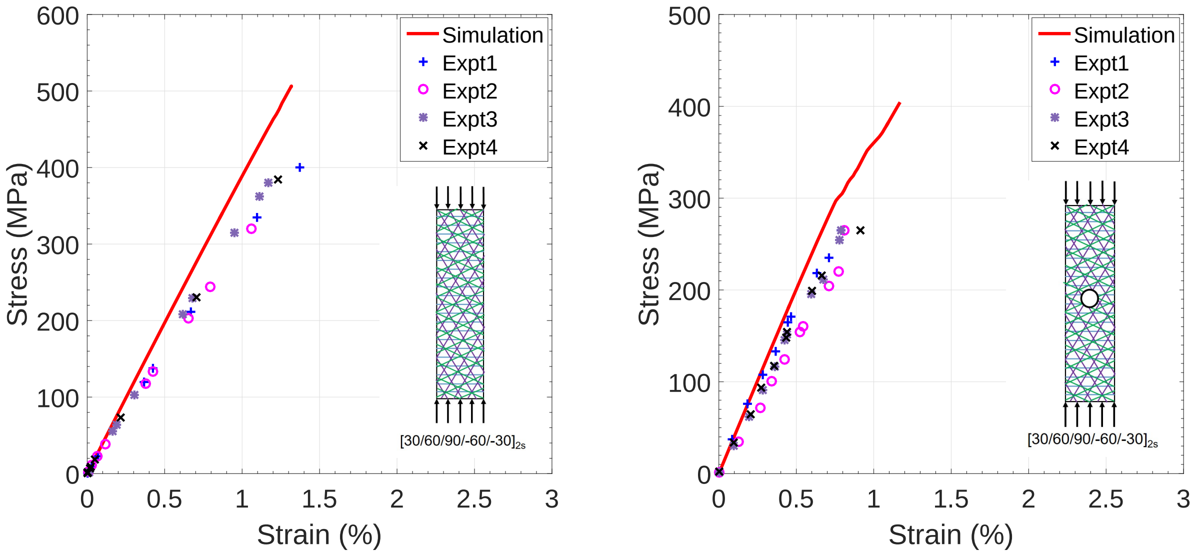

(a) Unnotched specimen

(b) Open hole specimen

Figure 6.11: Stress vs. strain for $[30, 60, 90, -60, -30]_{2s}$ specimens under compression

In the case of the $[30, 60, 90, -60, -30]_{2s}$ open-hole layup, damage accumulation due to matrix cracking was observed in the case of 30° and 60° angle plies, as evidenced in Figure 6.12. In addition, no fiber damage or delamination is observed. This could be another reason for high strength predictions observed in Figure 6.11b.

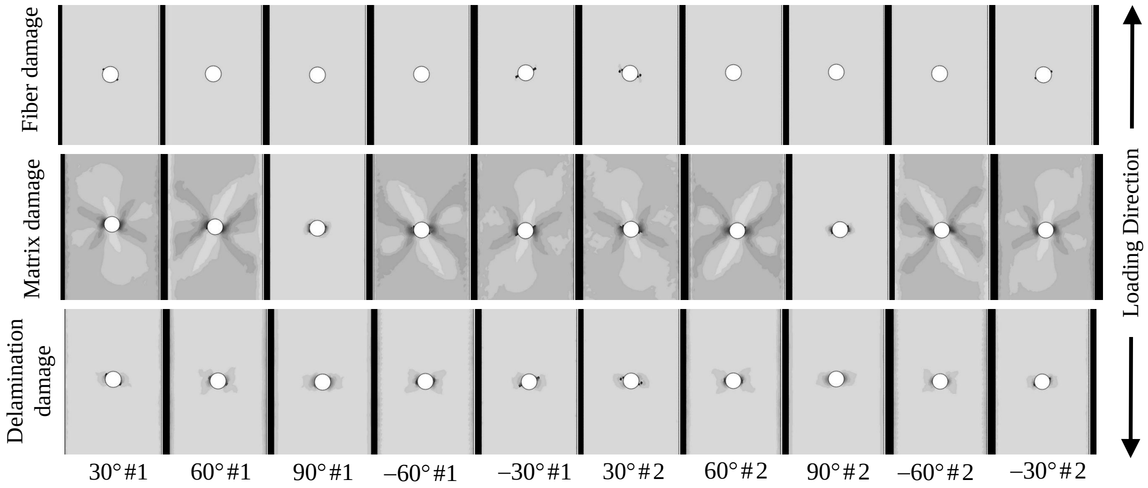

Figure 6.12: Damage contour for $[30, 60, 90, -60, -30]_{2s}$ specimen under compression

To this end, a summary of the predicted strengths is presented in Table 6.1 along with the simulation wall clock time on the cluster computer. The unnotched tension and compression is denoted as UNT and UNC respectively. Similarly, the open-hole specimens under tension and compression are denoted as OHT and OHC, respectively.

Table 6.1: Summary of simulation wall time and predicted strengths of IM7/977-3 laminates

Layup	**Type**	**Wall clock time (hh:mm)**	**AHLS model (MPa)**	**AFRL Mean (MPa)**	**AFRL St. Dev (%)**
$[0, 45, 90, -45]_{2s}$	UNT	00 : 48	980.67	866	1.48
	OHT	03 : 20	600.77	554	1.29
	UNC	00 : 47	638.08	603	1.41
	OHC	04 : 48	470.29	341	0.78
$[60, 0, -60]_{3s}$	UNT	01 : 25	1056.6	1005	1.64
	OHT	04 : 04	533.95	543	1.09
	UNC	01 : 58	630.42	765	2.03
	OHC	05 : 47	358.69	358	0.92
$[30, 60, 90, -60, -30]_{2s}$	UNT	01 : 13	503.30	473	1.38
	OHT	01 : 12	414.06	409	1.44
	UNC	01 : 12	506.45	392	1.26
	OHC	01 : 45	404.4	295	1.01

CHAPTER 7

CONCLUSIONS AND FUTURE RESEARCH

7.1 Conclusions

The research presented in this dissertation demonstrates significant addition to the state of the art in the computational modeling of the mechanical behavior for CFRP composite materials. This study incorporates multiscale constitutive modeling from both deterministic and probabilistic points of view. The primary goal of this dissertation was to develop a novel constitutive relationship under uncertainty alleviating spurious mesh sensitivity from the ERHM framework.

In Chapter 2, the ERHM multiscale modeling framework is described. Development of a new reduced order model partitioning using the Representative Unit Cell morphology is demonstrated. The treatment of alleviating the post failure spurious residual stiffness is presented followed by verification. Finally, enhancement of computational efficiency of the coefficient tensor computation using parallel computing is shown. The speed up and efficiency of the computation is quantified for the purpose of verification. Utilization of parallel computing reduced the computing time significantly.

Chapter 3 presents the mechanics-based formulation of the constitutive relation for the polymer matrix and carbon fiber reinforcement. The damage evolution potential for the softening regime is derived such that the material fails consistently following a linear stress-strain law. The proposed model is derived based on the thermodynamics of material damage. The damage evolution potential to model the material in the softening regime is derived and verified. A new triaxiality factor is derived to indicate the complex strain state. The constitutive relation is incorporated in the multiscale framework to model progressive damage in CFRP composite laminates. The novel contribution of this part of the research is the ability to capture the failure envelope of composites under multi-axial loading. The parameters for the constitutive model are calibrated using experimental data obtained at laminate scale. The calibration process considering epistemic uncertainty is presented in Chapter 4.

The development and implementation of the multiscale crack band model is given in Chapter 5. The objective of this work was to alleviate spurious mesh sensitivity using numerical regularization of dissipated energy. First, the performance of the proposed model is examined for unit cube composite specimen with various levels of discretization. Then, the model is verified for composite single ply and laminates. The model has shown its capability to alleviate mesh sensitivity. Finally, the mesh independent multiscale modeling framework is validated using three laminates with different configurations and loading. The validation study is presented in Chapter 6.

7.2 Future Research

In this dissertation the multiscale framework and constitutive relationship is employed assuming no effect of change in temperature. However, during service condition an aircraft experiences a wide range of temperature conditions. The mechanical properties of constituent materials of a composite can vary significantly with temperature. These effects can be taken into account within the constitutive relation. In addition, temperature field could also be incorporated within the multiple spatial scale framework for thermo-mechanical analysis of composites. An extension of the present multiscale framework to thin shell structure would allow more accurate representation of aircraft skin structures.

In PDA of bolted joints, contact between lamina brings additional complexity in the failure mechanisms. A thorough investigation can be done using contact mechanics. In this direction single or double lap joints with different types of fasteners (*e.g.* countersunk or protruded bolt) can be studied. Additionally, joints involving composites to metallic material is a challenging problem in aircraft structural design.

Modeling mechanical behavior of composite laminates under fatigue and impact are still maturing. To simulate more realistic service condition of an aircraft the above ideas should be applied to a multi-temporal framework. There are still open areas to develop computationally efficient multi-temporal model for high cycle fatigue. Although high performance computing infrastructure is used for macroscale analysis yet it is still expensive. A numerical approach could be developed to reduce the problem size of the reduced order model.

The studies in this dissertation are restricted to Representative Unit Cell with no defect. Although quality control techniques are utilized by manufactures, there are sources of variability within the material both at the micro and the structural scales. At the microscale, uncertainty is present due to variation in geometrical and constituent material properties. The effect of aleatory uncertainty arising from spatial variability needs to be incorporated both at microscale and macroscale.

REFERENCES

[1] ASTM Standard 3039. Standard test method for tensile properties of polymer matrix composite materials. ASTM International, West Conshohocken, PA, 2008.

[2] ASTM Standard 7078. Standard test method for shear properties of composite materials by v-notched rail shear method. ASTM International, West Conshohocken, PA, 2005.

[3] ASTM Standard D3410. Standard test method for compressive properties of polymer matrix composite materials with unsupported gage section by shear loading. ASTM International, West Conshohocken, PA, 2008.

[4] G. I. Barenblatt. The Mathematical Theory of Equilibrium Cracks in Brittle Fracture. In H.L. Dryden, Th. von Kármán, G. Kuerti, F.H. van den Dungen, and L. Howarth, editors, *The Mathematical Theory of Equilibrium Cracks in Brittle Fracture*, volume 7 of *Advances in Applied Mechanics*, pages 55 – 129. Elsevier, 1962. doi: https://doi.org/10.1016/S0065-2156(08)70121-2. URL http://www.sciencedirect.com/science/article/pii/S0065215608701212.

[5] Z. P. Bažant. Imbricate continuum and its variational derivation. *Journal of Engineering Mechanics*, 110(12):1693–1712, Dec 1984. doi: 10.1061/(ASCE)0733-9399(1984)110:12(1693). URL https://doi.org/10.1061/(ASCE)0733-9399(1984)110:12(1693).

[6] Z. P. Bažant and B. H. Oh. Crack band theory for fracture of concrete. *Materials and Structures*, 16(3):155–177, 1983.

[7] R. Bhattacharyya and P. K. Basu. Multiscale progressive damage analysis of CFRP composites using a mechanics based constitutive relation. *Composite Structures*, 235:111759, 2020. ISSN 0263-8223. doi: https://doi.org/10.1016/j.compstruct.2019.111759. URL http://www.sciencedirect.com/science/article/pii/S0263822319325310.

[8] R. Bhattacharyya and P. K. Basu. Multiscale crack band model for eigenstrain based reduced order homogenization. *Computational Mechanics*, 66(6):1237–1255, Aug 2020. ISSN 1432-0924. doi: 10.1007/s00466-020-01896-0. URL https://doi.org/10.1007/s00466-020-01896-0.

[9] M. J. Bogdanor and C. Oskay. Prediction of progressive damage and strength of IM7/977-3 composites using the Eigendeformation-based homogenization approach: static loading. *Journal of Composite Materials*, 51(10):1455–1472, 2017.

[10] J. Brynjarsdóttir and A. O'Hagan. Learning about physical parameters: the importance of model discrepancy. *Inverse Problems*, 30(11):114007, oct 2014. doi: 10.1088/0266-5611/30/11/114007. URL https://doi.org/10.1088%2F0266-5611%2F30%2F11%2F114007.

[11] G. T. Camacho and M. Ortiz. Computational modelling of impact damage in brittle materials. *International Journal of Solids and Structures*, 33(20):2899 – 2938, 1996. ISSN 0020-7683. doi: https://doi.org/10.1016/0020-7683(95)00255-3. URL http://www.sciencedirect.com/science/article/pii/0020768395002553.

[12] V. Cervenka. *Inelastic finite element analysis of reinforced concrete panels*. PhD thesis, University of Colorado, 1970.

[13] J. L. Chaboche. Continuum damage mechanics: Part I - General concepts. *Journal of Applied Mechanics*, 55(1):59–64, Mar 1988. ISSN 0021-8936. doi: 10.1115/1.3173661. URL http://dx.doi.org/10.1115/1.3173661.

[14] J. L. Chaboche. Continuum damage mechanics: Part II Damage growth, crack initiation, and crack growth. *Journal of Applied Mechanics*, 55(1):65–72, Mar 1988. ISSN 0021-8936. doi: 10.1115/1.3173662. URL http://dx.doi.org/10.1115/1.3173662.

[15] M. Christie, J. Glimm, J. W. Grove, D. Higdon, D. Sharp, and M. Wood-Schultz. Error analysis and simulations of complex phenomena. *Los Alamos Science*, 2005.

[16] S. B. Clay and P. M. Knoth. Experimental results of quasi-static testing for calibration and validation of composite progressive damage analysis methods. *Journal of Composite Materials*, 51(10):1333–1353, 2017.

[17] R. D. Crouch and C. Oskay. Symmetric mesomechanical model for failure analysis of heterogeneous materials. *International Journal for Multiscale Computational Engineering*, 8:447–461, 2010.

[18] R. D. Crouch, S. B. Clay, and C. Oskay. Experimental and computational investigation of progressive damage accumulation in CFRP composites. *Composites Part B: Engineering*, 48:59–67, 2013.

[19] L. Dagum and R. Menon. OpenMP: an industry standard API for shared-memory programming. *Computational Science & Engineering, IEEE*, 5(1):46–55, 1998.

[20] R. de Borst and H.-B. Mühlhaus. Gradient-dependent plasticity: Formulation and algorithmic aspects. *International Journal for Numerical Methods in Engineering*, 35(3): 521–539, 1992. doi: 10.1002/nme.1620350307. URL `https://onlinelibrary.wiley.com/doi/abs/10.1002/nme.1620350307`.

[21] R. de Borst, J. Pamin, and M. G. D. Geers. On coupled gradient-dependent plasticity and damage theories with a view to localization analysis. *European Journal of Mechanics - A/Solids*, 18(6):939 – 962, 1999. ISSN 0997-7538. doi: https://doi.org/10.1016/S0997-7538(99)00114-X. URL `http://www.sciencedirect.com/science/article/pii/S099775389900114X`.

[22] Department of Defense. *Composite Materials Handbook*, volume 2. Polymer Matrix Composites Materials Properties. SAE International, F edition, 2002.

[23] D. S. Dugdale. Yielding of steel sheets containing slits. *Journal of the Mechanics and Physics of Solids*, 8(2):100 – 104, 1960. ISSN 0022-5096. doi: https://doi.org/10.1016/0022-5096(60)90013-2. URL `http://www.sciencedirect.com/science/article/pii/0022509660900132`.

[24] S. P. Engelstad and S. B. Clay. Comparison of composite damage growth tools for static behavior of notched composite laminates. *Journal of Composite Materials*, 51 (10):1493–1524, 2017. doi: 10.1177/0021998316675945. URL `https://doi.org/10.1177/0021998316675945`.

[25] B. Fedulov, A. Fedorenko, A. Safonov, and E. Lomakin. Nonlinear shear behavior and failure of composite materials under plane stress conditions. *Acta Mechanica*, 228 (6):2033–2040, Jun 2017. ISSN 1619-6937. doi: 10.1007/s00707-017-1817-4. URL `https://doi.org/10.1007/s00707-017-1817-4`.

[26] F. Feyel and J. L. Chaboche. FE^2 multiscale approach for modelling the elastoviscoplastic behavior of long fiber SiC/Ti composite materials. *Computer Methods in Applied Mechanics and Engineering*, 183:309–330, 2000.

[27] J. Fish. *Practical multiscaling*. John Wiley & Sons, 2013.

[28] J. Fish, V. Filonova, and Z. Yuan. Hybrid impotent-incompatible eigenstrain base homogenization. *International Journal for Numerical Methods in Engineering*, 95(1): 1–32, 2013.

[29] R. Furuhashi and T. Mura. On the equivalent inclusion method and impotent eigenstrains. *Journal of Elasticity*, 9(3):263–270, 1979.

[30] M. G. D. Geers. *Experimental analysis and computational modelling of damage and fracture*. PhD thesis, Technische Universiteit Eindhoven, 1997.

[31] S. Ghosh, K. Lee, and S. Moorthy. Multiple scale analysis of heterogeneous elastic structures using homogenization theory and voronoi cell finite element method. *International Journal of Solids and Structures*, 32(1):27–62, 1995. ISSN 0020-7683. doi: https://doi.org/10.1016/0020-7683(94)00097-G. URL http://www.sciencedirect.com/science/article/pii/002076839400097G.

[32] A. Gilat, R. K. Goldberg, and G. D. Roberts. Strain rate sensitivity of epoxy resin in tensile and shear loading. *Journal of Aerospace Engineering*, 2007.

[33] S. Govindjee, G. J. Kay, and J. C. Simo. Anisotropic modelling and numerical simulation of brittle damage in concrete. *International Journal for Numerical Methods in Engineering*, 38(21):3611–3633, 1995. doi: 10.1002/nme.1620382105. URL https://onlinelibrary.wiley.com/doi/abs/10.1002/nme.1620382105.

[34] J. M. Guedes and N. Kikuchi. Preprocessing and postprocessing for materials based on the homogenization method with Adaptive Finite Element Methods. *Computer Methods in Applied Mechanics and Engineering*, 83:143–198, 1990.

[35] C. Heinrich and A. M. Waas. Investigation of progressive damage and fracture in laminated composites using the Smeared Crack Approach. *Computers, Materials & Continua*, 35(2):155–181, 2013.

[36] R. Higuchi, T. Okabe, and T. Nagashima. Numerical simulation of progressive damage and failure in composite laminates using XFEM/CZM coupled approach. *Composites Part A: Applied Science and Manufacturing*, 95:197 – 207, 2017. ISSN 1359-835X. doi: https://doi.org/10.1016/j.compositesa.2016.12.026. URL http://www.sciencedirect.com/science/article/pii/S1359835X16304547.

[37] A. Hillerborg, M. Modéer, and P.-E. Petersson. Analysis of crack formation and crack growth in concrete by means of fracture mechanics and finite elements. *Cement and Concrete Research*, 6(6):773 – 781, 1976. ISSN 0008-8846. doi: https://doi.org/10.1016/0008-8846(76)90007-7. URL http://www.sciencedirect.com/science/article/pii/0008884676900077.

[38] M. Jirásek. Nonlocal models for damage and fracture: Comparison of approaches. *International Journal of Solids and Structures*, 35(31):4133 – 4145, 1998. ISSN 0020-7683. doi: https://doi.org/10.1016/S0020-7683(97)00306-5. URL `http://www.sciencedirect.com/science/article/pii/S0020768397003065`.

[39] M. Jirásek and M. Bauer. Numerical aspects of the crack band approach. *Computers & Structures*, 110-111:60–78, 2012.

[40] M. Jirásek and S. Rolshoven. Localization properties of strain-softening gradient plasticity models Part I: Strain-gradient theories. *International Journal of Solids and Structures*, 46:2225–2238, 2009.

[41] M. Jirásek and S. Rolshoven. Localization properties of strain-softening gradient plasticity models Part II: Theories with gradients of internal variables. *International Journal of Solids and Structures*, 46:2239–2254, 2009.

[42] M. C. Kennedy and A. O'Hagan. Bayesian calibration of computer models. *Journal Royal Statistical Society. series B*, 63:425–464, 2001.

[43] D. Krajcinovic. Continuum Damage Mechanics. *Applied Mechanics Reviews*, 37:1–6, 1984.

[44] D. Krajcinovic. *Damage Mechanics*, volume 41 of *North Holland Series in Applied Mathematics and Mechanics*. Elsevier, Amsterdam, 1996.

[45] F. Larsson, K. Runesson, S. Saroukhani, and R. Vafadari. Computational homogenization based on a weak format of micro-periodicity for RVE-problems. *Computer Methods in Applied Mechanics and Engineering*, 200(1):11 – 26, 2011. ISSN 0045-7825. doi: https://doi.org/10.1016/j.cma.2010.06.023. URL `http://www.sciencedirect.com/science/article/pii/S0045782510001908`.

[46] F. Laurin, N. Carrère, and J.-F. Maire. A multiscale progressive failure approach for composite laminates based on thermodynamical viscoelastic and damage models. *Composites Part A: Applied Science and Manufacturing*, 38(1):198 – 209, 2007. ISSN 1359-835X. doi: https://doi.org/10.1016/j.compositesa.2006.01.018. URL `http://www.sciencedirect.com/science/article/pii/S1359835X0600025X`.

[47] J. Lemaitre. How to use damage mechanics. *Nuclear Engineering and Design*, 80: 233–245, 1984.

[48] J. Lemaitre and R. Desmorat. *Engineering damage mechanics*. Springer-Verlag Berlin Heidelberg, 2005. ISBN 978-3-540-21503-5. doi: 10.1007/b138882.

[49] J. Lemaitre and J. Dufailly. Damage measurements. *Engineering Fracture Mechanics*, 28(5-6):643–661, 1987.

[50] F. A. Leone, C. G. Dávila, and D. Girolamo. Progressive damage analysis as a design tool for composite bonded joints. *Composites Part B: Engineering*, 77:474 – 483, 2015. ISSN 1359-8368. doi: https://doi.org/10.1016/j.compositesb.2015.03.046. URL `http://www.sciencedirect.com/science/article/pii/S1359836815001651`.

[51] J. D. Littell, C. R. Ruggeri, R. K. Goldberg, G. D. Roberts, W. A. Arnold, and W. K. Binienda. Measurement of epoxy resin tension, compression, and shear stress–strain curves over a wide range of strain rates using small test specimens. *Journal of Aerospace Engineering*, pages 162–173, 2008.

[52] X. Liu, D. Furrer, J. Kosters, and J. Holmes. Vision 2040: A Roadmap for Integrated, Multiscale Modeling and Simulation of Materials and Systems. Technical Report NASA/CR-2018-219771, E-19477, GRC-E-DAA-TN52454, NASA, March 01 2018.

[53] E. V. Lomakin and B. N. Fedulov. Nonlinear anisotropic elasticity for laminate composites. *Meccanica*, 50(6):1527–1535, Jun 2015. ISSN 1572-9648. doi: 10.1007/s11012-015-0104-5. URL `https://doi.org/10.1007/s11012-015-0104-5`.

[54] P. Maimí, P. P. Camanho, J. A. Mayugo, and C. G. Dávila. A continuum damage model for composite laminates: Part I Constitutive model. *Mechanics of Materials*, 39(10): 897–908, 2007. ISSN 0167-6636. doi: https://doi.org/10.1016/j.mechmat.2007.03.005. URL `http://www.sciencedirect.com/science/article/pii/S0167663607000543`.

[55] P. Maimí, P. P. Camanho, J. A. Mayugo, and C. G. Dávila. A continuum damage model for composite laminates: Part II Computational implementation and validation. *Mechanics of Materials*, 39(10):909–919, 2007. ISSN 0167-6636. doi: https://doi.org/10.1016/j.mechmat.2007.03.006. URL `http://www.sciencedirect.com/science/article/pii/S0167663607000555`.

[56] E. Massarwa, J. Aboudi, and R. Haj-Ali. A multiscale progressive damage analysis for laminated composite structures using the parametric HFGMC micromechanics. *Composite Structures*, 188:159 – 172, 2018. ISSN 0263-8223. doi: https://doi.org/10.1016/j.compstruct.2017.11.089. URL `http://www.sciencedirect.com/science/article/pii/S026382231730702X`.

[57] NASA. Advanced composites partnership. Technical report, NASA, 2014.

[58] S. Nemat-Nasser and M. Hori. *Micromechanics: Overall properties of heterogeneous materials*. North Holland, 1998. ISBN 9780444500847.

[59] J. Oliver. A consistent characteristic length for smeared cracking models. *International Journal for Numerical Methods in Engineering*, 28:461–474, 1989.

[60] C. Oskay and J. Fish. Eigendeformation-based reduced order homogenization for failure analysis of heterogeneous materials. *Computer Methods in Applied Mechanics and Engineering*, 196:1216–1243, 2007.

[61] R. M. O'Higgins, M. A. McCarthy, and C. T. McCarthy. Comparison of open hole tension characteristics of high strength glass and carbon fibre-reinforced composite materials. *Composites Science and Technology*, 68(13):2770 – 2778, 2008. ISSN 0266-3538. doi: https://doi.org/10.1016/j.compscitech.2008.06.003. URL `http://www.sciencedirect.com/science/article/pii/S0266353808002303`. Directions in Damage and Durability of Composite Materials, with regular papers.

[62] I. K. Park, K. J. Park, and S. J. Kim. Rate-dependent damage model for polymeric composites under in-plane shear dynamic loading. *Computational Materials Science*, 96:506–519, 2015.

[63] K. Park, G. H. Paulino, and J. R. Roesler. A unified potential-based cohesive model of mixed-mode fracture. *Journal of the Mechanics and Physics of Solids*, 57(6):891 – 908, 2009. ISSN 0022-5096. doi: https://doi.org/10.1016/j.jmps.2008.10.003. URL `http://www.sciencedirect.com/science/article/pii/S0022509608001713`.

[64] R. H. J. Peerlings, R. de Borst, W. A. M. Brekelmans, and J. H. P. de Vree. Gradient enhanced damage for quasi-brittle materials. *International Journal for Numerical Methods in Engineering*, 39(19):3391–3403, 1996. doi: 10.1002/(SICI)1097-0207(19961015)39:19⟨3391::AID-NME7⟩3.0.CO;2-D. URL `https://onlinelibrary.wiley.com/doi/abs/10.1002/%28SICI%291097-0207%2819961015%2939%3A19%3C3391%3A%3AAID-NME7%3E3.0.CO%3B2-D`.

[65] S. Pietruszczak and Z. Mroz. Finite element analysis of deformation of strain softening materials. *International Journal for Numerical Methods in Engineering*, 17:327–334, 1981.

[66] G. Pijaudier-Cabot and Z. P. Bažant. Nonlocal damage theory. *Journal of Engineering Mechanics*, 113:1512–1533, 1987.

[67] E. J. Pineda, B. A. Bednarcyk, A. M. Waas, and S. M. Arnold. Progressive failure of a unidirectional fiber-reinforced composite using the method of cells: Discretization objective computational results. *International Journal of Solids and Structures*, 50(9): 1203 – 1216, 2013. ISSN 0020-7683. doi: https://doi.org/10.1016/j.ijsolstr.2012.12.003. URL `http://www.sciencedirect.com/science/article/pii/S0020768312005069`.

[68] E. J. Pineda, B. A. Bednarcyk, and S. M. Arnold. Validated progressive damage analysis of simple polymer matrix composite laminates exhibiting matrix microdamage: Comparing macromechanics and micromechanics. *Composites Science and Technology*, 133:184 – 191, 2016. ISSN 0266-3538. doi: https://doi.org/10.1016/j.compscitech.2016.07.018. URL `http://www.sciencedirect.com/science/article/pii/S0266353816307692`.

[69] S. T. Pinho, L. Iannucci, and P. Robinson. Physically-based failure models and criteria for laminated fibre-reinforced composites with emphasis on fibre kinking: Part I: Development. *Composites Part A: Applied Science and Manufacturing*, 37(1):63 – 73, 2006. ISSN 1359-835X. doi: https://doi.org/10.1016/j.compositesa.2005.04.016. URL `http://www.sciencedirect.com/science/article/pii/S1359835X05002198`.

[70] S. T. Pinho, L. Iannucci, and P. Robinson. Physically based failure models and criteria for laminated fibre-reinforced composites with emphasis on fibre kinking. Part II: FE implementation. *Composites Part A: Applied Science and Manufacturing*, 37(5):766 – 777, 2006. ISSN 1359-835X. doi: https://doi.org/10.1016/j.compositesa.2005.06.008. URL `http://www.sciencedirect.com/science/article/pii/S1359835X05002708`.

[71] J. Reinoso, G. Catalanotti, A. Blázquez, P. Areias, P. P. Camanho, and F. París. A consistent anisotropic damage model for laminated fiber-reinforced composites using the 3D-version of the Puck failure criterion. *International Journal of Solids and Structures*, 126-127:37 – 53, 2017. ISSN 0020-7683. doi: https://doi.org/10.1016/j.ijsolstr.2017.07.023. URL `http://www.sciencedirect.com/science/article/pii/S0020768317303396`.

[72] M. Ridha, C. H. Wang, B. Y. Chen, and T. E. Tay. Modelling complex progressive failure in notched composite laminates with varying sizes and stacking sequences. *Composites Part A: Applied Science and Manufacturing*, 58:16 – 23, 2014. ISSN 1359-835X. doi: https://doi.org/10.1016/j.compositesa.2013.11.012. URL `http://www.sciencedirect.com/science/article/pii/S1359835X13003217`.

[73] J. G. Rots. *Computational modeling of concrete fracture*. PhD thesis, Delft University of Technology, 1988.

[74] M. Salavatian and L. V. Smith. An investigation of matrix damage in composite laminates using continuum damage mechanics. *Composite Structures*, 131:565 – 573, 2015.

[75] S. Sankararaman, Y. Ling, and S. Mahadevan. Uncertainty quantification and model validation of fatigue crack growth prediction. *Engineering Fracture Mechanics*, 78(7):1487 – 1504, 2011. ISSN 0013-7944. doi: https://doi.org/10.1016/j.engfracmech.2011.02.017. URL http://www.sciencedirect.com/science/article/pii/S0013794411000865.

[76] J. C. Simo and J. W. Ju. Strain- and stress-based continuum damage models- II. Computational aspects. *International Journal of Solids and Structures*, 23(7):841–869, 1987.

[77] A. T. Slobbe. *Propagation and band width of smeared cracks*. PhD thesis, TU Delft, February 2015.

[78] A. T. Slobbe, M. A. N. Hendriks, and J. G. Rots. Systematic assessment of directional mesh bias with periodic boundary conditions: Applied to the crack band model. *Engineering Fracture Mechanics*, 109:186 – 208, 2013. ISSN 0013-7944. doi: https://doi.org/10.1016/j.engfracmech.2013.06.005. URL http://www.sciencedirect.com/science/article/pii/S0013794413002361.

[79] C. Soutis and D. Turkmen. Moisture and temperature effects of the compressive failure of cfrp unidirectional laminates. *Journal of Composite Materials*, 31(8):832–849, 1997. doi: 10.1177/002199839703100805. URL https://doi.org/10.1177/002199839703100805.

[80] P. A. Sparks and C. Oskay. The method of failure paths for reduced-order computational homogenization. *International Journal for Multiscale Computational Engineering*, 14: 515–534, 2016. doi: http://dx.doi.org/10.1615/IntJMultCompEng.2016018702.

[81] Z. C. Su, T. E. Tay, M. Ridha, and B. Y. Chen. Progressive damage modeling of open-hole composite laminates under compression. *Composite Structures*, 122:507 – 517, 2015. ISSN 0263-8223. doi: https://doi.org/10.1016/j.compstruct.2014.12.022. URL http://www.sciencedirect.com/science/article/pii/S0263822314006783.

[82] K. Terada, M. Hori, T. Kyoya, and N. Kikuchi. Simulation of the multi-scale convergence in computational homogenization approaches. *International Journal of Solids and*

Structures, 37(16):2285 – 2311, 2000. ISSN 0020-7683. doi: https://doi.org/10.1016/S0020-7683(98)00341-2. URL http://www.sciencedirect.com/science/article/pii/S0020768398003412.

[83] J. M. Tyrus, M. Gosz, and E. DeSantiago. A local finite element implementation for imposing periodic boundary conditions on composite micromechanical models. *International Journal of Solids and Structures*, 44(9):2972 – 2989, 2007. ISSN 0020-7683. doi: https://doi.org/10.1016/j.ijsolstr.2006.08.040. URL http://www.sciencedirect.com/science/article/pii/S0020768306003489.

[84] B. van Dongen, A. van Oostrum, and D. Zarouchas. A blended continuum damage and fracture mechanics method for progressive damage analysis of composite structures using XFEM. *Composite Structures*, 184:512 – 522, 2018. ISSN 0263-8223. doi: https://doi.org/10.1016/j.compstruct.2017.10.007. URL http://www.sciencedirect.com/science/article/pii/S0263822317318585.

[85] W. Van Paepegem, I. De Baere, and J. J. Degrieck. Modelling the nonlinear shear stress–strain response of glass fibre-reinforced composites. Part I: Experimental results. *Composites Science and Technology*, 66(10):1455 – 1464, 2006. ISSN 0266-3538. doi: https://doi.org/10.1016/j.compscitech.2005.04.014. URL http://www.sciencedirect.com/science/article/pii/S0266353805000965.

[86] W. Van Paepegem, I. De Baere, and J. J. Degrieck. Modelling the nonlinear shear stress–strain response of glass fibre-reinforced composites. Part II: Model development and finite element simulations. *Composites Science and Technology*, 66(10):1465 – 1478, 2006. ISSN 0266-3538. doi: https://doi.org/10.1016/j.compscitech.2005.04.018. URL http://www.sciencedirect.com/science/article/pii/S026635380500117X.

[87] J. Červenka, V. Červenka, and S. Laserna. On crack band model in finite element analysis of concrete fracture in engineering practice. *Engineering Fracture Mechanics*, 197:27 – 47, 2018. ISSN 0013-7944. doi: https://doi.org/10.1016/j.engfracmech.2018.04.010. URL http://www.sciencedirect.com/science/article/pii/S0013794418301620.

[88] G. Z. Voyiadjis and P. I. Kattan. *Damage mechanics*. CRC Press: Taylor & Francis Group, 2005. ISBN 9780824727574.

[89] X.-P. Xu and A. Needleman. Numerical simulations of fast crack growth in brittle solids. *Journal of the Mechanics and Physics of Solids*, 42(9):1397 – 1434, 1994. ISSN 0022-5096. doi: https://doi.org/10.1016/0022-5096(94)90003-5. URL http://www.sciencedirect.com/science/article/pii/0022509694900035.

[90] Z. Zhang, G. H. Paulino, and W. Celes. Extrinsic cohesive modelling of dynamic fracture and microbranching instability in brittle materials. *International Journal for Numerical Methods in Engineering*, 72(8):893–923, 2007. doi: 10.1002/nme.2030. URL `https://onlinelibrary.wiley.com/doi/abs/10.1002/nme.2030`.

[91] T. I. Zohdi and P. Wriggers. *An Introduction to Computational Micromechanics*. Springer-Verlag Berlin Heidelberg, 1 edition, 2005. ISBN 978-3-540-77482-2. doi: 10.1007/978-3-540-32360-0.

Appendix A

Derivation of the proposed triaxiality factor

The concept of triaxiality factor is to control the constitutive model parameters to capture the nonlinear shear behavior to brittle uniaxial behavior. The old definition of triaxiality factor was given by Equation (A.1).

$$k_b^{\text{old}} = \frac{\gamma_{\max}}{\left(\dfrac{\gamma_{\max}}{2} + \epsilon_{\max}\right)} \in [0, 1] \tag{A.1}$$

In this work, the range of triaxiality is varied from purely uniaxial to pure shear loading. However, the numerical range of triaxiality factor remains same. Keeping in mind the two strain-states of interest, the expressions of new triaxiality factor is deduced.

Pure uniaxial loading:

Assuming an isotropic material, under pure uniaxial tension loading, the principal strain vector is written as: $\begin{Bmatrix}\epsilon & -\nu\epsilon & -\nu\epsilon\end{Bmatrix}^\intercal$. The maximum shear strain $\gamma_{\max}$ and maximum absolute principal strain $\epsilon_{\max}$ are computed as Equations (A.2) and (A.3)

$$\frac{\gamma_{\max}}{2} = \frac{\epsilon - (-\nu\epsilon)}{2} = \frac{(1+\nu)\epsilon}{2} \tag{A.2}$$

$$\epsilon_{\max} = \epsilon \tag{A.3}$$

Substituting the expressions in Equation (A.1) the triaxiality factor is computed as:

$$k_b = \frac{(1+\nu)\epsilon}{\frac{(1+\nu)\epsilon}{2} + \epsilon} = \frac{2(1+\nu)}{(3+\nu)} \tag{A.4}$$

In order to make $k_b = 0$ under pure uniaxial loading the expression takes the form of Equation (A.5).

$$k_b = \left[\frac{\gamma_{\max}}{\left(\frac{\gamma_{\max}}{2} + \epsilon_{\max}\right)} - \frac{2(1+\nu)}{(3+\nu)}\right] \tag{A.5}$$

This treatment is verified to be true both for uniaxial tensile and compressive loading.

Pure shear loading:

Now the Equation (A.5) needs to be factorized by x in order to get $k_b = 1$ under pure shear loading. Under pure shear loading the maximum shear strain $\gamma_{\max}$ and maximum absolute principal strain $\epsilon_{\max}$ are computed as Equations (A.6) and (A.7)

$$\frac{\gamma_{\max}}{2} = \frac{\epsilon - (-\epsilon)}{2} = \epsilon \tag{A.6}$$

$$\epsilon_{\max} = \epsilon \tag{A.7}$$

Substituting the maximum strains in Equation (A.5) with a factor x gives the following expression:

$$\begin{aligned} 1 &= x\left[\frac{2\epsilon}{\epsilon + \epsilon} - -\frac{2(1+\nu)}{(3+\nu)}\right] \\ &= x\left[\frac{3 + \nu - 2 - 2\nu}{3 + \nu}\right] \end{aligned}$$

Hence, the factor x comes as:

$$x = \frac{3 + \nu}{1 - \nu}$$

The final expression for triaxiality factor takes the form of Equation (A.8).

$$k_b = \frac{(3+\nu)}{(1-\nu)}\left[\frac{\gamma_{\max}}{\left(\frac{\gamma_{\max}}{2} + \epsilon_{\max}\right)} - \frac{2(1+\nu)}{(3+\nu)}\right] \tag{A.8}$$

Appendix B

Evaluation of damage equivalent strain parameters for matrix

The damage equivalent strain at each increment of loading is evaluated using Equation (3.2). In order to obtain the damage equivalent strain parameters (3 for pure uniaxial and 3 for pure shear) the corresponding two strain state vectors have been used. At first the expressions corresponding to pure uniaxial strain state is obtained. The strain vector for pure uniaxial and pure shear loading are written as Equations (B.1) and (B.2), respectively.

$$\boldsymbol{\epsilon}^{\mathrm{N}}_{(\cdot)} = \begin{bmatrix} \epsilon^{\mathrm{N}}_{(\cdot)} & 0 & 0 \\ 0 & -\nu\epsilon^{\mathrm{N}}_{(\cdot)} & 0 \\ 0 & 0 & -\nu\epsilon^{\mathrm{N}}_{(\cdot)} \end{bmatrix} \tag{B.1}$$

$$\boldsymbol{\epsilon}^{\mathrm{S}}_{(\cdot)} = \begin{bmatrix} 0 & \epsilon^{\mathrm{S}}_{(\cdot)} & 0 \\ \epsilon^{\mathrm{S}}_{(\cdot)} & 0 & 0 \\ 0 & 0 & 0 \end{bmatrix} \tag{B.2}$$

The principal strain vectors for pure uniaxial and pure shear loading are obtained as Equations (B.3) and (B.4) respectively.

$$\hat{\boldsymbol{\epsilon}}^{\mathrm{N}} = \left\{ \epsilon^{\mathrm{N}}_{(\cdot)} \quad -\nu\epsilon^{\mathrm{N}}_{(\cdot)} \quad -\nu\epsilon^{\mathrm{N}}_{(\cdot)} \right\}^{\mathsf{T}} \tag{B.3}$$

$$\hat{\boldsymbol{\epsilon}}^{\mathrm{S}} = \left\{ -\epsilon^{\mathrm{S}}_{(\cdot)} \quad 0 \quad \epsilon^{\mathrm{S}}_{(\cdot)} \right\}^{\mathsf{T}} \tag{B.4}$$

Pure uniaxial loading:

Substituting the strain tensor in Equation (3.2) with the expression for principal strain vector in Equation (B.3), the expression of damage equivalent strain parameter can be written as Equation (B.5)

$$\upsilon^{\mathrm{N}}_{(\cdot)} = \sqrt{\frac{1}{2}\begin{bmatrix} h_1\epsilon^{\mathrm{N}}_{(\cdot)} & -\nu h_2\epsilon^{\mathrm{N}}_{(\cdot)} & -\nu h_3\epsilon^{\mathrm{N}}_{(\cdot)} \end{bmatrix} \begin{bmatrix} \lambda+2\mu & \lambda & \lambda \\ \lambda & \lambda+2\mu & \lambda \\ \lambda & \lambda & \lambda+2\mu \end{bmatrix} \begin{bmatrix} h_1\epsilon^{\mathrm{N}}_{(\cdot)} \\ -\nu h_2\epsilon^{\mathrm{N}}_{(\cdot)} \\ -\nu h_3\epsilon^{\mathrm{N}}_{(\cdot)} \end{bmatrix}} \tag{B.5}$$

The final expression of $\upsilon^{\mathrm{N}}_{(\cdot)}$ after algebraic operation is Equation (B.6).

$$\upsilon^{N}_{(\cdot)} = \epsilon^{\mathrm{N}}_{(\cdot)}\sqrt{\frac{E}{2(1+\nu)(1-2\nu)}}\sqrt{(1-\nu)(h_1^2+\nu^2h_2^2+\nu^2h_3^2)-2\nu^2(h_1h_2+h_1h_3-\nu h_2h_3)} \tag{B.6}$$

Following the logic of Equation (3.4), $h_1 = 1$ and $h_2 = h_3 = c$. Hence, the Equation (B.6) finally takes the form of Equation (3.12).

Pure shear loading:

The development of damage equivalent strain parameters for shear loading follows the same methodology. In this case the damage equivalent strain parameter is expressed as Equation (B.7).

$$\upsilon^{\mathrm{S}}_{(\cdot)} = \sqrt{\frac{1}{2}\begin{bmatrix} -h_1\epsilon^{\mathrm{S}}_{(\cdot)} & 0 & h_3\epsilon^{\mathrm{S}}_{(\cdot)} \end{bmatrix} \begin{bmatrix} \lambda+2\mu & \lambda & \lambda \\ \lambda & \lambda+2\mu & \lambda \\ \lambda & \lambda & \lambda+2\mu \end{bmatrix} \begin{bmatrix} -h_1\epsilon^{\mathrm{S}}_{(\cdot)} \\ 0 \\ h_3\epsilon^{\mathrm{S}}_{(\cdot)} \end{bmatrix}} \tag{B.7}$$

The final expression of $\upsilon^{\mathrm{S}}_{(\cdot)}$ after algebraic operation is Equation (B.8).

$$\upsilon^{\mathrm{S}}_{(\cdot)} = \epsilon^{\mathrm{S}}_{(\cdot)}\sqrt{\frac{E}{2(1+\nu)(1-2\nu)}}\sqrt{(1-\nu)(h_1^2+h_3^2)-2\nu h_1h_3} \tag{B.8}$$

Following the logic of Equation (3.4), $h_1 = c$ and $h_3 = 1$. Hence, the Equation (B.8) finally takes the form of Equation (3.13). The damage equivalent strain parameters at damage threshold or initiation and failure are computed using experimental data.

Evaluation of transition damage equivalent strain for pure normal and pure shear loading can be computed using the analytical expressions. The transition damage equivalent strain is physically conceived as a strain at which (or at vicinity of which) the stress-strain diagram reaches a peak before softening. Mathematically, this point can be obtained by making the gradient of stress state equals to zero (Equation (B.9)).

$$\frac{d\boldsymbol{\sigma}}{d\epsilon} = (1-\omega)\mathbf{C} : \frac{d\boldsymbol{\epsilon}}{d\epsilon} - \frac{d\omega}{d\epsilon}\mathbf{C} : \boldsymbol{\epsilon} = 0 \tag{B.9}$$

Evaluation of $\upsilon_{\text{tr}}^{\text{N}}$ for pure normal loading is straightforward as there is a well-defined peak in the stress vs. strain plot. This parameter ($\upsilon_{\text{tr}}^{\text{N}}$) is obtained by solving Equation (B.10):

$$\psi^{\text{N}(m)} = E\left[(1-\omega(\upsilon_{\text{tr}}^{\text{N}})) - \frac{\alpha^{\text{N}}\upsilon_{\text{tr}}^{\text{N}}}{\left[\frac{\pi}{2}+\text{atan}(\beta^{\text{N}})\right]\left[1+\left(\alpha^{\text{N}}\langle\upsilon_{\text{tr}}^{\text{N}}-\upsilon_0\rangle-\beta^{\text{N}}\right)^2\right]}\right] = 0 \tag{B.10}$$

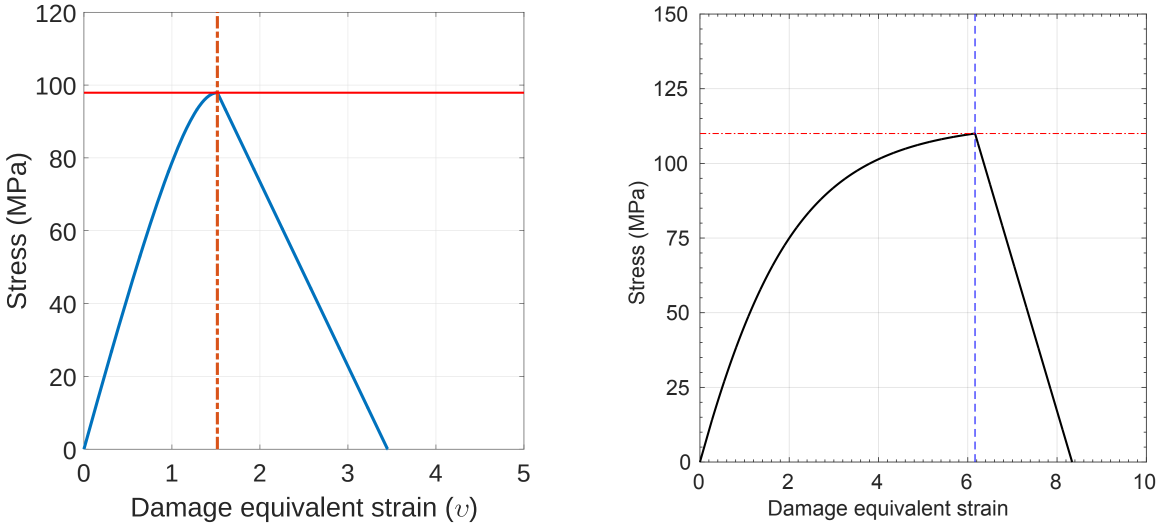

(a) Pure uniaxial load

(b) Pure shear load

Figure B.1: Evaluation of transition damage equivalent strain parameters

However, the above methodology can not be directly followed for pure shear loading as there is no such peak in the hardening regime due to presence of high ductility. The transition parameter, $\upsilon_{\text{tr}}^{\text{S}}$ for this case is obtained from maximum shear stress (τ_{max}), which is a parameter of this model. The Equation (B.11) is iteratively solved to obtain the transition parameter:

$$\psi^{\text{S}(m)} = \frac{\text{atan}(\alpha^{\text{S}}\langle\upsilon_{\text{tr}}^{\text{S}}-\upsilon_0\rangle-\beta^{\text{S}})+\text{atan}(\beta^{\text{S}})}{\frac{\pi}{2}+\text{atan}(\beta^{\text{S}})} + \frac{\tau_{\text{max}}(1+\nu)\chi_{\text{S}}}{E\upsilon_{\text{tr}}^{\text{S}}} - 1 = 0 \tag{B.11}$$

Evaluation of the transition damage equivalent strain parameters using Equations (B.10) and (B.11) are presented in Figures B.1a and B.1b respectively.

Appendix C

Evaluation of damage equivalent strain parameters for fiber

The model parameters that describe damage evolution and transitioning from the damage induced strain hardening regime to softening is obtained based on the analysis of the evolution equations under normal loading along the direction of the fiber length (assumed as the 3-direction in what follows). The strain tensor at initiation, transition or at final failure under uniaxial loading is written as:

$$\boldsymbol{\epsilon}_{(\cdot)} = \begin{bmatrix} -\nu_{31}\epsilon_{(\cdot)} & 0 & 0 \\ 0 & -\nu_{31}\epsilon_{(\cdot)} & 0 \\ 0 & 0 & \epsilon_{(\cdot)} \end{bmatrix} \tag{C.1}$$

The principal strains for the pure uniaxial loading are therefore:

$$\hat{\boldsymbol{\epsilon}} = \left\{ -\nu_{31}\epsilon_{(\cdot)} \quad -\nu_{31}\epsilon_{(\cdot)} \quad \epsilon_{(\cdot)} \right\}^{\mathsf{T}} \tag{C.2}$$

Substituting Equations (3.2) to (3.4) into the expression for principal strain vector in Equation (C.2), the expression of damage equivalent strain parameter can be written as:

$$\upsilon_{(\cdot)} = \sqrt{\frac{1}{2}\begin{bmatrix} -\nu_{31}c\epsilon_{(\cdot)} & -\nu_{31}c\epsilon_{(\cdot)} & \epsilon_{(\cdot)} \end{bmatrix} \begin{bmatrix} C_{11} & C_{12} & C_{13} \\ C_{12} & C_{11} & C_{13} \\ C_{13} & C_{13} & C_{33} \end{bmatrix} \begin{bmatrix} -\nu_{31}c\epsilon_{(\cdot)} \\ -\nu_{31}c\epsilon_{(\cdot)} \\ \epsilon_{(\cdot)} \end{bmatrix}} \tag{C.3}$$

Equation (C.3) can further be reduced by matrix operations:

$$\begin{aligned} \upsilon_{(\cdot)} &= \epsilon_{(\cdot)}\sqrt{\frac{1}{2}\begin{bmatrix} -\nu_{31}c & -\nu_{31}c & 1 \end{bmatrix} \begin{bmatrix} -\nu_{31}cC_{11} - \nu_{31}cC_{12} + C_{13} \\ -\nu_{31}cC_{12} - \nu_{31}cC_{11} + C_{13} \\ -\nu_{31}cC_{13} - \nu_{31}cC_{12} + C_{33} \end{bmatrix}} \\ &= \epsilon_{(\cdot)}\sqrt{\frac{1}{2}}\sqrt{2\nu_{31}^2c^2C_{11} + 2\nu_{31}^2c^2C_{12} - 4\nu_{31}cC_{13} + C_{33}} \end{aligned} \tag{C.4}$$

After rearranging, the final expression of $\upsilon_{(\cdot)}$ after algebraic operation is given in the following form as Equation (3.18):

$$\upsilon_{(\cdot)} = \epsilon_{(\cdot)}\sqrt{\frac{C_{33} + 2c^2\nu_{31}^2(C_{11} + C_{12}) - 4c\nu_{31}C_{13}}{2}} = \epsilon_{(\cdot)}\chi_{\mathrm{N}}^{(f)}$$

The final expression for Equation (B.9) to solve for υ_{tr} becomes Equation (C.5):

$$\psi^{(f)} = \big[C_{33} - 2\nu_{31}C_{13}\big]\left[(1 - \omega(\upsilon_{\mathrm{tr}})) - \frac{\alpha\upsilon_{\mathrm{tr}}}{\left[\frac{\pi}{2} + \operatorname{atan}(\beta)\right]\left[1 + \big(\alpha\langle\upsilon_{\mathrm{tr}} - \upsilon_0\rangle - \beta\big)^2\right]}\right] = 0 \quad \text{(C.5)}$$

Appendix D

Derivation of linear damage evolution function

The assumption of deriving a linear softening damage evolution function is to have a constant slope, A_f for the stress gradient. As a result, for a specific component of interest Equation (3.24) is written as Equation (D.1).

$$(1-\omega) - \frac{d\omega}{d\epsilon}\epsilon = -A_\mathrm{f} \tag{D.1}$$

Rearranging we get,

$$\frac{d\omega}{d\epsilon}\epsilon + \omega = (1 + A_\mathrm{f}) \tag{D.2}$$

This is a nonhomogeneous differential equation of order one. The integrating factor for Equation (D.2) is

$$\exp \int \frac{d\epsilon}{\epsilon} = \epsilon \tag{D.3}$$

Multiplying both sides of Equation (D.2) with the integrating factor

$$\omega\epsilon = \int (1 + A_\mathrm{f}) d\epsilon \tag{D.4}$$

which leads to

$$\omega = (1 + A_\mathrm{f}) + \frac{Q}{\epsilon} \tag{D.5}$$

where, Q is an integration constant. We evaluate the integration constant Q by satisfying the constraint: $\Phi(\upsilon_\mathrm{tr}^-) = \Phi(\upsilon_\mathrm{tr}^+)$. Finally,

$$Q = \epsilon_\mathrm{tr}\Big[\Phi(\upsilon_\mathrm{tr}) - (1 + A_\mathrm{f})\Big] \tag{D.6}$$

Multiplying the numerator and denominator with χ we obtain Equation (3.25) as below.

$$\omega = \frac{\upsilon_\mathrm{tr}}{\upsilon}\Big[\Phi(\upsilon_\mathrm{tr}) - \big(1 + A_\mathrm{f}\big)\Big] + \big(1 + A_\mathrm{f}\big)$$

Appendix E

Derivation of multiscale crack band model

In order to simplify the computation of the fracture strain, the part of the fracture energy within the softening regime is approximated in a linear fashion:

$$\tilde{G}_{\mathrm{f}}^{\mathrm{N}(2)}(\epsilon_{\mathrm{f}}^{\mathrm{N}}) = \frac{1}{2}\big(\epsilon_{\mathrm{f}}^{\mathrm{N}} - \epsilon_{\mathrm{tr}}^{\mathrm{N}}\big)\Big[1 - \Phi(\upsilon_{\mathrm{tr}}^{\mathrm{N}})\Big]E\epsilon_{\mathrm{tr}}^{\mathrm{N}} \tag{E.1}$$

$$\tilde{G}_{\mathrm{f}}^{\mathrm{S}(2)}(\epsilon_{\mathrm{f}}^{\mathrm{S}}) = \frac{1}{2}\big(\epsilon_{\mathrm{f}}^{\mathrm{S}} - \epsilon_{\mathrm{tr}}^{\mathrm{S}}\big)\Big[1 - \Phi(\upsilon_{\mathrm{tr}}^{\mathrm{S}})\Big]\frac{E}{(1+\nu)}\epsilon_{\mathrm{tr}}^{\mathrm{S}} \tag{E.2}$$

Let us consider the fracture energy for a reference mesh size h_0 for any loading case L is given as:

$$G_{\mathrm{f}}^{\mathrm{L}}\Big|_{h_0} = \frac{wh_0}{l}\Big[\tilde{G}_{\mathrm{f}}^{\mathrm{L}(1)} + \tilde{G}_{\mathrm{f}}^{\mathrm{L}(2)}(\epsilon_{\mathrm{f}}^{\mathrm{L}}\Big|_{h_0})\Big] \tag{E.3}$$

Similarly, the fracture energy for any arbitrary mesh size h can be written as:

$$G_{\mathrm{f}}^{\mathrm{L}} = \frac{wh}{l}\Big[\tilde{G}_{\mathrm{f}}^{\mathrm{L}(1)} + \tilde{G}_{\mathrm{f}}^{\mathrm{L}(2)}\Big] \tag{E.4}$$

The area in softening regime for any arbitrary mesh size h is scaled with a parameter $\tilde{c}$, as the fracture energy remains conserved. Hence, for any mesh size h, the fracture energy due to softening can be written as Equation (E.5).

$$\tilde{G}_{\mathrm{f}}^{\mathrm{L}(2)} = \frac{1}{\tilde{c}}\Big[\frac{l}{wh}G_{\mathrm{f}}^{\mathrm{L}} - \tilde{G}_{\mathrm{f}}^{L(1)}\Big] \tag{E.5}$$

Following the fact that, energy in the hardening regime remains same, we substitute $\tilde{G}_f^{L(1)}$ from Equation (E.3) to Equation (E.5) yields:

$$\tilde{G}_{\mathrm{f}}^{\mathrm{L}(2)} = \frac{1}{\tilde{c}}\Big[\frac{l}{wh}G_{\mathrm{f}}^{\mathrm{L}} - \frac{l}{wh_0}G_{\mathrm{f}}^{\mathrm{L}} + \tilde{c}\tilde{G}_{\mathrm{f}}^{\mathrm{L}(2)}\Big] \tag{E.6}$$

Now, substituting $G_{\mathrm{f}}^{\mathrm{L}}$ from Equation (E.3) into Equation (E.6), the fracture energy under softening for any mesh size h will be Equation (E.7).

$$\tilde{G}_{\mathrm{f}}^{\mathrm{L}(2)} = \frac{1}{\tilde{c}}\frac{h_0}{h}(\tilde{G}_{\mathrm{f}}^{\mathrm{L}(1)} + \tilde{G}_{\mathrm{f}}^{\mathrm{L}(2)}) - \frac{1}{\tilde{c}}\,(\tilde{G}_{\mathrm{f}}^{\mathrm{L}(1)} + \tilde{G}_{\mathrm{f}}^{\mathrm{L}(2)}) + \tilde{G}_{\mathrm{f}}^{\mathrm{L}(2)} \tag{E.7}$$

Rearranging fracture energy terms in Equation (E.7) under hardening and softening, we obtain Equation (E.8).

$$\tilde{G}_{\mathrm{f}}^{\mathrm{L}(2)} = \frac{1}{\tilde{c}}\left(\frac{h_0}{h} - 1\right)\tilde{G}_{\mathrm{f}}^{\mathrm{L}(1)} + \left[1 + \frac{1}{\tilde{c}}\left(\frac{h_0}{h} - 1\right)\right]\tilde{G}_{\mathrm{f}}^{\mathrm{L}(2)}(\epsilon_{\mathrm{f}}^{\mathrm{L}}\Big|_{h_0}) \tag{E.8}$$

Now, for uniaxial and pure shear loading, the failure strains can be expressed in terms of $\tilde{G}_f^{N(2)}$ and $\tilde{G}_f^{S(2)}$ using Equations (E.1) and (E.2) as:

$$\epsilon_{\mathrm{f}}^{\mathrm{N}} = 2\frac{\tilde{G}_{\mathrm{f}}^{\mathrm{N}(2)}}{\big[1 - \Phi(\upsilon_{\mathrm{tr}}^{\mathrm{N}})\big]E\epsilon_{\mathrm{tr}}^{\mathrm{N}}} + \epsilon_{\mathrm{tr}}^{\mathrm{N}} \tag{E.9}$$

$$\epsilon_{\mathrm{f}}^{\mathrm{S}} = 2(1+\nu)\frac{\tilde{G}_{\mathrm{f}}^{\mathrm{S}(2)}}{\big[1 - \Phi(\upsilon_{\mathrm{tr}}^{\mathrm{S}})\big]E\epsilon_{\mathrm{tr}}^{\mathrm{S}}} + \epsilon_{\mathrm{tr}}^{\mathrm{S}} \tag{E.10}$$

Appendix F

MATLAB script for characteristic length computation

```
function CElEnt=Compute_Chlen(int_pt,crack_vec,coord,center_coord,n_node)

% Gauss points coordinates on each direction
if int_pt == 1
    GaussPoint = 0 ;                              % Reduced integration
else
    GaussPoint = [-1/sqrt(3), 1/sqrt(3)];    % Full integration
end

% Compute the projection on to crack direction
proj=zeros(n_node,1);
for i=1:n_node
    proj(i,1)=(coord(i,:)-center_coord)*crack_vec;
end

tau_max = max(proj);
tau_min = min(proj);

% Evaluate the indicator function at each node
tau_i=zeros(n_node,1);
for i=1:n_node
    tau_i(i,1)=(proj(i,1)-tau_min)/(tau_max-tau_min);
end

% Preallocate memory for characteristic length
CElEnt = 0.;

% Loop over each Gauss point
for xi=GaussPoint
    for eta=GaussPoint
        for zeta=GaussPoint
            % Compute shape functions derivatives w.r.t canonical
            % coordinates
            dShape_dCanconical = (1/8)*...
                [-(1-eta)*(1-zeta),(1-eta)*(1-zeta) ,...
                (1+eta)*(1-zeta),-(1+eta)*(1-zeta),-(1-eta)*(1+zeta) ,...
                (1-eta)*(1+zeta),(1+eta)*(1+zeta),-(1+eta)*(1+zeta);...

                -(1-xi)*(1-zeta),-(1+xi)*(1-zeta),(1+xi)*(1-zeta) ,...
```

```
                (1-xi)*(1-zeta),-(1-xi)*(1+zeta),-(1+xi)*(1+zeta) ,...
                (1+xi)*(1+zeta),(1-xi)*(1+zeta);...

                -(1-xi)*(1-eta),-(1+xi)*(1-eta),-(1+xi)*(1+eta) ,...
                -(1-xi)*(1+eta),(1-xi)*(1-eta),(1+xi)*(1-eta) ,...
                (1+xi)*(1+eta), (1-xi)*(1+eta)];

            % Compute Jacobian matrix
            JacobianMatrix = dShape_dCanconical*coord;

            % Compute shape functions derivatives w.r.t global
            % coordinates
            dShape_dGlobal = JacobianMatrix\dShape_dCanconical;

            CElEnt = inv((dShape_dGlobal*tau_i)'*crack_vec);
        end
    end
end

end
```